Studies on Some Aspects of Neutron Stars – From Crust to Core

By

Rana Nandi

(PHYS05200704006)

Saha Institute of Nuclear Physics
Kolkata

A thesis submitted to the
Board of Studies in Physical Sciences
In partial fulfillment of requirements
For the Degree of

DOCTOR OF PHILOSOPHY

of

HOMI BHABHA NATIONAL INSTITUTE

July, 2012

Homi Bhabha National Institute

Recommendations of the Viva Voce board

As members of the Viva Voce Board, we certify that we have read the dissertation prepared by Rana Nandi entitled "Studies on Some Aspects of Neutron Stars – From Crust to Core" and recommend that it may be accepted as fulfilling the dissertation requirement for the Degree of Doctor of Philosophy.

Date:

Chairman -

Date:

Convener -

Date:

Member 1 -

Date:

Member 2 -

Date:

Member 3 -

Date:

Member 4 -

Final approval and acceptance of this dissertation is contingent upon the candidates submission of the final copies of the dissertation to HBNI.

I hereby certify that I have read this dissertation prepared under my direction and recommend that it may be accepted as fulfilling the dissertation requirement.

Date:

Guide

STATEMENT BY AUTHOR

Rana Nandi

DECLARATION

I, hereby declare that the investigation presented in the thesis has been carried out by me. The work is original and has not been submitted earlier as a whole or in part for a degree / diploma at this or any other Institution / University.

Rana Nandi

To My Parents......

ACKNOWLEDGEMENT

At first I express my sincere gratitude and indebtedness to my thesis supervisor Prof. Debades Bandyopadhyay for providing his sincere help and guidance during the entire period of my research. He has always motivated me and incessantly encouraged me to pursue my own line of thinking. I am grateful to him for his patience and boosting my confidence from time to time.

Immediate next name that comes to my mind is Dr. Sarmistha Banik who helped me all through my research days at SINP. I am grateful to her for collaborating with me in various projects which constituted my thesis in turn and also for helping me to acquire programming skills. I also like to thank my other collaborators Dr. Debarati Chatterjee, Prof. Igor N. Mishustin and Prof. Walter Greiner for their invaluable advice and guidance.

I wish to express my warm and sincere thanks to Prof. Jadunath De, Prof. Santosh Samaddar and Prof. Bijoy K Agrawal for all the illuminating discussions we had at various stages of this work. I also thank Prof. Kamales Kar, Prof. Pijushpani Bhattacharjee, Prof. Parthasarathi Majumdar and Prof. Debasish Majumdar for extending all kinds of help and support throughout my thesis work.

I also thank all the members of the Theory and Astroparticle Physics division of SINP for maintaining a cordial and comfortable working environment. I am sincerely thankful to Srijit, Soumini, Pratyay, Parijat, Pritibhajan, Lab and Avirup for their constant support and encouragements by maintaining an ambient atmosphere around my workplace. My thanks also to Chandrachur, Ayanda, Sayanda, Bhramardi, Baishali, Abhik, Arindam, Najmul, Kamakshya, Susmita, Santanu, Susnata, Raktim, Somdeb, Satyajit, Mainak, Abhishek, Anirban, Debabrata, Amit, Dipankar, Aminul, Amna and Richard for making the environment enjoyable. Thanks also to Pradyutda and Doladi for their help and support.

I am also grateful to my classmates Chiku, Anirban, Sarbani, Sanjoy, Abhisakh, Bishnu, Safiul, Nupur, Shryeoshi for a youthful company.

Finally, I wish to express my deep sense of gratitude to my parents for their immense patience, love, affection, encouragements and support. I am indebted to them for giving me the freedom to choose my own career and for constantly providing me the moral and emotional support at every stage of my life. It is only because of their kind blessings that I could complete this work.

Rana Nandi

Contents

List of Figures

List of Tables

Chapter 1

Introduction

1.1 General Introduction

Discovery of Pulsars [1] and its identification [2] as rotating neutron stars in 1968-69 generated a great flurry of interests in neutron star physics. Now they are believed to be remnants of supernova explosions which are the endpoint in the evolution of massive stars. All the quantities that characterize neutron stars are extreme. At the surface of the star the matter density is $\rho \lesssim 10^4$ g cm^{-3}, but at the core it can be a few times greater than the normal nuclear matter density ($\rho_o \simeq 2.8 \times 10^{14}$ g cm^{-3}). Various exotic forms of matter such as hyperons, quark-hadron mixed phase, Bose-Einstein condensate of kaons etc may appear at such high densities. Neutron Stars can also have very strong magnetic fields ($\sim 10^{12}$ G), very large spins (period P $\sim 10^{-3} - 1$ s) and very small spin down rates ($\dot{\mathrm{P}} \sim 10^{-15}$). We cannot have matters with these kind of extreme characteristics in our terrestrial laboratories; therefore neutron stars are very promising laboratories for studying matter under such extreme conditions. A wide variety of theoretical models exists in the literature to describe the properties of neutron star matter. Ultimately only one model which would successfully interpret all the observational data will survive in future.

1.2 Birth of a Neutron Star

Neutron stars are final products of stellar evolution and believed to be formed in supernova explosions. A typical star spends most of its luminous life in the hydrogen burning phase where hydrogen is fused to produce helium accompanied by the release of a huge amount of thermal energy, in the stellar core. The outward thermal pressure produced in this fusion process balances the inward gravitational pull and stabilizes the star. When the hydrogen is exhausted in the core the star begins to collapse due to its own gravity. The matter in the core gets heated due to this collapse and when the temperature is high enough helium fusion starts at the core with hydrogen continuing to burn in a outer shell surrounding the core. For stars with mass $M \lesssim 8M_{\odot}$, the burning process cannot proceed beyond helium fusion as the core temperature can never become high enough for further burning. Mainly carbon and oxygen are produced in helium burning and these reactions are very temperature sensitive - just a few percent rise in temperature can increase the reaction rate by manifolds. This makes the star very unstable and causes a huge pulsation to build up which eventually expels the whole envelope into the interstellar medium. The remaining carbon-oxygen core contracts under gravity but cannot attain enough temperature to burn carbon, as a large portion of the stellar mass has been lost to the interstellar medium. Eventually it becomes a white dwarf where the gravity is balanced by the electron degeneracy pressure.

For more massive stars ($M \gtrsim 8M_{\odot}$) the core goes through the subsequent burning of carbon, neon, oxygen, magnesium and silicon with the addition of concentric burning shells surrounding the core. This gives the star a onion-shell like structure (Fig. 1.1) with iron group elements (Fe, Ni, Co) which are the ash of silicon burning, at the center. Burning process ends at ^{56}Fe, as it is the most stable nucleus and therefore Fe burning is not energetically favorable. As there is no burning and therefore no outward thermal pressure in the core; it begins to collapse under gravity. The core also gains mass as the

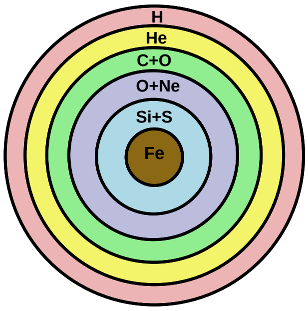

Figure 1.1: Onion-shell like structure of a massive star before core-collapse

ash of burning shells are added to it and when the mass exceeds the Chandrasekhar limit ($1.4\,M_\odot$), electron degeneracy pressure cannot balance the gravity and hence the core continues to collapse. Very soon the density become high enough so that the inverse beta decay, where a proton capture an electron to produce a neutron and a neutrino, becomes energetically favorable. As the core collapses further there is a huge loss of electrons by this process which in turn reduces the electron degeneracy pressure and thereby further accelerating the collapse. Neutrinos produced in this process interact very little with the matter and leave the star very quickly; but as the density reach $\sim 10^{12}$ g cm^{-3}, diffusion time scale of neutrinos become greater than the collapse rate and they get trapped inside the core. When the density inside the core exceeds the nuclear density ($\sim 2.8 \times 10^{14}$ g cm^{-3}), nuclei dissolve to form nuclear matter, and the short-range repulsion of nucleons together with the degeneracy pressure of nucleons, electrons as well as neutrinos resists further compression. This sudden halt in collapse generates a shock wave through the in-falling material and it eventually gathers sufficient energy to expel the whole stellar envelope in a spectacular event called supernova explosion. If the initial mass of the star is more than $20 M_\odot$, the remaining core collapses further to form a black hole, while for less massive stars the remnant form a neutron star. A newly born neutron star also called protoneutron star is initially very hot having a temperature of $10^{11} - 10^{12}$ K, but it cools down very fast by the emission of its trapped neutrinos and within a day the temperature drops to $10^9 - 10^{10}$ K. The neutron star continues its cooling through neutrino emission

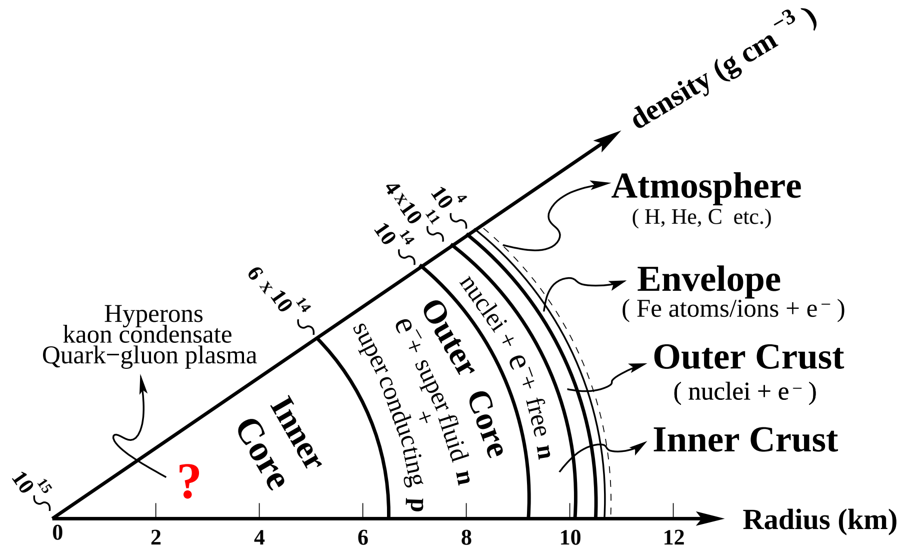

Figure 1.2: Interior of a typical neutron star

but in a much slower rate and in the later stage the cooling is dominated by emission of photons.

1.3 Structure and Composition of Neutron Stars

In a cold neutron star, the matter is in its absolute ground state in the sense that energy can't be lowered by any strong, weak or electromagnetic process. The ground state composition changes considerably with increasing density. Figure (1.2) shows a schematic picture of the interior of a neutron star. At the surface of the star there is an atmosphere with thickness of few centimeters and containing plasma of H, He and possibly a trace of heavier elements. Though it contains a negligible fraction of the total mass of the star, it is very important in the context of observations as the observed spectra of electromagnetic and thermal radiations originate in this region. Just below the atmosphere there is a thin envelope which is a few meter thick and contains ionized ^{56}Fe atoms along with a gas of non-relativistic electrons.

^{56}Fe nuclei become completely ionized at density $\sim 10^4$ g cm^{-3}, when the spacing between nuclei becomes small compared to the Thomas-Fermi radius of an isolated neutral atom. This can be taken as the starting point of the outer crust and it has thickness of a few hundred meters. The outer crust contains nuclei arranged in a body-centered cubic (bcc) lattice and immersed in a gas of free electrons which are relativistic above the density $\rho \sim 10^7$ g cm^{-3}. At $\rho \sim 10^4$ g cm^{-3}, ^{56}Fe is present as the equilibrium nucleus; but with increasing density the equilibrium nucleus become more and more neutron rich through electron capture process ($p + e^- \rightarrow n + \nu_e$). At a density $\sim 4 \times 10^{11}$ g cm^{-3}, the chemical potential of neutrons exceeds their rest mass and as a consequence neutrons begin to drip out of the nuclei. This point is called the neutron drip point and it marks the end of the outer crust and the beginning of the inner crust.

So the matter in the inner crust is made up of neutron-rich nuclei embedded in a neutron gas along with the uniform electron gas and it might have a thickness of about one kilometer. With increasing density, number of dripped neutrons as well as the volume fraction occupied by the nuclei increases. At the bottom layer of the crust when this volume fraction becomes $\gtrsim 50\%$, it may become energetically favorable for the nuclei to undergo a series of transitions from spherical shape to cylinder, slab, cylindrical bubble and spherical bubble with increasing density [3–5]. This is the so called pasta phase. Beyond $\rho \sim 10^{14}$ g cm^{-3}, nuclei no longer exist as they dissolve to form nuclear matter. This is defined as the crust-core boundary.

The outer core extends upto a density $\sim 2\rho_0$ and can have thickness of a few kilometers. It contains uniform matter of neutrons, protons, electrons and muons where electrons and muons make up ideal fermi gases and neutrons and protons form a strongly interacting fermi liquid. In this high density neutrons may behave as superfluid while protons can show superconductivity.

The inner core is the inner most part of a neutron star. The inner core along with the outer core accounts for most of the neutron star mass. The composition and the equation of state (EOS) of this dense region is very much model dependent and it has been proposed that various exotic forms of matter such as hyperons, quark-hadron mixed phase, Bose-Einstein condensate of kaons etc may appear at such extremely high densities.

1.4 Observational constraints

Since the theory of many-body interactions in dense matter is not fully developed yet, there exists a great number of theoretical models which give different EOSs for neutron star matter. To constrain these models we depend exclusively on neutron star observations, as the environment of neutron star interior cannot be reproduced in our laboratories in earth. Two most important ingredients in this regard are masses and radii of neutron stars. This is because each EOS of neutron star matter gives different mass-radius relationship and also predicts a different allowed maximum mass for a neutron star. So the accurate measurement of masses and radii of neutron stars can disqualify a theoretical model if the mass-radius relationship given by it does not satisfy measured values. Usually theoretical models that include exotic particles at the core give softer EOS which leads to a smaller maximum mass, as compared to the models which do not consider exotic particles. The observed maximum mass for neutron stars thus can limit the number of models by throwing away those which predict smaller maximum mass than that of the observed. Exactly this thing has happened very recently after an accurate measurement reveals a neutron star to have mass $1.97 \pm .04\, M_\odot$ [6] which is significantly larger than the earlier accurately measured neutron star masses and consequently some of the models have been ruled out [6].

Neutron stars emit radiations in all bands of electromagnetic spectrum. Various important informations on the surface temperature, chemical composition, magnetic field, mass, radius etc of neutron stars can be extracted from these spectra. Most of the neutron stars are observed as radio pulsars and more than two thousand (2008) [7] radio pulsars have been discovered so far of which 186 are in binaries which can be of two types

: PSR+NS and PSR+WD. In the first case the companion star is a neutron star while for the latter case it is a white dwarf. There are other types of binaries where the neutron star accrete matter from the companion and thereby emit X-rays. These are called X-ray binaries and are of two types: high mass X-ray binaries (HMXBs) and low mass X-ray binaries (LMXBs). In a HMXB, the companion is a massive star with mass $M_{com} > 10M_\odot$ and for LMXBs, companions are lighter than the sun.

1.4.1 Mass measurements

The mass of a neutron star can only be measured if it is in a binary. So far masses of only 58 neutron stars have been measured and are summarized by J M Lattimer [8] as shown in Fig. 1.3. In a binary system, stars closely follow the Keplerian orbits and this enables us to use the standard astronomical techniques to measure their masses. By measuring the radial velocity of one of the components we can evaluate five Keplerian parameters: the orbital period (P_b), the semi-major axis projected on the line of sight ($x_j = a \sin i$, i is the orbital inclination angle to the line of sight and a is the orbital separation), the eccentricity of the orbit (e), the periastron longitude (ω) and the time of periastron passage (T_0). These parameters give two independent equations relating four unknowns: M_1, M_2, a, and $\sin i$ and therefore we have to search for other means to obtain other two equations.

In X-ray binaries neutron stars are observed in X-rays and companions are mainly optical but may also be seen in other bands (near infrared, ultraviolet etc). In this case the third equation, namely the mass ratio ($q = M_1/M_2$), can be obtained by measuring the radial velocity of the other component. For eclipsing binaries another equation can be obtained by measuring the eclipse duration and relating it to the inclination angle ($\sin i$). The knowledge of the Roche lobe radius (R_L) and the factor $\beta(=R/R_L$, where R is the radius of the companion) can also be important to constrain the inclination angle. Among the 14 X-ray binaries listed in the Fig. 1.3, 9 are HMXBs all of which show eclipses

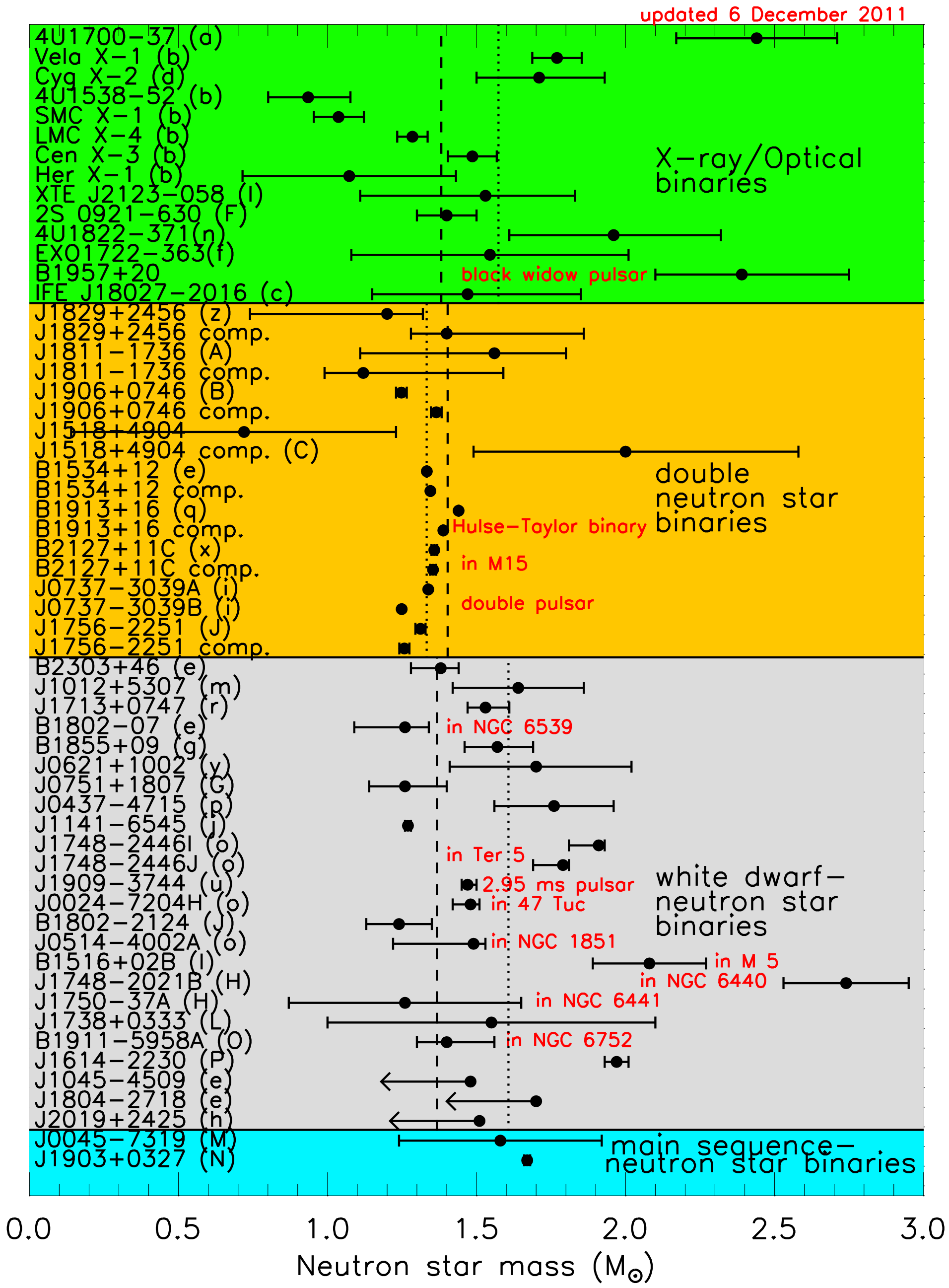

Figure 1.3: Measured masses of neutron stars [8]

and therefore presumably have enough observational data to calculate their masses. But the figure shows large uncertainties in the mass measurements and for most of the cases these arise due to the deviation of the radial velocity profile of the optical companions from the expected Keplerian profiles. The most accurate mass measurements have been done for LMC X-4, but its mass ($M_1 = 1.285 \pm 0.051 M_\odot$) is too low to constrain the EOS. The most interesting candidate in this set is the 4U1700-377 with measured mass of $2.44 \pm 0.27 M_\odot$, but there are some speculations that the compact star may be a black hole instead of a neutron star [9]. We hope further observations will resolve the issue and if it turns out to be a neutron star it will greatly constrain the neutron star EOS and possibly rule out all the exotic EOSs. There are also 5 LMXBs in the list out of which 4U1822-371 ($M_1 = 1.96^{+0.36}_{-0.35} M_\odot$) and B1957+20 ($M_1 = 2.39^{+0.36}_{-0.29} M_\odot$) may be massive, but unfortunately the uncertainties are too large to draw any definite conclusion.

In PSR+NS and PSR+WD binaries both the components are compact objects and this gives us very good opportunity to study the effects of general relativity on their orbital motions. From the pulsed radio emission of pulsars one can easily measure their radial velocities which give first two relations to measure the masses of both the components. For other two relations one tries to measure at least two of the five general relativistic post-Keplerian (PK) parameters [10]: the periastron advance ($\dot{\omega}$), the time dilation or gravitational redshift (γ), the orbital period decay ($\dot{P}_b$) and the range (r) and shape (s) of the Shapiro delay. The Periastron advance is only measurable if the eccentricity of the orbit is large. By measuring it one can get the third relation namely the total mass ($M = M_1 + M_2$) of the binary system. The parameter γ contains the quadratic Doppler effect as well as the gravitational redshift in the field of the companion. This can also give an independent relation for eccentric binaries. The third parameter $\dot{P}_b$ arises due to the emission of gravitational radiation and measurable for binaries with small periods ($P_b \lesssim 12$ hours). There can be an extra delay in pulse arrival if the signal travels close to the compact companion. This delay is called Shapiro delay and best detected for binaries with large orbital inclination. These gives two independent relations through the parameters r and s.

Figure 1.3 contains 9 PSR+NS binaries containing 18 neutron stars, masses of which are obtained by measuring the radial velocities of the pulsars as well as some of the PK parameters. As can be seen from the figure, except for J1829+2456, J1811-1736 and J1518+4904, masses of these binaries are measured with very good accuracy. The Husle-Taylor pulsar (B1913+16) is the first radio pulsar detected in a binary and its mass (1.4398 ± 0.0002) is the most accurately measured neutron star mass so far. The binary containing J037-3030A and J037-3030A is an unique system where both the neutron stars are radio pulsars and it helped to determine their masses precisely. But, unfortunately the masses are too small to constrain the EOS. There is only one candidate J1518+4904 which can contain a massive neutron star but the error in mass measurement ($M_2 = 2.00^{+0.58}_{-0.51}$) is very large because of the fact that the orbit of this binary is very wide so that it is very difficult to measure the PK parameters other than $\dot{\omega}$ [11].

For NS+WD binaries also PK parameters can only be measured if they are compact enough as for wide binaries relativistic effects are very weak. But, luckily additional relations for these systems can be obtained by optical observations of white dwarf components [12]. Masses of white dwarfs can be obtained in several ways [13]. For example, by estimating the radius from direct measurements of optical flux, effective temperature and the distance, the mass can be determined from the theoretical mass-radius relationship. Also, from the measurement of the surface gravity, the mass of a white dwarf can be estimated. For binary millisecond pulsars the mass of the white dwarf companion can also be obtained from the relation between P_b and M_2 [14]. Till date masses of 24 NS-WD binaries have been measured as shown in the fig. 1.3. Here the most accurately measured mass is of the pulsar J1141-6545. This is because the binary system is very compact and eccentric and that allow one to measure the PK parameters accurately. The mass (1.97 ± 0.04) of the pulsar J1614-2230 is the highest accurately measured mass so far and it has ruled out some of the exotic EOSs. The accurate measurement of the mass, done by Demorest *et al* [6] in 2010, was possible because of the high orbital inclination ($i \simeq 89^\circ$), which allowed the very precise determination of the Shapiro delay parameters, of the system. There are two interesting binaries, B1516+02B and J1748-2021B, which can have neutron stars with mass beyond $2M_\odot$. For B1516+02B the measured mass is $2.08 \pm 0.19 M_\odot$, so the error should be narrowed down by future observations to confirm that possibility. The measured mass for the J1748-2021B is 2.74 ± 0.21 i.e. even the lower limit gives a mass greater than $2.5M_\odot$. In this measurement the total mass of the system was deduced by measuring the periastron advance ($\dot{\omega}$) of the system with the assumption that $\dot{\omega}$ was fully relativistic and had no contribution from the tidal or rotational deformation of the companion [15]. But any such contribution make the measurement unreliable and therefore further investigations are needed to justify the assumption. Anyway, J1748-2021 along with the two X-ray binaries 4U1700-377 and B1957+20 seem to be the strongest candidates to further constrain the EOS of neutron star matter in future.

1.4.2 Radius measurements

Simultaneous knowledge of mass and radius with very good accuracy is necessary to constrain the neutron star EOS, as already discussed in the beginning of this section. Although masses of several neutron stars have been measured quite accurately, (unfortunately) there is no radius measurement available for them. However, there exist some methods by which one can try to measure the radius of a neutrons star.

In one such approach the radius of a neutron star is measured by analyzing the thermal spectrum emitted from its surface. Assuming the emission as blackbody the radiation radius (R_∞) of a star can be obtained from the relation

$$F_\infty = \left(\frac{R_\infty}{d}\right)^2 \sigma_B T_\infty^4, \tag{1.1}$$

where F_∞ is the redshifted radiation flux at the earth and is found by measuring the intensity of the radiation, T_∞ is the redshifted surface temperature determined from the position of spectral maximum, d is the distance of the star with respect to the observer and σ_B is the Stefan-Boltzmann constant. The radius R of the star then can be obtained from

$$R = R_\infty (1+z)^{-1}, \tag{1.2}$$

if the gravitational redshift (z) is known. However, various systematic uncertainties can enter in the determination of R_∞. Inaccuracy in the measurement of distance of the star is a major source of uncertainty. Temperature may not be uniform over the stellar surface as assumed in Eq. (1.1). The detected spectrum may get distorted due to the absorption in the interstellar hydrogen gas the column density of which is poorly known. The real radiation spectrum deviates from that of a blackbody and is difficult to simulate as it depends on various things such as the chemical composition of the atmosphere, the surface gravity, magnetic field etc of the neutron star all of which are not that well known. Clearly, measurements will be reliable only if most of these uncertainties can be controlled.

There are several isolated neutron stars like Geminga (PSR B0633+17), Vela (PSR B0833-45), PSR B0656+14, RX J1856-3754 etc for which radius measurements have been performed. From optical studies of Geminga and taking its distance to be $\sim$ 160 pc as obtained by parallax measurements [16], Golden & Shearer [17] first estimated the radius of Geminga as $R_\infty \lesssim 10$ km. Later considering large uncertainties in d, Haensel [18] obtained the limit $R_\infty \lesssim 17.6$ km, which is too weak to constrain the EOS. Radius of Vela pulsar was estimated by Mori *et al.* [19] by spectral analysis of XMM-Newton observations. For spectral fitting they use a two-component model made up of a thermal (blackbody or magnetized hydrogen atmosphere) as well as a non-thermal (power-law) spectrum. With blackbody fit they obtained $R_\infty = 2.5 \pm 0.2$ km which may be attributed to the thermal radiation of a hot polar cap on the stellar surface. For the hydrogen atmosphere model the inferred radius was $R_\infty = 15.0^{+6.5}_{-5.1} \times d/(294\,\mathrm{pc})$ km, where 294 pc is the measured distance [16] of the Vela pulsar by parallax method. For the PSR B0656+14 the parallax measurement gives $d = 288^{+33}_{-27}$ pc [20]. Fit of the thermal X-ray spectra with a magnetized hydrogen atmosphere model yields $13 \lesssim R_\infty/km \lesssim 20$ [20]. RX J1856.5-3754 is an another isolated neutron star interesting for radius measurements. The most recent radius estimate of this source has been done by Sartore *et al.* [21]. They used the data taken by XMM-Newton satellite between 2002 and 2011 and fit them with two blackbody models: one is hard with a temperature of $kT^h_\infty = 62.4^{+0.6}_{-0.4}$ and emission radius of $R^h_\infty = 4.7^{+0.2}_{-0.3}(d/120\,\mathrm{pc})$ km while the other one is soft with temperature of $kT^s_\infty = 38.9^{+4.9}_{-2.9}$ and emission radius of $R^s_\infty = 11.8^{+5.0}_{-0.4}(d/120\,\mathrm{pc})$ km. The soft spectrum can be associated with the emission from the whole surface while the hard spectrum corresponds to the emission from a hot polar cap and when taken together they give a radiation radius of $R_\infty = \sqrt{R^{s2}_\infty + R^{h2}_\infty} = 12.7^{+4.6}_{-0.2}(d/120\,\mathrm{pc})$ km. The measured parallax distance of this pulsar is $d = 123^{+11}_{-15}$ pc [22], which implies $R_\infty = 13.0^{+6.3}_{-1.8}$ km. In all the last three cases the uncertainties in R_∞ measurements are not small enough to be useful for containing the EOS.

LXMBs that exhibit thermonuclear bursts are very good candidates to constrain the neutron star EOS. These bursts are called type-I X-ray bursts and occur due to the unstable ignition of nuclear burning (mainly helium) in the accreted matter on a neutron star surface. Some of these bursts are so intense that the radiation pressure can temporarily lift the photosphere off the neutron star surface. During such a photospheric radius expansion (PRE) bursts, initially the temperature decreases while the flux increases rapidly. As the photosphere comes down, the temperature increases and the flux decreases. Gradually the photosphere settles down on the surface and the temperature decreases again as the star begins to cool [23]. It is generally assumed [24] that at touchdown (when the photosphere touches the stellar surface), the temperature becomes maximum, the radius of the photosphere (r_{ph}) becomes equal to the stellar radius (R) and the corresponding flux is equal to the Eddington limited flux given by

$$F_{\mathrm{edd},\infty} = \frac{GMc}{\kappa d^2}\sqrt{1 - 2GM/c^2R}, \tag{1.3}$$

where the opacity of the atmosphere is $\kappa = 0.2(1 + X)$ cm^2 g^{-1}, X is the hydrogen mass fraction. The relation is obtained by assuming electron scattering as the dominant process. After the burst, the star gradually reaches the quiescent state and the ratio $F_\infty/\sigma_B T_\infty^4$ becomes almost constant :

$$\frac{F_\infty}{\sigma_B T_\infty^4} = f_c^{-4}\left(\frac{R}{d}\right)^2\left(1 - \frac{2GM}{c^2R}\right)^{-1}, \tag{1.4}$$

where $f_c = T_\infty/T_{\mathrm{eff}}$ is the color correction factor which accounts for the deviation of the spectrum from a blackbody and depends on the composition of the atmosphere, surface gravity and T_{eff} [25]. Combining eqs. (1.3), (1.4) and the expression for redshift $z = (1 - 2GM/c^2R)^{-1/2} - 1$, following relations are obtained :

$$\begin{aligned}
M &= \frac{f_c^4 c^5}{4G\kappa}\frac{F_\infty}{\sigma_B T_\infty^4}[1-(1+z)^{-2}]^2(1+z)^{-3}F_{\mathrm{edd},\infty}^{-1}\,,\\
R &= \frac{f_c^4 c^3}{2\kappa}\frac{F_\infty}{\sigma_B T_\infty^4}[1-(1+z)^{-2}](1+z)^{-3}F_{\mathrm{edd},\infty}^{-1}\,,\\
d &= \frac{f_c^2 c^3}{2\kappa}\frac{F_\infty}{\sigma_B T_\infty^4}[1-(1+z)^{-2}](1+z)^{-3}F_{\mathrm{edd},\infty}^{-1}\,.
\end{aligned} \tag{1.5}$$

So, for neutron stars that undergo PRE bursts, simultaneous determination of mass, radius and distance is possible if $F_{\mathrm{edd},\infty}$, $F_\infty/\sigma_B T_\infty$ as well as z could be measured from observations and sufficient knowledge of κ and f_c could be acquired. Using this procedure Özel (2006) [24] determined the mass ($M = 2.10 \pm 0.28 M_\odot$), radius ($R = 13.8 \pm 1.8$ km) and distance ($d = 9.2 \pm 1.0$ kpc) of the source EXO 0748-676 and claimed to rule out all the soft EOSs. If the redshift of the star is unknown then the mass and radius can be calculated using eqs. (1.2), (1.3) and (1.4) and with the knowledge of the stellar distance. PRE burst sources that reside in globular clusters (GCs) are good candidates for this method as their distances can typically be measured with good accuracy. Özel *et al* (2009) [26] applied this method to a neutron star EXO 1745-248 residing in the GC Terzan 5 and obtained tightly constrained pairs of values for the mass and radius centered around $M = 1.4M_{\odot}$ and $R = 11$ km or around $M = 1.7M_{\odot}$ and $R = 9$ km. By similar approach Güver *et al* [27, 28] determined masses and radii of two LXMBs, 4U1608-522 and 4U1820-20. For 4U1608-522 they found $M = 1.74 \pm 0.14M_{\odot}$ and $R = 9.3 \pm 1.0$ km and $M = 1.58 \pm 0.06M_{\odot}$ and $R = 9.1 \pm 0.4$ km for 4U1820-20. The last three results give stringent constraints on the neutron star mass and radius with Özel *et al* (2010) [30] claiming that these results disfavor any EOS that contains only nucleons. However, Steiner *et al* (2010) [29] found internal inconsistency in these calculations and they argued that the inconsistency can be removed by relaxing the assumption that $r_{ph} = R$ at touchdown point, which is identified from the maximum in T_{∞}. Considering extended photosphere corresponding to T_{∞} maximum, they obtained larger values for radii and substantially larger confidence intervals for masses and radii and therefore could accommodate a larger number of EOSs some of which contain only nucleons.

Quiescent LMXBs (qLMXBs) which spend long periods in quiescent states between episodes of accretions, are very good candidates for the mass and radius measurements, because of several reasons: (i) there atmospheres are composed of pure hydrogen as heavier elements obtained from accretions gradually sink in, (ii) they have very small magnetic fields as no pulsations or cyclotron spectral features are observed from them, (iii) their distances can be measured from PRE bursts or if they reside in globular clusters. Therefore, fitting the spectra with a nonmagnetic hydrogen atmosphere model and using eqs. (1.1) and (1.2), one can estimate the mass and radius of a qLMXB. Using this approach most accurate radii which were useful to constrain the neutron star EOS [29,31], so far are obtained for qLMXBs in globular cluster ω Cen, in M13 [31], for U24 in NGC 6397 [32] and for X7 in 47 Tuc [33].

1.4.3 Measurements of moment of inertia

So far the most reliable determination of moment of inertia (I) has been done for the Crab pulsar by Bejger and Haensel (2003) [34]. Assuming a time dependent acceleration for the expansion of the Crab nebula and using the estimates of the mass ($4.6 \pm 1.8 M_\odot$) [35] contained in the optical filaments they obtained a lower bound for the moment of inertia of the Crab pulsar, but unfortunately it could rule out only very soft EOSs. However, moment of inertia measurements of relativistic binary systems can be a very important tool to constrain the neutron star EOS. In this context, PSR J0737-3039A of the double pulsar system is the most suitable candidate. Since $I \propto MR^2$ and mass of this pulsar has been measured with good accuracy, measurement of I will allow an accurate determination of its radius. Moment of inertia of such an object can be determined by measuring the spin-orbit coupling [36, 37], which contributes to the motion of the system in two ways. In one hand it causes an extra advancement in the periastron angle (ω) and on the other hand it induces a precession of the orbital plane around the direction of the total angular momentum of the system. According to Lattimer *et al* (2005) [37], moment of inertia of PSR J0737-3039A could be measured within 10% accuracy with few years of future observations and that could put stringent constraint on the neutron star EOS.

1.4.4 Other constraints

Apart from these methods there are several other methods that can be applied to constrain the neutron star EOS. Detection of gravitational waves can be very useful to know about the neutron star interior. Relativistic binaries (NS+NS or NS+WD) which are close to the merging state, are thought to be very good source of gravitational waves. Such waves can also be emitted from a rapidly rotating neutron star if it looses its axial symmetry. Other potential methods are study of seismic oscillations of isolated neutron stars, quasi-periodic oscillations from LMXBs, analysis of pulse profiles in X-ray pulsars etc.

Table 1.1: List of magnetar candidates [40]

	Name	**Period (P) (s)**	**dP/dt (10^{-11})**	**B_{surf} (10^{14} G)**
SGRs	SGR 0526-66	8.0544(2)	3.8(1)	5.6
	SGR 1900+14	5.19987(7)	9.2(4)	7.0
	SGR 1806-20	7.6022(7)	75(4)	24.0
	SGR 1627-41	2.594578(6)	1.9(4)	2.2
	SGR 0501+4516	5.76209653(3)	0.582(3)	1.9
	SGR 0418+5729	9.07838827(4)	< 0.0006	< 0.075
	SGR 1833-0832	7.5654091(8)	0.439(43)	1.8
	Swift J1822.3-1606*	8.43771968(6)	0.0254(22)	0.47
	Swift J1834.9-0846*	2.4823018(1)	0.796(12)	1.4
	SGR 1801-23*	–	–	–
	SGR 2013+34*	–	–	–
AXPs	4U 0142+61	8.68832877(2)	0.20332(7)	1.3
	1E 1048.1-5937	6.457875(3)	~ 2.25	3.9
	1E 2259+586	6.9789484460(39)	0.048430(8)	0.59
	1E 1841-045	11.7828977(10)	3.93(1)	6.9
	1E 1547.0-5408	2.06983302(4)	2.318(5)	2.2
	1RXS J170849.0-400910	11.003027(1)	1.91(4)	4.6
	XTE J1810-19	5.5403537(2)	0.777(3)	2.1
	CXOU J010043.1-721134	8.020392(9)	1.88(8)	3.9
	CXO J164710.2-455216	10.6106563(1)	0.083(2)	0.95
	CXOU J171405.7-381031*	3.82535(5)	6.40(14)	5.0
	PSR J1622-4950*	4.3261(1)	1.7(1)	2.8
	AX J1845-0258*	6.97127(28)	–	–

* marked candidates are unconfirmed.

1.5 Magnetars

Recent discoveries of magnetars have created renewed interests in neutron star research. Magnetars are highly magnetized neutron stars [38] having surface magnetic fields $\sim 10^{14} - 10^{15}$ G which are 2-3 order of magnitude larger than the ordinary neutron stars. They also have larger spin periods ($P \sim 2 - 12$ s) and spin down rates ($dP/dt \sim 10^{-13} - 10^{-10}$) as compared to the ordinary neutron stars.

Magnetars consist of mainly two types of stars [39] - Anomalous X-ray Pulsars (AXPs: 12 objects; 9 confirmed and 3 candidates) and Soft Gamma-ray Repeaters (SGRs: 11 objects; 7 confirmed and 4 candidates) [40], as summarized in table 1.1. In most of the cases their quiescent X-ray luminosity exceeds their rotational energy loss rate. SGRs emit sporadic X-ray and γ-ray bursts (Luminosity, $L \sim 10^{38} - 10^{41}$ erg/s) of sub-second duration with occasional emission of much stronger γ-rays called Giant Flares having luminosity ($L \sim 10^{44} - 10^{46}$ erg/s) much greater than the Eddington limit. Only three such flares have been observed so far one each for SGR 0526-66 (March, 1979), SGR 1900+14 (August, 1998) and SGR 1806-20 (December, 2004). In the decaying tail of last two flares, a number of long-lasting, quasi-periodic oscillations (QPOs) have been detected having frequencies in the range 18-1800 Hz [41]. Study of these QPOs can give us important information about the neutron star interior. Some of AXPs also display X-ray bursts which are less energetic than that of SGRs. Unlike accreting pulsars, their emission spectra don't have any optical component and also their X-ray emissions are much softer as compared with the accreting pulsars [42].

Features of SGRs and AXPs are best explained by the magnetar model [43]. In this model SGRs and AXPs are assumed to be powered by extremely strong magnetic fields. Such strong magnetic fields might be generated by dynamo processes in newly born neutron stars [45]. Strong magnetic fields act as strong brake on magnetars' rotation and thereby explain their large spin down rate [39] and hence large period. Decay of such ultra-strong magnetic fields are thought to be responsible for their high-luminosity bursts as well as persistent emission of X-rays [43]. Giant flares of SGRs are caused by magnetic instabilities analogous to earthquakes.

This thesis studies various properties of ordinary neutron stars as well as magnetars and can be divided into two main parts. In the first part it describes the ground state properties such as composition, equation of state (EOS) of the outer crust (Chapter 2) as well as the inner crust (Chapter 3) of neutron stars, with and without magnetic fields. Effects of strong magnetic fields on the shear modulus of the neutron star crust and its influence on the calculations of torsional shear mode frequencies are also investigated in this part (Chapter 4). The calculation of transport properties especially the shear viscosity of antikaon (K^-) condensed matter in neutron star core are studied in the second part (Chapter 6). This part also studies the role of neutrino shear viscosity on the nucleation time of K^- droplets in neutrino-trapped matter of newly born neutron stars called proto-neutron stars (Chapter 7).

Chapter 2

The Outer Crust

2.1 Introduction

Outer crust of a neutron star is the region just below the thin envelope at its surface and extending upto a few hundred meters (Sec. 1.3). Although the crust contains only a few percent of the neutron star mass, the knowledge of it is very important to understand various aspects of neutron star evolution and dynamics. The temperature of the neutron star core can be estimated from the observed X-ray flux, if the thermal conductivity of the crust which controls the heat transport from the core to the surface, is known. Electrical conductivity of the crust is necessary to understand the evolution of magnetic fields of pulsars. The presence of nuclear lattice in the crust is mandatory to explain the glitches in the rotational frequency of radio pulsars. A rapidly rotating neutron star can emit gravitational waves if its shape undergoes non-axial deformations, which can only be supported by the solid crust. Solid nature of the crust also supports the excitation of torsional shear modes (Chapter 4) .

Discovery of magnetars has greatly enhanced the interest in the study of neutron star properties in the presence of strong magnetic fields [44]. Their surface magnetic fields could be quite large $\sim 10^{14} - 10^{15}$ G, as predicted by observations on SGRs and AXPs

(Sec. 1.5). Such strong magnetic fields might be generated by dynamo processes in newly born neutron star [45]. Inside the star the magnitude of the fields may be even higher. The limiting interior field strength is set by the virial theorem and for a typical neutron star of mass $1.5M_{\odot}$ and radius 10 km this comes out to be $\sim 10^{18}$ G [46]. Such high magnetic fields can have significant effects on the equilibrium composition and the equation of state of the neutron star crust as well as the core [46, 47].

Nonmagnetic equilibrium composition and equation of state for the outer crust of cold neutron stars was reported in a seminal paper by Baym, Pethick and Sutherland (BPS) [48]. Outer crust begins at a density $\rho \sim 10^4$ g cm^{-3} and contains nuclei arranged in a body-centered cubic (bcc) lattice which minimizes the Coulomb energy, and immersed in a gas of free electrons which become relativistic above the density $\rho \sim 10^7$ g cm^{-3}. Though the lattice effect is small on the equation of state, it changes the equilibrium nucleus to a heavier one and lowers the total energy of the system by reducing the coulomb energy of the nucleus. At lower densities $\rho \sim 10^4 - 10^7$ g cm^{-3}, ^{56}Fe is present as the equilibrium nucleus, but with increasing density equilibrium nuclei become increasingly neutron rich through electron capture process. At a density $\rho \simeq 4 \times 10^{11}$g cm^{-3} neutrons begin to drip out of nuclei - this is called the neutron drip point which marks the end of the outer crust.

The composition and equation of state of the outer crust of nonaccreting cold neutron stars in the presence of strong magnetic fields were first studied by Lai and Shapiro [46]. Magnetic fields may influence the ground state properties of crusts either through magnetic field and nuclear magnetic moment interaction or through Landau quantization of electrons. In a magnetic field $\sim 10^{17}$ G, magnetic field and nuclear magnetic moment interaction would not produce any significant change [49]. However such a strong magnetic field is expected to influence charged particles such as electrons in the crust through Landau quantization. If the magnetic field is very strong then electrons occupy only the low-lying Landau levels and it may affect the sequence of nuclei and the equation of state as well as any nonequilibrium β-processes [46].

This chapter is organized in the following way. In the next section we discuss the effect of strong magnetic fields on the motion of electrons. We revisit the magnetic BPS model [46] adopting recent experimental and theoretical nuclear mass tables in Section 3. Results are discussed in section 4. Section 5 contains the summary and conclusions.

2.2 Landau quantization of electrons

In the presence of a magnetic field, the electron motion is Landau quantized in the plane perpendicular to the field. We take the magnetic field ($\overrightarrow{B}$) along Z-direction and assume that it is uniform throughout the outer crust. If the field strength exceeds a critical value $B_c = m_e^2/e \simeq 4.414 \times 10^{13}$G (we use natural unit i.e. $\hbar$ = c = 1), which is obtained by equating the electron cyclotron energy with its rest-mass energy, then electrons become relativistic. The energy eigenvalue of relativistic electrons in a quantizing magnetic field is given by

$$E_e(\nu, p_z) = \left[p_z^2 + m_e^2 + 2\nu eB\right]^{1/2}, \tag{2.1}$$

where p_z is the Z-component of momentum, and ν is the Landau quantum number. The Fermi momenta of electrons ($p_{f_e}(\nu)$) are obtained from electron chemical potential μ_e as

$$p_{f_e}(\nu) = \sqrt{\mu_e^2 - (m_e^2 + 2\nu eB)}\,. \tag{2.2}$$

The number density of electrons in a magnetic field is calculated as

$$n_e = \frac{eB}{2\pi^2}\sum_0^{\nu_{max}} g_\nu p_{f_e}(\nu), \tag{2.3}$$

where g_ν is the spin degeneracy :

$$\begin{aligned} g_\nu &= 1 \ \text{for} \ \nu = 0 \\ &= 2 \ \text{for} \ \nu \geq 1, \end{aligned} \tag{2.4}$$

and ν_{max} is the maximum Landau quantum number given by

$$\nu_{max} = \frac{\mu_e^2 - m_e^2}{2eB}. \tag{2.5}$$

Energy density of the electron gas is,

$$\begin{aligned}
\varepsilon_e &= \frac{eB}{2\pi^2}\sum_{\nu=0}^{\nu_{max}} g_\nu \int_0^{p_{f_e}(\nu)} E(\nu, p_z)dp_z & (2.6)\\
&= \frac{eB}{4\pi^2}\sum_{\nu=0}^{\nu_{max}} g_\nu \left[p_{f_e}(\nu)\mu_e + (m_e^2 + 2\nu eB)\ln\frac{p_{f_e}(\nu)+\mu_e}{\sqrt{m_e^2+2\nu eB}}\right], & (2.7)
\end{aligned}$$

and the pressure is calculated as

$$\begin{aligned}
P_e &= \mu_e n_e - \varepsilon_e & (2.8)\\
&= \frac{eB}{4\pi^2}\sum_{\nu=0}^{\nu_{max}} g_\nu \left[p_{f_e}(\nu)\mu_e - (m_e^2 + 2\nu eB)\ln\frac{p_{f_e}(\nu)+\mu_e}{\sqrt{m_e^2+2\nu eB}}\right]. & (2.9)
\end{aligned}$$

2.3 Magnetic BPS Model

We revisit the BPS model to find the sequence of equilibrium nuclei and calculate the equation state of the outer crust in the presence of strong magnetic fields $B \sim 10^{17}$G [46]. In this calculation, we include the finite size effect in the lattice energy and adopt recent experimental and theoretical mass tables. Nuclei are arranged in a bcc lattice in the outer crust. Here we adopt the Wigner-Seitz (WS) approximation, where the whole lattice is divided into electrically neutral WS cells containing only one nucleus at the center. WS cells are taken to be spherical in shape and assumed to be charge neutral such that it contains exactly Z number of electrons, where Z is the nuclear charge. The Coulomb interaction between cells is neglected. To find an equilibrium nucleus (A,Z) at a given pressure P one has to minimize the Gibbs free energy per nucleon with respect to A and

Z. The total energy density of the system is given by

$$E_{tot} = n_N(W_N + W_L) + \varepsilon_e(n_e). \tag{2.10}$$

The energy of the nucleus (including rest mass energy of nucleons) is

$$W_N = m_n(A - Z) + m_p Z - bA, \tag{2.11}$$

where b is the binding energy per nucleon. Binding energies for experimental nuclear masses are obtained from the atomic mass table compiled by Audi *et al* (2003) [50]. For the rest of nuclei we use the theoretical extrapolation of Möller et al (1995) [51]. W_L is the lattice energy of the cell and is given by [52]

$$W_L = -\frac{9}{10}\frac{Z^2e^2}{r_C}\left(1 - \frac{5}{9}\left(\frac{r_N}{r_C}\right)^2\right) . \tag{2.12}$$

Here r_C is the cell radius and $r_N \simeq r_0 A^{1/3}$ ($r_0 \simeq$1.16 fm) is the nuclear radius. The first term in W_L is the lattice energy for point nuclei and the second term is the correction due to the finite size of the nucleus (assuming a uniform proton charge distribution in the nucleus). Further ε_e is the electron energy density which in absence of magnetic fields is given by

$$\varepsilon_e = \frac{1}{\pi^2}\int_0^{p_{f_e}} p^2 dp \sqrt{p^2 + m_e^2} \tag{2.13}$$

$$= \frac{1}{8\pi^2}\left[p_{f_e}\mu_e(\mu_e^2 + m_e^2) - m_e^4 \ln\left(\frac{p_{f_e} + \mu_e}{m_e}\right)\right] , \tag{2.14}$$

with $\mu_e = \sqrt{p_{f_e}^2 + m_e^2}$, where p_{f_e} is the fermi momentum of electrons. In presence of magnetic fields we use the results given in the previous section (Eq. (2.7)).

The total pressure P is given by

$$P = P_e + \frac{1}{3} W_L n_N \,, \tag{2.15}$$

where P_e is the pressure of the electron gas and can be calculated using Eq. (2.8), and the second term is the lattice pressure.

The nucleon number density n_N is related to the baryon number density n_b as

$$n_b = A n_N \,, \tag{2.16}$$

and the charge neutrality condition gives

$$n_e = Z n_N \,. \tag{2.17}$$

At a fixed pressure P, we minimize the Gibbs free energy per nucleon

$$g = \frac{E_{tot} + P}{n_b} = \frac{W_N + 4/3 W_L + Z\mu_e}{A}, \tag{2.18}$$

by varying A and Z.

2.4 Results

In Fig. 2.1, electron number density is plotted with mass density for different values of magnetic fields ($B_* = B/B_c$). For $B_* \leq 10^3$, large number of Landau levels are populated. Consequently there is no significant change in the electron number density compared with that of the field free case. However there is a significant enhancement in electron number density for magnetic fields $B_* = 2.3 \times 10^3$ ($\simeq 10^{17}$ G) or higher. This happens because only the zeroth Landau level gets populated for the whole mass density range in such high values of the magnetic field [53]. Fig. 2.2 shows the EOS i.e. the pressure as a function of

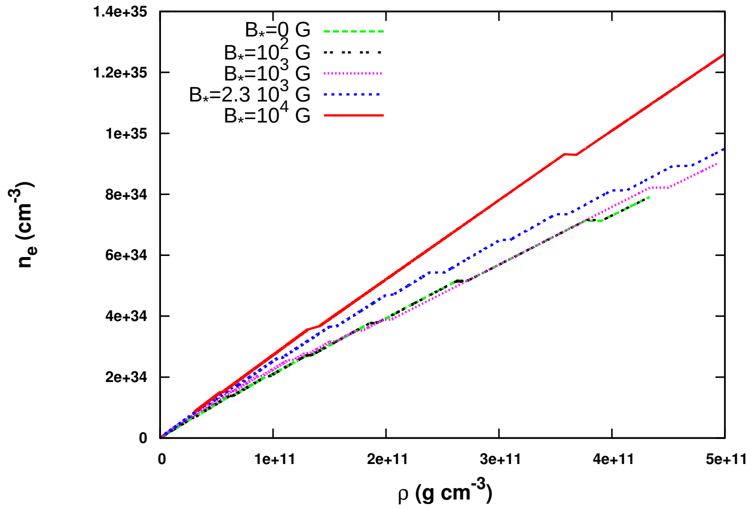

Figure 2.1: Electron number density as a function of mass density for different magnetic field strengths.

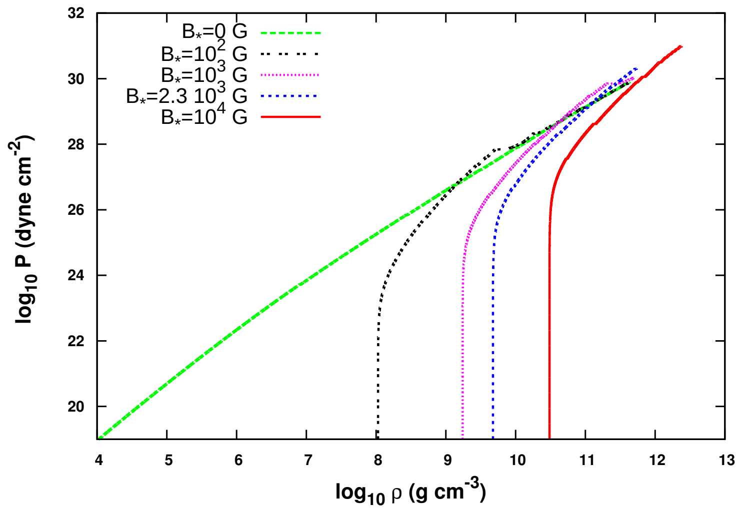

Figure 2.2: EOS of the outer crust in presence of magnetic fields

Table 2.1: Sequence of nuclei in the outer crust of neutron stars in presence of magnetic fields

Nuc	$\rho_{\max}$ (g/cm^3)						
	Z	N	$B_* = 0$	$B_* = 10^2$	$B_* = 10^3$	$B_* = 2.3 \times 10^3$	$B_* = 10^4$
^{56}Fe	26	30	8.03×10^6	4.68×10^8	4.32×10^9	9.29×10^9	–
^{60}Ni	28	32	–	–	–	–	5.33×10^{10}
^{62}Ni	28	34	2.72×10^8	1.68×10^9	1.83×10^{10}	4.06×10^{10}	1.31×10^{11}
^{64}Ni	28	36	1.34×10^9	2.78×10^9	2.34×10^{10}	–	–
^{66}Ni	28	38	1.50×10^9	–	–	–	–
^{88}Sr	38	50	–	–	2.59×10^{10}	6.44×10^{10}	3.58×10^{11}
^{86}Kr	36	50	3.10×10^9	3.87×10^9	4.33×10^{10}	1.04×10^{11}	5.37×10^{11}
^{84}Se	34	50	1.06×10^{10}	1.20×10^{10}	6.34×10^{10}	1.50×10^{11}	6.61×10^{11}
^{82}Ge	32	50	2.79×10^{10}	2.89×10^{10}	8.69×10^{10}	1.99×10^{11}	–
^{80}Zn	30	50	6.11×10^{10}	6.18×10^{10}	1.14×10^{10}	–	–
^{78}Ni	28	50	9.29×10^{10}	9.37×10^{10}	–	–	–
^{132}Sn	50	82	–	–	–	2.39×10^{11}	1.15×10^{12}
^{128}Pd	46	82	–	–	1.29×10^{11}	3.01×10^{11}	1.42×10^{12}
^{126}Ru	44	82	1.29×10^{11}	1.30×10^{11}	1.51×10^{11}	3.50×10^{11}	1.62×10^{12}
^{124}Mo	42	82	1.86×10^{11}	1.87×10^{11}	1.73×10^{11}	4.00×10^{11}	1.83×10^{12}
^{122}Zr	40	82	2.64×10^{11}	2.63×10^{11}	1.98×10^{11}	4.54×10^{11}	2.05×10^{12}
^{120}Sr	38	82	3.77×10^{11}	3.78×10^{11}	4.34×10^{11}	5.18×10^{11}	2.32×10^{12}
^{118}Kr	36	82	4.34×10^{11}	4.35×10^{11}	4.92×10^{11}	5.53×10^{11}	2.40×10^{12}

density of the outer crust in presence of magnetic fields. As in Ref. [46], strong magnetic fields are found to shift zero-pressure densities to higher values. We obtain the sequence of equilibrium nuclei by minimizing the Gibbs free energy per nucleon (Eq. (2.18)) for various magnetic field strengths and is shown in table 2.1. When we compare our results of magnetic fields with that of zero field case we find several new and heavier nuclei to appear in the sequence of nuclei. For $B_* = 100$, ^{66}Ni disappear from the sequence as was also found in Ref. [46]. When $B_* = 10^3$, two heavier nuclei, ^{88}Sr and ^{128}Pd are found to appear while the nucleus ^{78}Ni disappears from the sequence. If the magnetic field is increased to $B_* = 2 \times 10^3$ ($\sim 10^{17}$ G), another heavy nucleus ^{132}Sn find its place in the sequence, but ^{80}Zn no longer exists. Finally, for $B_* = 10^4$, ^{56}Fe is found to be replaced by ^{60}Ni and also ^{82}Ge disappears from the sequence. Further we note that the maximum density (ρ_{max}) upto which an equilibrium nucleus can exist, increases as the field strength increases and

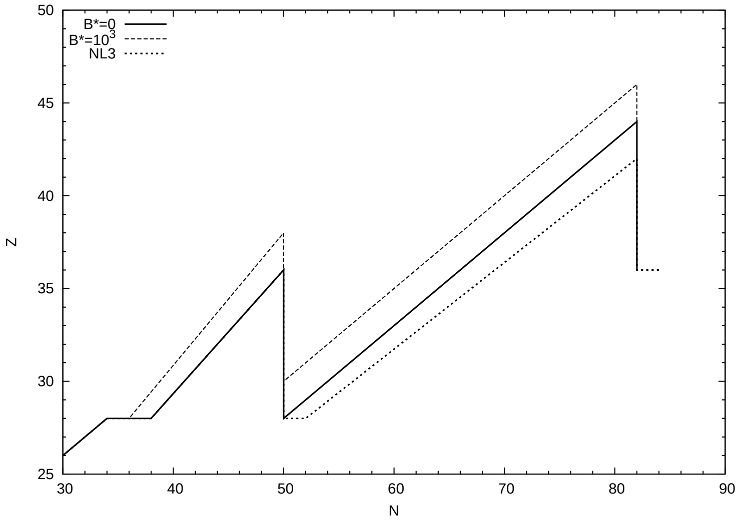

Figure 2.3: Proton number is shown as a function of neutron number for different theoretical nuclear models with and without magnetic fields.

as a result, the neutron drip point gets shifted from 4.34×10^{11} g cm^{-3} in zero field to 4.92×10^{11} g cm^{-3} for $B_* = 10^3$ and to 2.40×10^{12} g cm^{-3} for $B_* = 10^4$. The lattice energy correction influences our results in strong magnetic fields, e.g. ^{180}Xe replaces ^{118}Kr for magnetic field $B_* = 10^4$, if the lattice correction is not included in our calculations. It is worth mentioning here that our results are different from those of earlier calculation [46] because we have adopted most recent experimental and theoretical nuclear mass tables. In Ref. [46] the last experimentally studied nucleus that appear in the sequence was ^{84}Se, but in our case the corresponding nucleus is ^{78}Ni, i.e. more experimental data are in use here. Further we performed our calculation at higher magnetic fields than the previous calculation [46] as it has become relevant after the discovery of magnetars.

Fig. 2.3 displays the proton number as a function of neutron number. Here we compare results obtained with two different theoretical nuclear mass models which are used whenever experimental data are not available. We use the theoretical model of Möller et al. [51] and relativistic mean field model with NL3 set [54,55]. It is evident from the figure that for zero magnetic field our calculation of equilibrium nuclei initially agrees with those of the relativistic model calculation because nuclear masses are obtained from the experimental mass table. However, both calculations for zero magnetic field differ considerably beyond N=50 due to differences in theoretical mass tables used here.

2.5 Summary and Conclusions

We have revisited the BPS model of the outer crust to calculate the EOS and the sequence of nuclei in presence of strong magnetic fields and using the recent experimental mass table. Further we have included the correction in the lattice energy due to the finite size of a nucleus. Several new and heavier nuclei are found to appear in the sequence when the magnetic field is very strong. Strong magnetic fields also shift the neutron drip point to higher densities as compared to the field free case. Our results can greatly affect the transport properties such as thermal and electrical conductivities as well as shear viscosity of the crust in magnetars. It can also play very important role in the calculation of crustal shear modes as will be discussed in Chapter 4.

Chapter 3

The Inner Crust

3.1 Introduction

In the outer crust of a neutron star, neutrons and protons are bound inside nuclei and immersed in a uniform background of relativistic electron gas. As the density increases, nuclei become more and more neutron rich until the neutron drip point is reached when neutrons begin to drip out of nuclei. This is the beginning of the inner crust. The matter in the inner crust is made up of nuclei embedded in a neutron gas along with the uniform background of an electron gas. Further the matter is in β-equilibrium and maintains charge neutrality. Nuclei are also in mechanical equilibrium with the neutron gas. The ground state properties of the inner crusts of neutron stars in zero magnetic field were studied by different groups. The early studies of the inner crust matter were based on the extrapolations of the semiempirical mass formula to the free neutron gas regime [56, 57]. Baym, Bethe and Pethick considered the reduction of the nuclear surface energy due to the free neutron gas in their calculation [52]. The study of nuclei in the neutron star crust was carried out using the energy density of a many body system by Negele and Vautherin [58]. With increasing density in the inner crust, unusual nuclear shapes might appear there [3–5]. The properties of nuclei in the inner crust were also investigated using a relativistic field theoretical model [59]. The transport properties such as thermal and electrical conductivities of neutron star crusts in magnetic fields were studied by several groups [60, 61]. Recently the magnetized neutron star crust was studied using the Thomas-Fermi model and Baym-Bethe-Pethick [52] and Harrison-Wheeler EOS for nuclear matter [62].

There are two important aspects of the problem when nuclei are immersed in a neutron gas. On the one hand we have to deal with the coexistence of two phases of nuclear matter - denser phase inside a nucleus and low density phase outside it, in a thermodynamical consistent manner. On the other hand, the determination of the surface energy of the interface between two phases with good accuracy is needed. It was shown that this problem could be solved using the subtraction procedure of Bonche, Levit and Vautherin [63, 64]. The properties of a nucleus are isolated from the nucleus plus neutron gas in a temperature dependent Hartree-Fock theory using the subtraction procedure. This same method was extended to isolated nuclei embedded in a neutron gas [65] as well as nuclei in the inner crust at zero temperature [66]. This motivates us to study the properties of nuclei in the inner crust in the presence of strongly quantizing magnetic fields relevant to magnetars using the subtraction procedure.

Recently the stability of nuclei embedded in an electron gas was investigated within a relativistic mean field model in zero magnetic field [67]. It was observed in their calculation that nuclei became more stable against α decay and spontaneous fission with increasing electron number density. We have already observed in the previous chapter that the electron number density increases in the presence of strong magnetic fields due to Landau quantization compared with the zero field case. Now, the question is what the impact of Landau quantization would be on the ground state properties of matter in the inner crusts of magnetars. This is the focus of our calculation in this chapter.

This chapter is organized as follows. In Sec. 3.2 , the formalism for the calculation of nuclei in the inner crust immersed in a neutron as well as an electron gas in the presence of strongly quantizing magnetic fields is described. The results of our calculation are discussed in Sec. 3.3. Section 3.4 contains the summary and conclusions.

3.2 Formalism

We investigate the properties of nuclei in the inner crust in the presence of strong magnetic fields using the Thomas-Fermi (TF) model [68]. In this case nuclei are immersed in a neutron gas as well as a uniform background of electrons and may be arranged in a lattice. Like in the outer crust here also each lattice volume is replaced by a spherical cell with a nucleus at its center in the Wigner-Seitz (WS) approximation. Each cell is taken to be charge neutral such that the number of electrons is equal to the number of protons in it. The Coulomb interaction between cells is neglected. Electrons are assumed to be uniformly distributed within a cell. The system maintains the β-equilibrium. We assume that the system is placed in a uniform magnetic field. Electrons are affected by strongly quantizing magnetic fields. Protons in the cell are affected by magnetic fields only through the charge neutrality condition. The interaction of nuclear magnetic moment with the field is negligible in a magnetic field $\sim 10^{17}$ G [49].

The calculation below is performed in a zero temperature TF model. In the WS cell, a nucleus is located at the center and immersed in a low density neutron gas whereas protons are trapped in the nucleus. However, the spherical cell does not define a nucleus. The nucleus is realized after subtraction of the gas part from the cell as shown by Bonche, Levit and Vautherin [63]. In an earlier calculation, it was demonstrated that the TF formalism at finite temperature gave two solutions [64]. One solution corresponds to the nucleus plus neutron gas and the second one represents only the neutron gas. The density profiles of the nucleus plus neutron gas as well as that of the neutron gas are obtained self-consistently in the TF formalism. Finally the nucleus is obtained as the difference of two solutions. This formalism is adopted in our calculation at zero temperature as described below [68].

The nucleus plus gas solution coincides with the gas solution at large distance leading to the definition of the thermodynamic potential (Ω_N) of the nucleus as [63]

$$\Omega_N = \Omega_{NG} - \Omega_G \,, \tag{3.1}$$

where Ω_{NG} is the thermodynamic potential of the nucleus plus gas phase and Ω_G is that of the gas only. The thermodynamic potential is defined as

$$\Omega = \mathcal{F} - \sum_{q=n,p} \mu_q A_q \,, \tag{3.2}$$

where μ_q and A_q are the chemical potential and number of q-th species, respectively. The free energy is given by

$$\mathcal{F}(n_b, Y_p) = \int [\mathcal{H} + \varepsilon_c + \varepsilon_e] d\mathbf{r} \,, \tag{3.3}$$

where $\mathcal{H}$ is nuclear energy density functional, ε_c is the Coulomb energy density and ε_e is the energy density of electrons. The free energy is a function of average baryon density (n_b) and proton fraction (Y_p). The nuclear energy density is calculated using the SkM nucleon-nucleon interaction and given by [69, 70]

$$\begin{aligned}
\mathcal{H}(r) \;=\;& \frac{\hbar^2}{2m_n^*}\tau_n + \frac{\hbar^2}{2m_p^*}\tau_p + \frac{1}{2}t_0 \left[\left(1 + \frac{x_0}{2}\right) n^2 - \left(x_0 + \frac{1}{2}\right)\left(n_n^2 + n_p^2\right) \right] \\
& - \frac{1}{16}\left[t_2 \left(1 + \frac{x_2}{2}\right) - 3t_1 \left(1 + \frac{x_1}{2}\right) \right] (\nabla n)^2 \\
& - \frac{1}{16}\left[3t_1 \left(x_1 + \frac{1}{2}\right) + t_2 \left(x_2 + \frac{1}{2}\right) \right] \left[(\nabla n_n)^2 + (\nabla n_p)^2 \right] \\
& + \frac{1}{12} t_3 n^\alpha \left[\left(1 + \frac{x_3}{2}\right) n^2 - \left(x_3 + \frac{1}{2}\right)\left(n_n^2 + n_p^2\right) \right] \,.
\end{aligned} \tag{3.4}$$

The first two terms of the nuclear energy density are the kinetic energy densities of neutrons and protons, respectively. The third term originates from the zero-range part of the Skyrme interaction whereas the fourth and fifth terms are relevant for surfaces effects. The last term is the contribution of the density dependent part of the nucleon-nucleon interaction. The effective mass of nucleons is given by

$$\begin{aligned} \frac{m}{m_q^*(r)} &= 1 + \frac{m}{2\hbar^2}\left\{\left[t_1\left(1+\frac{x_1}{2}\right)+t_2\left(1+\frac{x_2}{2}\right)\right]n\right. \\ &\left. + \left[t_2\left(x_2+\frac{1}{2}\right)-t_1\left(x_1+\frac{1}{2}\right)\right]n_q\right\} , \end{aligned} \tag{3.5}$$

where the total baryon density is $n = n_n + n_p$.

The Coulomb energy densities for the NG and G phases are:

$$\begin{aligned} \varepsilon_c^{NG}(r) &= \frac{1}{2}(n_{NG}^p(r)-n_e)\int\frac{e^2}{\mid \mathbf{r}-\mathbf{r'}\mid}(n_{NG}^p(r')-n_e)d\mathbf{r'} , \\ \varepsilon_c^{G}(r) &= \frac{1}{2}(n_{G}^p(r)-n_e)\int\frac{e^2}{\mid \mathbf{r}-\mathbf{r'}\mid}(n_{G}^p(r')-n_e)d\mathbf{r'} \\ &+ n_N^p(r)\int\frac{e^2}{\mid \mathbf{r}-\mathbf{r'}\mid}(n_{G}^p(r')-n_e)d\mathbf{r'} , \end{aligned} \tag{3.6}$$

where n_{NG}^p and n_G^p are proton densities in the nucleus plus gas phase and in the gas phase, respectively. Here, the coulomb energy densities (ε_c) represent the direct part. We do not consider the exchange part because its contribution is small.

Thus far, the formalism described above is applicable for the zero magnetic field. However, we study the effects of magnetic fields on ground state properties of the inner crust. In the presence of a magnetic field, the motion of electrons get quantized in the plane perpendicular to the field and as a result electron number density gets modified as already discussed in the previous chapter. The Coulomb energy density and the energy density of electrons appearing in Eq. (3.3) are also get influenced by the presence of magnetic fields. Protons in nuclei get affected by a magnetic field through the charge neutrality condition. We use Eq. (2.7) for energy density of electrons for magnetic cases and for nonmagnetic case we use Eq. (2.14).

We minimize the thermodynamic potential in the TF approximation with the condition of number conservation of each species. The density profiles of neutrons and protons with or without magnetic fields are obtained from

$$
\begin{aligned}
\frac{\delta\Omega_{NG}}{\delta n^q_{NG}} &= 0 \\
\frac{\delta\Omega_G}{\delta n^q_G} &= 0\,.
\end{aligned}
\tag{3.7}
$$

This results in the following coupled equations [65, 66]

$$
\begin{aligned}
(3\pi^2)^{\frac{2}{3}}\frac{\hbar^2}{2m^*_q}(n^q_{NG})^{\frac{2}{3}} + V^q_{NG} + V^c_{NG}(n^p_{NG}, n_e) &= \mu_q\ , \\
(3\pi^2)^{\frac{2}{3}}\frac{\hbar^2}{2m^*_q}(n^q_G)^{\frac{2}{3}} + V^q_G + V^c_G(n_e) &= \mu_q\,,
\end{aligned}
\tag{3.8}
$$

where m^*_q is the effective mass of q-th species , V^q_{NG} and V^q_G are the single particle potentials of nucleons in the nucleus plus gas as well as gas phases [71]. On the other hand, V^c_{NG} and V^c_G are direct parts of the single particle Coulomb potential corresponding to the nucleus plus gas and gas only solutions, respectively, and both are given by

$$
V^c(r) = \int [n^p_{NG}(r') - n_e]\,\frac{e^2}{\mid \mathbf{r} - \mathbf{r'} \mid}d\mathbf{r'}\,. \tag{3.9}
$$

The average chemical potential for q-th nucleon is

$$
\mu_q = \frac{1}{A_q}\int [(3\pi^2)^{\frac{2}{3}}\frac{\hbar^2}{2m^*_q}(n^q_{NG})^{\frac{2}{3}} + V^q_{NG}(r) + V^c_{NG}(r)]n^q_{NG}(r)d\mathbf{r}\,, \tag{3.10}
$$

where A_q refers to N_{cell} or Z_{cell} of the cell which is defined by the average baryon density n_b and proton fraction Y_p. The β-equilibrium condition is written as

$$
\mu_n = \mu_p + \mu_e\ . \tag{3.11}
$$

The average electron chemical potential in magnetic fields is given by (see Sec 2.2)

$$\mu_e = \left[p_{f_e}(\nu)^2 + (m_e^2 + 2\nu eB)\right]^{1/2} - < V^c(r) > , \tag{3.12}$$

where $< V^c(r) >$ denotes the average of the single particle Coulomb potential.

Density profiles of neutrons and protons in the cell are constrained as

$$\begin{aligned} Z_{\text{cell}} &= \int n_p^{NG}(r) d\mathbf{r} \, , \\ N_{\text{cell}} &= \int n_n^{NG}(r) d\mathbf{r} \, , \end{aligned} \tag{3.13}$$

where N_{cell} and Z_{cell} are neutron and proton numbers in the cell, respectively.

Finally, number of neutrons (N) and protons (Z) in a nucleus with mass number $A = N + Z$ are obtained using the subtraction procedure as

$$\begin{aligned} Z &= \int \left[n_p^{NG}(r) - n_p^{G}(r)\right] d\mathbf{r} \, , \\ N &= \int \left[n_n^{NG}(r) - n_n^{G}(r)\right] d\mathbf{r} \, . \end{aligned} \tag{3.14}$$

3.3 Results and Discussion

We present the results of our calculation with the SkM interaction in the following paragraphs. We find the equilibrium nucleus at each density point minimizing the free energy of the system within a WS cell maintaining charge neutrality and β-equilibrium. The variables of this problem are the average baryon density (n_b), the proton fraction (Y_p) and the radius of a cell (R_c). For fixed values of n_b, Y_p and R_c, the total number of nucleons (A_{cell}) is given by $A_{\text{cell}} = V_{\text{cell}} n_b$ where the volume of a cell is $V_{\text{cell}} = 4/3\pi R_C^3$. The proton number in the cell is $Z_{\text{cell}} = Y_p n_b V_{cell}$ and the neutron number is $N_{\text{cell}} = A_{\text{cell}} - Z_{\text{cell}}$. We obtain density profiles of neutrons and protons in the cell using eqs 3.8 and 3.13 at a

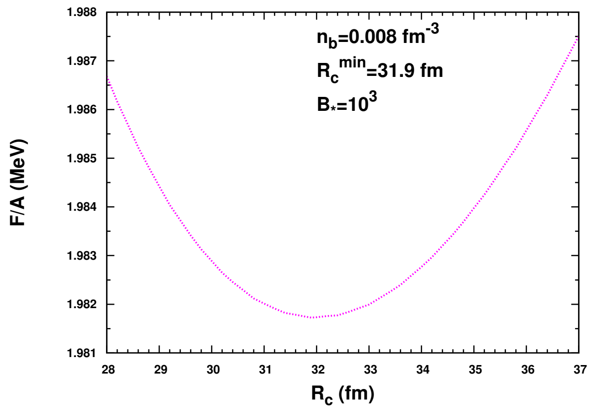

Figure 3.1: Free energy per nucleon as function of cell size for the SkM interaction and average baryon density 0.008 fm^{-3} and magnetic field $B_* = 10^3$.

given average baryon density and proton fraction. Consequently, we calculate chemical potentials of neutrons and protons and free energy per nucleon. Next, we vary the proton fraction, calculate chemical potentials and density profiles, and obtain the β-equilibrium in the cell. Finally, we adjust the cell size (R_C) and repeat the above mentioned steps to get the minimum of the free energy. These values of Y_p and R_C are then used to calculate neutron and proton numbers in a nucleus at an average baryon density corresponding to the free energy minimum with the help of eq 3.14. This procedure is repeated for each average baryon density.

The minimum of the free energy originates from the interplay between different contributions. The free energy per nucleon is given by

$$F/A = e_N + e_{lat} + e_{ele}. \tag{3.15}$$

The nuclear energy including the Coulomb interaction among protons is denoted by e_N, e_{lat} is the lattice energy which involves the Coulomb interaction between electrons and protons and the electron kinetic energy is e_{ele}. The free energy per nucleon in the presence of magnetic field $B_* = 10^3$ ($B_* = B/4.414 \times 10^{13}$ G) is shown in Fig. 3.1 as a function

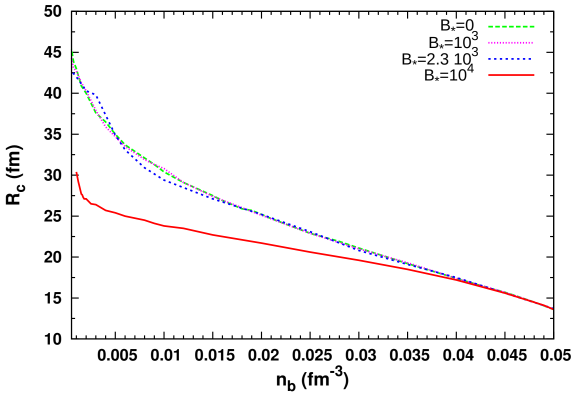

Figure 3.2: Cell size as a function of average baryon density for the SkM interaction and different magnetic fields.

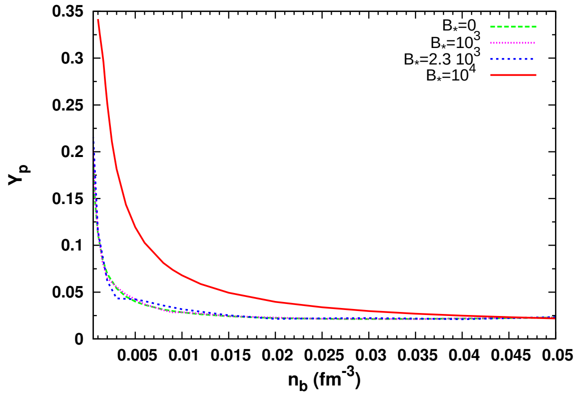

Figure 3.3: Proton fraction as a function of average baryon density for the SkM interaction and different magnetic fields.

of the cell size for an average baryon density $n_b = 0.008$ fm $^{-3}$. We note that the nuclear energy increases with R_C. On the other hand, the lattice energy and electron kinetic energy both decrease with increasing cell size. The competition of e_N with the sum of e_{lat} and e_{ele} determines the free energy minimum. The cell radius corresponding to the free energy minimum is 32.1 fm for the zero field case (not shown in the figure) and 31.9 fm for $B_* = 10^3$. The corresponding proton fraction for $B = 10^3$ is 0.03.

In Fig. 3.2, the cell size corresponding to the free energy minimum is plotted as a function of average baryon density for magnetic fields $B_* = 0$, 10^3, 2.3×10^3 and 10^4. For magnetic fields $B < 2.3 \times 10^3$ ($\simeq 10^{17}$ G), several Landau levels are populated by electrons. Consequently we do not find any change in the cell size in the magnetic fields compared with the zero-field case. However, we find some change in the cell size for $B_* = 2.3 \times 10^{17}$ when only the zeroth Landau level is populated by electrons for $n_b \leq 0.004$, fm^{-3} whereas first two levels are populated in the density range 0.005 to 0.015 fm^{-3}. However the cell size is increased compared with the zero-field case due to the population of only zeroth Landau level in the presence of a magnetic field $B_* = 10^4$ G. The size of the cell always decreases with increasing average baryon density.

The proton fraction in the presence of magnetic fields is shown as a function of average

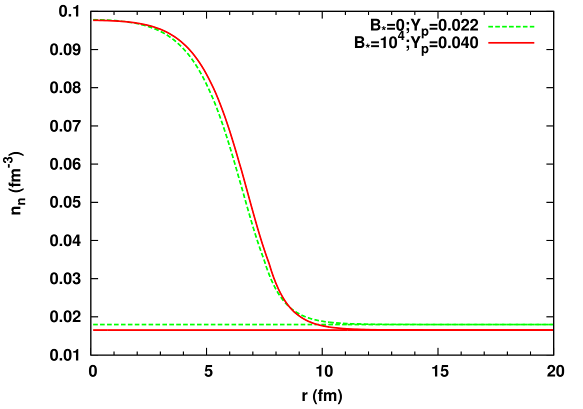

Figure 3.4: Neutron density profiles in the nucleus plus gas phase and gas phase for the SkM interaction and for magnetic fields $B_* = 0$ and $B_* = 10^4$ at $n_b = 0.02$ fm^{-3}.

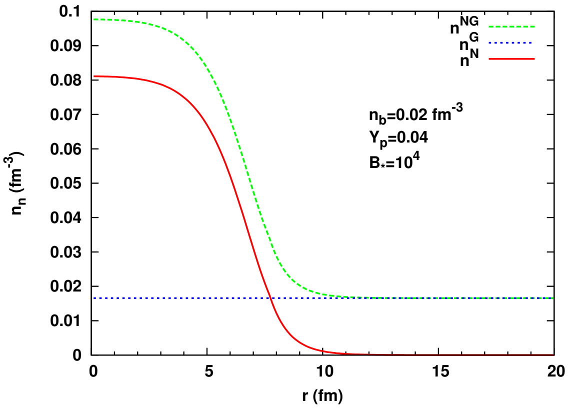

Figure 3.5: Neutron density profiles in the nucleus plus gas phase and after the subtraction of the gas phase for the SkM interaction and for $B_* = 10^4$ at $n_b = 0.02$ fm^{-3}.

baryon density in Fig. 3.3. Protons in nuclei are affected by the Landau quantization of electrons through the charge neutrality condition in a cell. For magnetic fields $B_* < 2.3{\times}10^3$, the proton fraction is the same as that of the zero-field case over the whole density range considered here. We find some changes in the proton fraction below $n_b = 0.015$ fm^{-3} when $B_* = 2.3 \times 10^3$. Though electrons populate the zeroth Landau level for $n_b \leq 0.004$ fm^{-3}, the proton fraction decreases below the corresponding proton fraction of the zero-field case. However, for a magnetic field $B_* = 10^4$, the proton fraction is strongly enhanced compared with the zero-field case due to the population of only the zeroth Landau level for $n_b \leq 0.04$ fm^{-3}.

The density profiles of neutrons in the nucleus plus gas and gas phases corresponding to $n_b = 0.02$ fm^{-3} with and without magnetic fields are exhibited as a function of distance (r) within the cell in Fig. 3.4. The green line denotes the zero-field case, whereas the red line represents the density profile with the field $B_* = 10^4$. The horizontal lines imply the uniform gas phases in both cases. The proton fraction is 0.040 for the magnetic field case whereas it is 0.022 for the zero-field case. Further, we show the subtracted density profiles of neutrons with a magnetic field $B_* = 10^4$ in Fig. 3.5. Though neutrons are not directly affected by the magnetic field, the neutron chemical potential is modified

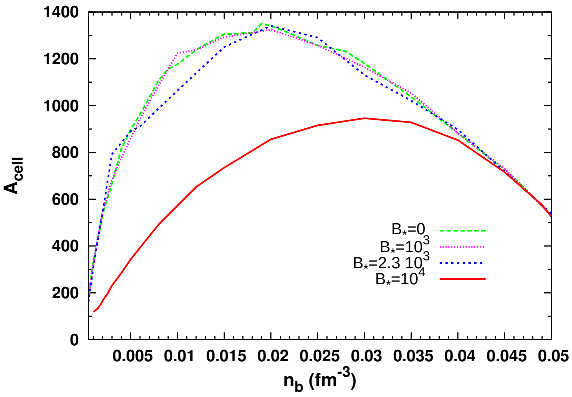

Figure 3.6: Total number of nucleons in a cell $A_{\rm cell}$ as a function of average baryon density for the SkM interaction and different magnetic fields.

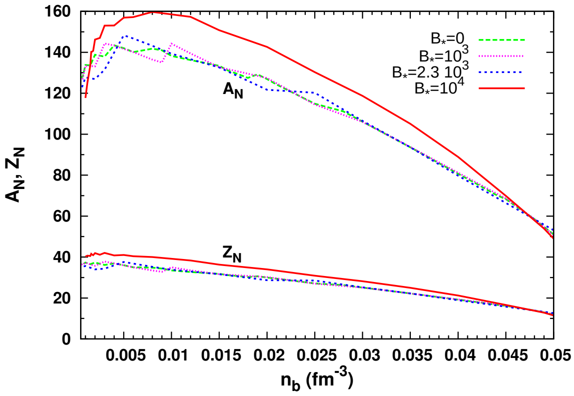

Figure 3.7: Mass and proton numbers of equilibrium nuclei as a function of average baryon density for the SkM interaction and different magnetic strengths.

through the β-equilibrium due to Landau quantization of electrons. As a consequence, we find that the neutron density is higher in the gas phase for the zero-field case than that of the magnetic field. This implies that fewer neutrons drip out of a nucleus in the presence of strong magnetic fields. This can be attributed to the shift in the β-equilibrium in strong magnetic fields. We encounter a similar situation in the calculation of the outer crust in magnetic fields (see Chapter 2), i.e, the neutron drip point is shifted to higher densities [53].

Now we know the density profiles of neutrons and protons in the nucleus plus gas phase as well as in the nucleus at each average baryon density. We immediately calculate the total number of neutrons and protons in the nucleus plus gas phase and in a nucleus using Eqs. (3.13) and (3.14). We show total number of nucleons ($A_{\rm cell}$) in a cell for magnetic fields $B_* = 0$, 10^3, 2.3×10^3 and 10^4 with average baryon density in Fig. 3.6. In all cases, the $A_{\rm cell}$ growing with the density reaches a maximum and then decreases. Such a trend was observed in the calculation of Negele and Vautherin [58] in the absence of a magnetic field. We note that our predictions for $B_* = 10^3$ do not change from the field-free results because a large number of Landau levels are populated in that magnetic field. For a magnetic field $B_* = 2.3 \times 10^3$ ($B \simeq 10^{17}$ G), the total number of nucleons decreases compared to the corresponding results of the field- free case in the density regime 0.005 - 0.02 fm^{-3}. This can be understood from the behavior of the cell size around that density regime in Fig. 3.2. For $B_* = 10^4$, only the zeroth Landau level is populated by electrons for densities $\leq$ 0.04 fm^{-3}. This modifies the β-equilibrium and the charge neutrality conditions which, in turn, impact the size of the cell and the total number of nucleons in a cell. This effect is pronounced in the case of $B_* = 10^4$. In this case, A_{cell} is significantly reduced compared with the zero-field case for densities $\leq$ 0.04 fm^{-3}.

We obtain neutron (N), proton (Z) and total nucleon numbers (A) in the nucleus at each average baryon density following the subtraction procedure. Total nucleon and proton numbers are shown in Fig. 3.7 for the above mentioned magnetic fields. When the magnetic field is 2.3×10^3, it is noted that our results start oscillating from the field-free results. This may be attributed to the fact that the population of Landau levels jumps from zero to a few levels in the above mentioned fields as baryon density varies from lower to higher values. In contrast to Fig. 3.6, we find that total nucleon and proton numbers inside the nucleus at each density point beyond 0.002 upto 0.04 fm^{-3} are significantly enhanced in the case of $B_* = 10^4$ compared to the field-free case as well as other magnetic fields considered here. This clearly demonstrates that more neutrons are inside the nucleus in the presence of strong magnetic fields $\geq 2.3 \times 10^3$ ($\simeq 10^{17}$ G) than in the gas phase in that density regime. This is opposite to the situation in the zero magnetic field. This can be easily understood from the density profiles with and without magnetic fields in Fig. 3.4 and Fig. 3.5.

We repeat the above-mentioned calculation for the SLy4 nucleon-nucleon interaction [72]. Fig. 3.8 shows the variation of nucleon-nucleon interaction on mass and proton numbers of nuclei as a function of average baryon density with $B_* = 0$ and $B_* = 10^4$. Comparing results of the SkM and SLy4 interactions, we find that A_N and Z_N in the latter case are higher beyond density of 0.005 fm^{-3}. We find that symmetry energy of the SLy4 interaction is larger in the subsaturation density regime that that of the SkM

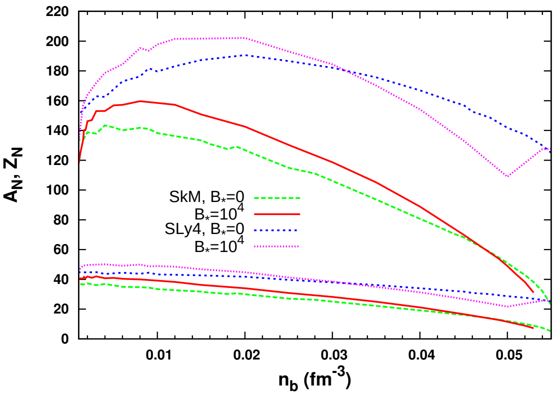

Figure 3.8: Mass and proton numbers of equilibrium nuclei as a function of average baryon density for the SkM and SLy4 interactions and magnetic fields $B_* = 0$ and $B_* = 10^4$.

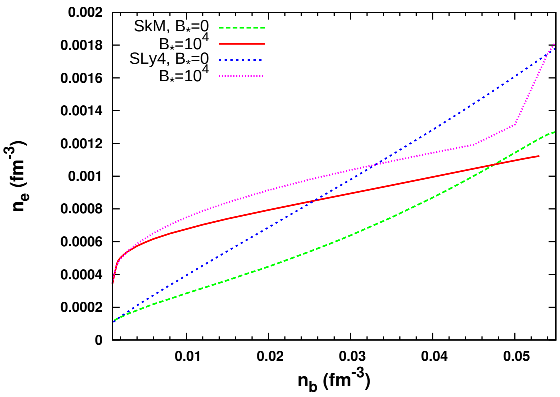

Figure 3.9: Electron number density as a function of average baryon density for the SkM and SLy4 interactions and magnetic fields $B_* = 0$ and $B_* = 10^4$.

interaction. Higher symmetry energy results in a higher proton fraction, which, in turn, enhances the electron density via the charge neutrality condition. This is demonstrated in Fig. 3.9, where the electron density is plotted as a function of average baryon density for SkM and SLy4 interactions with and without a magnetic field. Consequently, this leads to an increase in the number of nucleons in a nucleus for the SLy4 interaction. The values of A_N and Z_N for the SLy4 case in the presence of a magnetic field are enhanced compared to the field-free case as found with the SkM interaction up to a baryon density of ~ 0.03 fm^{-3}. It is noted for the SLy4 interaction that the values of A_N and Z_N in the magnetic field jump when electrons move from the zeroth to the first Landau level at a baryon density of 0.05 fm^{-3}. We do not find such a feature for the SkM interaction case because we have already noted that only the zeroth Landau level is populated in $B_* = 10^4$ up to the density regime shown in Fig. 3.8.

We do not consider the nuclear shell effects in our calculations. Here we adopt the TF formalism which reproduces average nuclear properties very well. A detailed comparison of properties of nuclei in Hartree-Fock as well as (extended) calculations using the subtraction procedure and the same nucleon-nucleon interaction was performed by Suraud [64]. It was noted that the results of semi-classical calculations, in particular the

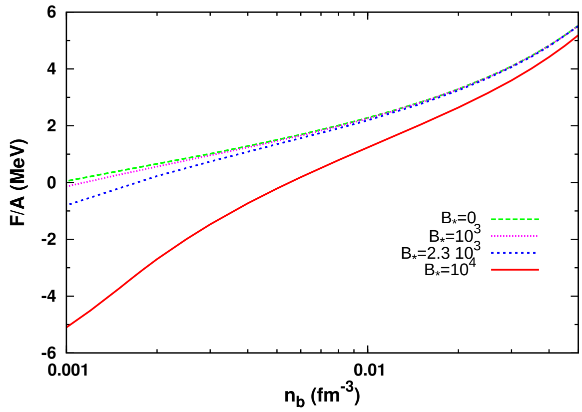

Figure 3.10: Minimum free energy per nucleon as function of average baryon density for the SkM interaction and various magnetic fields.

TF calculation [64], were in very good agreement with those of the Hartree-Fock calculation [63]. On the other hand, the washout of neutron shells may happen due to the presence of of external neutrons in which nuclei are immersed [73, 74]. In this case, the collisional broadening of a nuclear level due to scattering of external neutrons could make it wider that the gap between levels.

We plot the free energy per nucleon of the system with average baryon density in Fig. 3.10. This calculation is performed using the SkM interaction. Our results for $B_* = 10^3$ do not change much form the field-free results. However, for $B_* = 2.3 \times 10^3$ ($B \simeq 10^{17}$ G), the free energy per nucleon is reduced at lower densities (< 0.004 fm^{-3}) compared to the field-free case. We find more pronounced reduction in the free energy per nucleon in the field $B_* = 10^4$ almost over the whole density regime considered here.

3.4 Summary and Conclusions

We have investigated ground-state properties of the inner crust in the presence of strong magnetic fields of $\sim 10^{16}$ or more. Nuclei are immersed in a neutron gas and uniform background of electrons. We have adopted the SkM and SLy4 interactions for the nuclear energy density and studied this problem in the TF model. Electrons are affected through Landau quantization in strong magnetic fields because much lower Landau levels can be occupied in these cases. Consequently, electron number density and energy density are modified in strongly quantizing magnetic fields and the β-equilibrium condition is altered compared with the field-free case. The enhancement of the electron number density in magnetic fields $\geq 10^{17}$ G due to the population of only the zeroth Landau level leads to enhancement in proton fraction through the charge neutrality condition. We minimize the free energy of the system within a WS cell to obtain the nucleus at each average baryon density. In this connection, we used the subtraction procedure to obtain the density profiles of a nucleus from the nucleus plus gas and gas solutions at each average baryon density point. We note that fewer neutrons drip out of a nucleus in the presence of strong fields than the situation without a magnetic field. This results in larger mass and proton numbers in a nucleus in the presence of magnetic field $> 10^{17}$ G compared to the corresponding nucleus in the field-free case. Further the free energy per nucleon of the system is reduced in magnetic fields $\geq 10^{17}$ G. It is found that the variation of nucleon-nucleon interaction influences mass and proton numbers of nuclei in zero as well as strong magnetic fields.

This calculations might have observational consequences for magnetars in several ways. Results of this chapter together with results of the outer crust (Chapter 2, [53]) can be very important to explain the observed QPO frequencies of magnetars as will be discussed in the chapter 4. Magnetars might eject crustal matter due to tremendous magnetic stress on the crust [75]. The ejected matter of the inner crust might expand to much lower densities. The decompressed crustal matter has long been considered as an important site for r-process nuclei [73,76]. It would be worth studying the r-process in the decompressed crust matter of magnetars using the results of our calculation as input.

Chapter 4

Shear mode oscillations in magnetars

4.1 Introduction

Soft gamma ray repeaters (SGRs) are characterized by their sporadic and short bursts of soft gamma rays. Luminosities in these bursts could reach as high as $\sim 10^{41}$ erg s^{-1}. There are about 11 SGRs (see table 1.1) known observationally. Evidences of stronger emissions of gamma rays from SGRs were observed in several cases. These events are known as giant flares in which luminosities are $\sim 10^{44} - 10^{46}$ erg s^{-1} . So far three cases of giant flares were reported and those are for SGR 0526-66, SGR 1900+14 and SGR 1806-20 [77–80]. In giant flares, the early part of the spectrum was dominated by hard flash of shorter duration followed by a softer decaying tail of a few hundreds of seconds.

SGRs are very good candidates for magnetars which are neutron stars with very high surface magnetic fields $\sim 10^{15}$ G [38, 81] (table 1.1). Giant flares might be caused by the evolving magnetic field and its stress on the crust of magnetars. It was argued that starquakes associated with giant flares could excite global seismic oscillations [81]. Torsional shear modes of magnetars with lower excitation energies would be easily excited. In this case, oscillations are restored by the Coulomb forces of crustal ions. Furthermore, the shear modes have longer damping times. Quasi-periodic oscillations (QPOs) were found in the decaying tail of giant flares from the timing analysis of data [78–80]. These findings implied that QPOs might be shear mode oscillations of magnetar crusts [81]. Frequencies of the observed QPOs ranged from 18 Hz to 1800 Hz.

It was noted from earlier theoretical models of QPOs that the observed frequencies in particular higher frequencies could be explained reasonably well using torsional shear oscillations of magnetar crusts [79,81–85]. On the other hand, lower frequencies of observed QPOs might be connected to Alfv́en modes of the fluid core. This makes the study of the oscillations of magnetar crusts more difficult. There were attempts to explain frequencies of QPOs using Alfv́en oscillations of the fluid core without considering a crust [86–88]. The coupling of Alfv́en oscillations of the fluid core with the shear mode oscillations in the solid crust due to strong magnetic fields in magnetars was already studied by several groups [89–92]. It was argued that torsional shear modes of the crust might appear in GSOs and explain observed frequencies of QPOs for not very strong magnetic fields despite all these complex problem [93].

Nuclear physics of crusts plays an important role on the torsional shear modes of magnetar crusts. In particular, the effects of the nuclear symmetry energy on the shear mode frequencies were investigated recently [85]. It may be worth noting here that torsional shear mode frequencies are sensitive to the shear modulus of neutron star crusts. Furthermore, the shear modulus is strongly sensitive to the composition of neutron star crusts. Earlier studies of torsional shear mode oscillations exploited only non-magnetic crusts. We have seen in chapters 2 and 3 that strong magnetic fields have significant effects on the ground state properties of neutron star crusts. This, in turn, might influence the shear modulus of crusts and shear mode oscillations in magnetars. This motivates us to study torsional shear mode oscillations of magnetars using magnetic crusts [94].

We organize this chapter in the following way. We describe models for torsional shear mode oscillations of magnetars in Sec. 4.2. Results of this calculation are discussed in Sec. 4.3. Section 4.4 gives the summary and conclusions.

4.2 Formalism

Earlier calculations of torsional shear mode oscillations were performed in Newtonian gravity [81, 82, 95, 96] as well as in general relativity [84, 86, 93, 97, 98] with and without magnetic fields. In many of these calculations, the magnetized crust was decoupled from the fluid core.

As we are interested in the effects of magnetized crusts on torsional shear mode frequencies, we consider a free slip between the crust and the core. Here we calculate torsional shear mode frequencies for spherical and non-rotating stars in presence of a dipole magnetic field following the model of Refs. [84, 98]. We neglect any deformation in the shape of the equilibrium star due to magnetic fields considered here as the magnetic energy is much smaller compared to the gravitational energy [84].

4.2.1 Magnetic field distribution

The equilibrium model for a non-rotating spherically symmetric neutron star can be obtained by solving the Tolman-Oppenheimer-Volkov (TOV) equation with a line element of the form

$$ds^2 = -e^{2\nu(r)}dt^2 + e^{2\lambda(r)}dr^2 + r^2(d\theta^2 + \sin^2\theta d\phi^2)\,. \tag{4.1}$$

The magnetic field distribution is obtained from the Maxwell equations

$$F^{\alpha\beta}_{\ \ ;\beta} = 4\pi J^\alpha\,. \tag{4.2}$$

For a dipole magnetic field and within ideal MHD approximation, Maxwell equations (4.2) lead to the following equation [84]

$$e^{-2\lambda}\frac{d^2a}{dr^2} + (\nu' - \lambda')e^{-2\lambda}\frac{da}{dr} - \frac{2a}{r^2} = -4\pi j\,, \tag{4.3}$$

where prime denotes the derivative with respect to r; $a(r)$ and $j(r)$ give the radial dependence of the non-vanishing component of the electromagnetic 4-potential $A_\alpha = (0,0,0,A_\phi)$ and the 4-current $J_\alpha = (0,0,0,J_\phi)$, respectively. Outside the star, this equation can be solved analytically putting $j \equiv j_{\rm out} = 0$ [84, 99] :

$$a_{\rm out} = -\frac{3\mu_d}{8M^3} r^2 \left[\ln\left(1 - \frac{2M}{r}\right) + \frac{2M}{r} + \frac{2M^2}{r^2} \right] , \tag{4.4}$$

where μ_d is the magnetic dipole moment observed at infinity. Inside the star the Eq. 4.3 is solved numerically with a current distribution of the form [100]

$$j_{\rm in} = c_0 r^2 (\epsilon + P) , \tag{4.5}$$

where c_0 is an arbitrary constant. Finally the magnetic field distribution is given by [84]

$$B_r = \frac{2e^{\lambda}\cos\theta}{r^2}\, a , \tag{4.6}$$

$$B_\theta = -e^{-\lambda}\sin\theta\,\frac{da}{dr} . \tag{4.7}$$

4.2.2 Torsional shear modes

The equations of motion for the magnetized fluid is given by [84]

$$\left(\epsilon + P + \frac{B^2}{4\pi}\right) u^\alpha u_{;\beta} u^\beta = -\, \triangle^{\alpha\beta} \left(P + \frac{B^2}{8\pi}\right)_{;\beta} + \frac{1}{4\pi}\, \triangle^{\alpha}_{\ \delta}\, (B^\delta B^\beta)_{;\beta} , \tag{4.8}$$

where $u^\alpha = (e^{-\nu}, 0, 0, 0)$ is the 4-velocity which satisfies $u^\alpha u_\alpha = -1$ and $\triangle^{\alpha\beta}$ is a projection tensor that annihilates the component of a 4-vector parallel to u^α. This equation is obtained from the conservation of the energy-momentum tensor as following

$$\triangle^{\alpha}_{\ \delta}\, T^{\delta\beta}_{\ \ ;\beta} = 0 , \tag{4.9}$$

where $T^{\alpha\beta}$ is the energy-momentum tensor of the magnetized fluid given by

$$
\begin{aligned}
T^{\alpha\beta} &= T_0^{\alpha\beta} + T_M^{\alpha\beta} \\
&= \left[(\epsilon + P)u^\alpha u^\beta + P g^{\alpha\beta}\right] + \frac{1}{4\pi}\left[\frac{1}{2}B^2 g^{\alpha\beta} + B^2 u^\alpha u^\beta - B^\alpha B^\beta\right] . \qquad (4.10)
\end{aligned}
$$

Here $T_0^{\alpha\beta}$ denotes the energy-momentum tensor of a perfect fluid and $T_M^{\alpha\beta}$ is the contribution of the magnetic field. In the ideal MHD approximation the Maxwell's equations $F_{[\alpha\beta;\gamma]}$ gives [84]

$$
\left(u^\alpha B^\beta - u^\beta B^\alpha\right)_{;\alpha} = 0 \, . \qquad (4.11)
$$

This equation can be recast to get the magnetic induction equation given by [84]

$$
B^\alpha_{;\beta} u^\beta = \left(\sigma^\alpha_\beta + \omega^\alpha_\beta - \frac{2}{3}\delta^\alpha_\beta \Theta\right) B^\beta + B^\delta u_{\delta;\gamma} u^\gamma u^\alpha \, , \qquad (4.12)
$$

where $\Theta = u^\alpha_{;\alpha}$ denotes the expansion of the fluid, $\sigma^\alpha_\beta = (u^\alpha_{;\delta} \triangle^\delta_\beta + u_{\beta;\delta} \triangle^{\delta\alpha} - \frac{2}{3}\Theta \triangle^\alpha_\beta)/2$ is the shear tensor and $\omega^\alpha_\beta = (u^\alpha_\delta \triangle^\delta_\beta - u_{\beta;\delta} \triangle^{\delta\alpha})/2$ is the twist tensor.

To study the torsional shear mode oscillations we need to derive a perturbation equation in terms of axial deformations. This is done by linearizing the equation of motion 4.8 and the magnetic induction equation 4.12, within the relativistic Cowling approximation i.e. by neglecting metric perturbations ($\delta g_{\alpha\beta} = 0$). This approximation is justified by the fact that torsional oscillations being of axial in nature do not induce any density perturbation in the star. Here the only non-vanishing perturbed quantity is [84]

$$
\delta u^\phi = e^{-\nu} \frac{\partial \mathcal{Y}(t,r)}{\partial t} \frac{1}{\sin\theta} \frac{\partial}{\partial \theta} P_l(cos\theta) \, , \qquad (4.13)
$$

where $\mathcal{Y}(r,t)$ denotes the angular displacement of the matter. This displacement induce deformations in the crystal lattice of neutron star crusts. This contribution is included in the linearized equation of motion through the relation $\delta T_{\alpha\beta} = -2\mu\delta S_{\alpha\beta}$ [97], where $\delta T_{\alpha\beta}$ and $\delta S_{\alpha\beta}$ are the linearized shear stress tensor and shear tensor, respectively and

μ is the isotropic shear modulus. With the assumption that $\mathcal{Y}$ has time dependence as $\mathcal{Y}(r,t) = \mathcal{Y}(r)e^{i\omega t}$, the perturbation equation lead to the eigenvalue equation given by [84]

$$\begin{aligned}
\left[\mu + (1+2q_l)\frac{a^2}{\pi r^4}\right]\mathcal{Y}'' &+ \left[\left(\frac{4}{r} + \nu' - \lambda'\right)\mu + \mu' + (1+2q_l)\frac{a}{\pi r^4}\{(\nu' - \lambda')a + 2a'\}\right]\mathcal{Y}' \\
&+ \left[\left\{\left(\epsilon + P + (1+2q_l)\frac{a^2}{\pi r^4}\right)e^{2\lambda} - \frac{q_l a'^2}{2\pi r^2}\right\}\omega^2 e^{2\nu}\right. \\
&- \left.(l+2)(l-1)\left(\frac{\mu e^{2\lambda}}{r^2} - \frac{q_l a'^2}{2\pi r^4}\right) + (2+5q_l)\frac{a}{2\pi r^4}\{(\nu' - \lambda')a' + a''\}\right]\mathcal{Y} \\
&= 0\,,
\end{aligned} \tag{4.14}$$

where

$$q_l = -\frac{l(l+1)}{(2l-1)(2l+3)}\,, \tag{4.15}$$

With the definitions

$$\mathcal{Y}_1 = \mathcal{Y} r^{1-l}\,, \tag{4.16}$$

$$\mathcal{Y}_2 = \left[\mu + (1+2q_l)\frac{a^2}{\pi r^4}\right] e^{\nu-\lambda}\mathcal{Y}' r^{2-l}\,, \tag{4.17}$$

the second order differential equation 4.14 can be transformed into two first order equations :

$$\mathcal{Y}_1' = -\frac{l-1}{r}\mathcal{Y}_1 + \frac{\pi r^3}{\pi r^4 \mu + (1+2q_l)a^2} e^{-\nu+\lambda}\mathcal{Y}_2 \tag{4.18}$$

$$\begin{aligned}
\mathcal{Y}_2' = &-\frac{l+2}{r}\mathcal{Y}_2 - \left[\left\{\epsilon + P + (1+2q_l)\frac{a^2}{\pi r^4} - \frac{q_l a'^2}{2\pi r^2}e^{-2\lambda}\right\}\omega^2 r e^{2(\lambda-\nu)}\right. \\
&\left. -(l+2)(l-1)\left(\frac{\mu e^{2\lambda}}{r} - \frac{q_l a'^2}{2\pi r^3}\right) + (2+5q_l)\frac{a e^{2\lambda}}{\pi r^3}\left(\frac{a}{r^2} - 2\pi j\right)\right] e^{\nu-\lambda}\mathcal{Y}_1\,,
\end{aligned} \tag{4.19}$$

To solve this set of equations we use the boundary condition that the horizontal traction must be zero at the top ($r = R$) and bottom ($r = R_c$) of the stellar crust. These lead to the conditions

$$\mathcal{Y}_2(r_i) = 0 \qquad r_i = R_c, R\,. \tag{4.20}$$

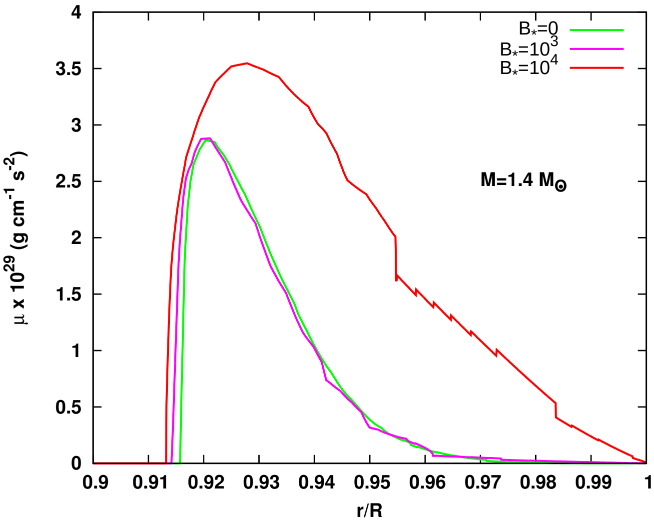

Figure 4.1: Shear modulus as a function of normalized distance for different magnetic field strengths.

We also use the normalization condition

$$\mathcal{Y}_1(R) = 1\,. \tag{4.21}$$

4.3 Results

Our main focus in this chapter is to study the dependence of torsional shear mode frequencies on the compositions of magnetized crusts which are already described in chapters 2 and 3. Earlier calculations were performed with non-magnetized crusts [79, 84, 85, 93]. One important input for the shear mode calculation is the knowledge of shear modulus of the magnetized crust. Here we use the expression of shear modulus as given by [101, 102]

$$\mu = 0.1194\frac{n_i(Ze)^2}{a} \tag{4.22}$$

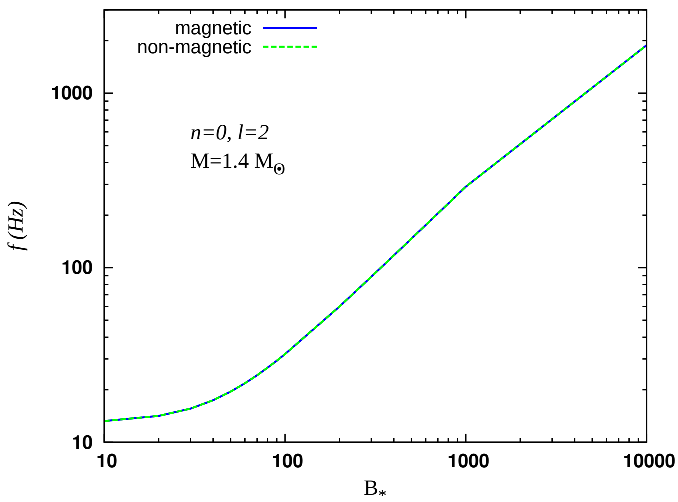

Figure 4.2: Fundamental torsional shear mode frequency with magnetic (solid line) as well as non-magnetic crust (dashed line) as a function of normalized magnetic field ($B_* = B/4.414 \times 10^{13}$ G).

where $a = 3/(4\pi n_i)^{1/3}$, Z is the atomic number of a nucleus and n_i is the ion density. This zero temperature form of the shear modulus was obtained by assuming a bcc lattice and performing directional averages [103]. Later the dependence of the shear modulus on temperature was investigated with Monte Carlo sampling technique by Strohmayer *et al* [102]. However we use the zero temperature shear modulus of Eq. (4.22) in this calculation. Values of n_i and Z are obtained from the calculations of chapters 2 and 3.

To get the torsional shear mode frequencies we have to solve Eqs. (4.18) and (4.19) with boundary conditions (4.20). As can be seen from these equations we need to know the pressure (P), the energy density (ϵ) and the shear modulus (μ) of the stellar matter as a function of distance from the center of the star, to perform this calculation. These information can be obtained by solving the TOV equation with an appropriate neutron star EOS. We prepare the EOS by suitably matching the EOS of the core with that of the crust at crust-core boundary. To get the EOS of the core we use the RMF model with the GM1 parameter set as described in chapter 5. The EOS of the crust is obtained from the calculations of chapters 2 and 3. In Fig. 4.1 the shear modulus of the crust as a function of distance normalized with respect to the stellar radius (R), is shown for different field strengths $B_* = 0, 10^3$ and $B_* = 10^4$ and a neutron star of mass $1.4M_\odot$. The shear modulus increases initially with decreasing distance and drops to zero at the crust-core boundary. For field strengths of $B_* = 10^4$ i.e 4.4×10^{17} or more, the shear modulus is enhanced appreciably as compared with the zero-field case.

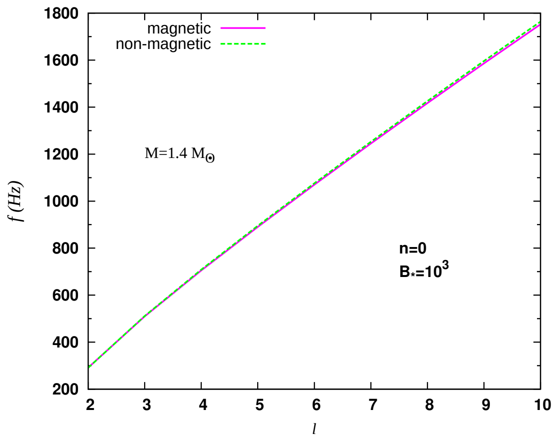

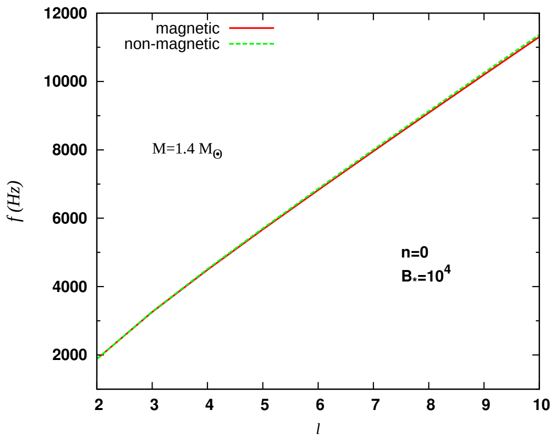

Figure 4.3: Torsional Shear mode frequency for non-magnetic as well as magnetic crusts with fields $B_* = 10^3$ (left panel) and $B_* = 10^4$ for different harmonics of $n = 0$ mode.

It was argued that torsional shear mode frequencies are sensitive to the shear modulus of the crust [79, 81, 85] . Here we calculate the shear mode frequencies using the shear modulus of non-magnetized as well as magnetized crusts. Fundamental torsional shear mode frequencies ($n = 0$, $l = 2$) for a neutron star of mass $1.4M_\odot$ are shown as a function of normalized magnetic field $B_* (\equiv B/4.414 \times 10^{13}\,\mathrm{G})$ in Fig. 4.2. Figure 4.3 shows torsional shear mode frequencies for different harmonics of $n = 0$ mode and magnetic fields $B_* = 10^3$ and 10^4. From these two figures we can see that magnetized crusts have practically no effect on the fundamental as well as different harmonics of $n = 0$ torsional shear mode frequencies. However, there are considerable changes in the frequencies of the first radial overtone ($n = 1$) as can be seen from Fig. 4.4, where shear mode frequencies for different harmonics of first radial overtone are plotted for magnetic fields $B_* = 10^3$ and 10^4. We see from Fig. 4.4 that the frequencies of first overtone get reduced when we

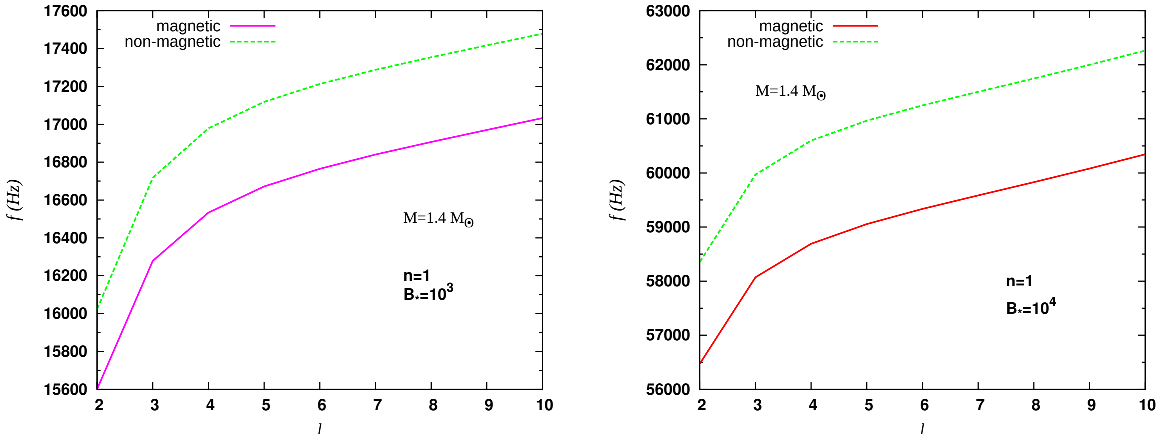

Figure 4.4: Torsional shear mode frequency for non-magnetic as well as magnetic crusts with fields $B_* = 10^3$ (left panel) and $B_* = 10^4$ for different harmonics of first overtone ($n = 1$).

use the magnetized crust and this reduction increases with increasing field strength [94].

Next, we calculate torsional shear mode frequencies of SGRs 1806-20 and 1900+14 and match them with observed frequencies as shown in table 4.1. For SGR 1900+14, the best match is obtained for a neutron star of mass $1.4M_\odot$ and magnetic field $B = 4 \times 10^{14}$ G [94]. It is evident from the table that we obtain very good match for all the four frequencies for this SGR. However, for SGR 1806-20 the match is good only for higher four frequencies with a neutron star of mass $1.2M_\odot$ and magnetic field $B = 8 \times 10^{14}$ G.

Table 4.1: Calculated shear mode frequencies of SGRs 1806-20 and 1900+14 and comparison with observations.

SGR 1806-20				SGR 1900+14			
Observed Frequency (Hz)	Calculated Frequency (Hz)	n	ℓ	Observed Frequency (Hz)	Calculated Frequency (Hz)	n	ℓ
18	15	0	2	28	28	0	4
26	24	0	3	54	55	0	8
29	32	0	4	84	82	0	12
93	93	0	12	155	154	0	23
150	151	0	20				
626	626	1	29				
1838	1834	4	2				

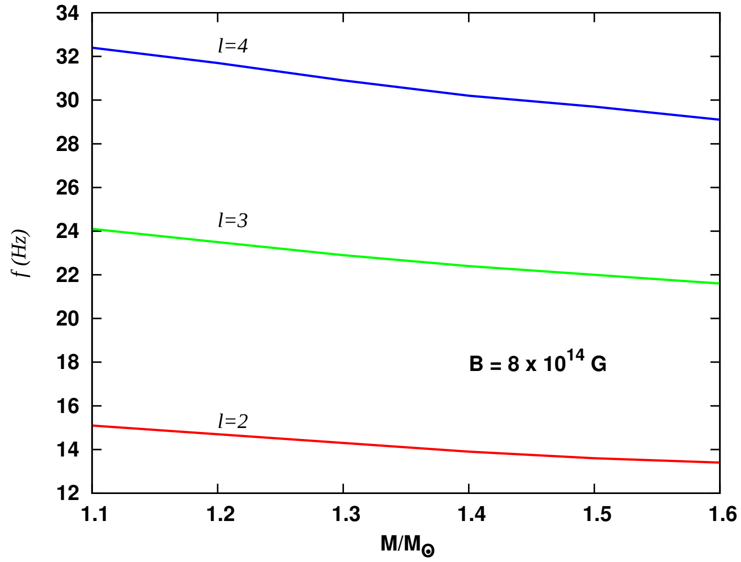

Figure 4.5: Shear mode frequencies for $n = 0$; $l = 2, 3$ and 4 as a function of neutron star mass.

Lower frequencies (18, 26 and 29 Hz) can't be explained with our calculation as these frequencies are too close to be matched by different harmonics of the $n = 0$ mode. However, these frequencies may possibly be explained by considering the Alfvén modes [104].

In Fig. 4.5 we show the dependence of shear mode frequencies on neutron star mass for a magnetic field $B = 8 \times 10^{14}$ G. For all the modes displayed here the frequency decreases with increasing neutron star mass. If the masses of the SGRs can be measured with good precision from observations they can put constrain on the EOS used here.

4.4 Summary and Conclusions

In this chapter, we have estimated frequencies of torsional shear modes of magnetars assuming a dipole magnetic field configuration. Frequencies are computed using our models of magnetized crusts. The shear modulus of magnetized crusts is found to be enhanced in strong magnetic fields $\sim 4.414 \times 10^{17}$ G because electrons populate only the zeroth Landau level. It is observed that frequencies of fundamental ($n = 0, l = 2$)

torsional shear modes are not sensitive to this enhancement in the shear modulus in strong magnetic fields. On the other hand, frequencies of first overtones ($n = 1$) of torsional shear modes in presence of strongly quantizing magnetic fields are distinctly different from those of the field free case. We have compared our results with frequencies of observed QPOs and found good agreement. Observed frequencies could constrain the EOS of magnetized neutron star crusts if masses of neutron stars are known.

Chapter 5

Neutron star Core

5.1 Introduction

In the previous chapter it was seen that the ground state of a neutron star inner crust contains nuclei immersed in electron and neutron gases. With increasing density nuclei come closer to each other and at a density $\sim 0.5\rho_0$ ($\rho_0 \simeq 2.8 \times 10^{14}$ g cm^{-3} is the saturation density of nuclear matter), nuclei no longer exist as they merge together to form a uniform matter of neutrons, protons and electrons. The outer core begins at this point. With increasing density Fermi energy of all the components increase. When the Fermi energy (or, chemical potential) of electrons exceeds the muon rest mass energy ($m_\mu = 105.7$ MeV), muons appear in the system and take part in maintaining the charge neutrality ($n_e + n_\mu = n_p$) and the β-equilibrium ($\mu_n = \mu_p + \mu_e$, $\mu_e = \mu_\mu$) of the system. At density $\rho \gtrsim 2\rho_0$, inner core starts the composition of which is not known and therefore model dependent. There are suggestions that at such high densities transition from $npe\mu$ matter to various exotic phases such as strange baryons (Λ, Σ and Ξ hyperons), Bose-Einstein condensation of pions and (anti)kaons may take place. At ultrahigh densities, matter can dissolve into deconfined quark matter [105].

There are a host of theoretical models describing matter of neutron star cores. The main uncertainty in the calculation of dense matter arises from poorly known many-body interactions. However, several methods have been developed over the years to solve this problem and can be divided into two main categories. In the first category one tries to calculate the ground state energy of the matter starting from a bare nucleon-nucleon (NN) interaction. Models based on Brueckner-Bethe-Goldstone (BBG) theory [106, 107], Green's function method [108, 109], variational method [110] etc fall under this category. In the other category one starts from an effective NN interaction. The non-relativistic Skyrme-type models [70], the relativistic mean field (RMF) model [105,111,112] etc belong to this category.

Any many-body theory of neutron star matter must reproduce the empirical results of bulk nuclear matter: the saturation density, $n_0 = 0.15 - 0.16$ fm^{-3}; the binding energy per nucleon, $E/A = -16 \pm 1$ MeV; effective nucleon mass $m_N^* = 0.7 - 0.8 m_N$; the incompressibility defined as $K = \left[\rho^2 \frac{d^2}{d\rho^2}\left(\frac{\epsilon}{\rho}\right)\right]_{\rho=\rho_0}$ in the range $200 - 300$ MeV and symmetry energy at the saturation given as $a_s = \frac{1}{2}\left(\frac{\partial^2(\epsilon/\rho)}{\partial t^2}\right)_{t=0}$; $t \equiv \frac{\rho_n - \rho_p}{\rho}$ within $30 - 35$ MeV. In this thesis, we employ the RMF model to investigate the properties of dense matter in neutron star interior.

5.2 Relativistic Mean Field (RMF) model

Motivated by the experimental observation of large Lorentz scalar and four-vector components in the NN interaction Walecka [111] introduced a field-theoretical model, also known as $\sigma - \omega$ model, to describe the properties of nuclei as well as nuclear matter. In this model the interaction between nucleons is mediated by the exchange of a scalar (σ) and a vector meson (ω). In the static limit of infinitely heavy baryons, these meson exchanges correspond to an effective NN potential of the form [112]

$$V = \frac{g_\omega^2}{4\pi}\frac{e^{-m_\omega r}}{r} - \frac{g_\sigma^2}{4\pi}\frac{e^{-m_\sigma r}}{r}, \tag{5.1}$$

which with the appropriate choices of the coupling constants (g_σ, g_ω) and and masses (m_σ, m_ω), reproduces the main qualitative behaviors, namely the short range repulsion and the long range attraction of the NN interaction. However, this model was unable to reproduce empirical values of the incompressibility, the effective nucleon mass and the symmetry energy. To gain control over the first two properties Boguta and Bodmer [113] introduced non-linear self-interactions of the scalar meson (σ) in this model. The model was further extended by including a vector-isovector meson (ρ) which accounts for the symmetry energy of the nuclear matter.

5.2.1 Hadronic phase

To describe the pure hadronic phase we consider an extension of the $\sigma-\omega$ model where nucleons interact with each other by the exchange of σ, ω and ρ mesons. The NN interaction is given by the Lagrangian density [105, 114]

$$\begin{aligned}
\mathcal{L}_N &= \bar{\psi}_N \left(i\gamma_\mu \partial^\mu - m_N + g_{\sigma N}\sigma - g_{\omega N}\gamma_\mu \omega^\mu - \frac{1}{2} g_{\rho N}\gamma_\mu \boldsymbol{\tau}_N \cdot \boldsymbol{\rho}^\mu \right) \psi_N \\
&+ \frac{1}{2}\left(\partial_\mu \sigma \partial^\mu \sigma - m_\sigma^2 \sigma^2\right) - U(\sigma) \\
&- \frac{1}{4}\omega_{\mu\nu}\omega^{\mu\nu} + \frac{1}{2} m_\omega^2 \omega_\mu \omega^\mu - \frac{1}{4}\boldsymbol{\rho}_{\mu\nu} \cdot \boldsymbol{\rho}^{\mu\nu} + \frac{1}{2} m_\rho^2 \boldsymbol{\rho}_\mu \cdot \boldsymbol{\rho}^\mu. \qquad (5.2)
\end{aligned}$$

where $\psi_N \equiv (\psi_p, \psi_n)^T$ is the isospin doublet of nucleons with ψ_p and ψ_n being the 4-component Dirac spinors for proton and neutron, respectively; m_N is the nucleon mass; m_σ, m_ω, and m_ρ are masses of mesons; $g_{\sigma N}, g_{\omega N}$ and $g_{\omega N}$ are coupling constants; $\boldsymbol{\rho}$ and $\boldsymbol{\tau}_N$ are vectors in isospin space (isovectors) and $\omega_{\mu\nu}, \boldsymbol{\rho}_{\mu\nu}$ are meson field tensors given by

$$\begin{aligned}
\omega_{\mu\nu} &= \partial_\mu \omega_\nu - \partial_\nu \omega_\mu, \\
\boldsymbol{\rho}_{\mu\nu} &= \partial_\mu \boldsymbol{\rho}_\nu - \partial_\nu \boldsymbol{\rho}_\mu\,. \qquad (5.3)
\end{aligned}$$

The scalar self-interaction [105, 113] is

$$U(\sigma) \;=\; \frac{1}{3}g_1 m_N (g_{\sigma N}\sigma)^3 + \frac{1}{4}g_2 (g_{\sigma N}\sigma)^4. \tag{5.4}$$

The coupling constants are the parameters of the model and can be determined by relating them algebraically to five empirically known quantities of bulk nuclear matter at saturation : $\rho, E/A, m_N^*, K$ and a_s.

Equations of motion for the fields are obtained from Euler-Lagrange equation

$$\partial_\mu \frac{\partial \mathcal{L}}{\partial(\partial_\mu \phi)} = \frac{\partial \mathcal{L}}{\partial \phi}, \tag{5.5}$$

where ϕ represents fields ψ_N, σ, ω and ρ. Using this Eq. (5.5) along with Eq. (5.2) we get the Dirac equation for nucleons

$$\left[\gamma^\mu \left(i\partial_\mu - g_{\omega N}\omega_\mu - \frac{1}{2}g_{\rho N}\boldsymbol{\tau}_N \cdot \boldsymbol{\rho}_\mu\right) - (m_N - g_{\sigma N}\sigma)\right]\psi_N = 0\,. \tag{5.6}$$

For mesons we get following equations of motions

$$(\Box + m_\sigma^2)\sigma \;=\; g_{\sigma N}\bar{\psi}_N\psi_N - \frac{\partial U}{\partial \sigma}\,, \tag{5.7}$$

$$(\Box + m_\omega^2)\omega_\mu \;=\; g_{\omega N}\bar{\psi}_N\gamma_\mu\psi_N\,, \tag{5.8}$$

$$(\Box + m_\rho^2)\boldsymbol{\rho}_\mu \;=\; \frac{1}{2}g_{\rho N}\bar{\psi}_N\gamma_\mu\boldsymbol{\tau}_N\psi_N\,, \tag{5.9}$$

with $\Box \equiv \partial^\mu\partial_\mu$.

The last four equations form a set of coupled nonlinear differential equations and therefore very difficult to solve exactly. Moreover, coupling constants are expected to be large which make perturbation approach inapplicable. However, in the context of studying dense and uniform matter of neutron stars we can use the *mean-filed approximation* where the meson field operators are replaced by their ground state expectation values as

$$
\begin{aligned}
\sigma &\rightarrow <\sigma> \\
\omega_\mu &\rightarrow <\omega_\mu> \\
\boldsymbol{\rho}_\mu &\rightarrow <\boldsymbol{\rho}_\mu>
\end{aligned}
$$

The validity of this approximation improves with density as at large densities source terms of Eqs. (5.7)-(5.9) increase which in turn increase the justification of the above replacements. The expectation values of space components of $\omega_\mu, \boldsymbol{\rho}_\mu$ vanish due to the rotational symmetry of the system. The first two components of the isovector field ($\boldsymbol{\rho}$) also have vanishing expectation values in the ground state so that only the third component survives. Moreover, in the rest frame of this uniform matter the fields are independent of space and time. Considering all these together we get greatly simplified equations of motion for nucleons as well as mesons

$$
\begin{aligned}
\left[\gamma^0\left(i\partial_0 - g_{\omega N}\omega_0 - \frac{1}{2}g_{\rho N}\tau_{3N}\rho_{03}\right) \right. &- \left.(m_N - g_{\sigma N}\sigma)\right]\psi_N = 0\,, &(5.10)\\
m_\sigma^2\sigma &= -\frac{\partial U}{\partial\sigma} + g_{\sigma N} <\bar{\psi}_N\psi_N>\,, &(5.11)\\
m_\omega^2\omega_0 &= g_{\omega N} <\psi_N^\dagger\psi_N>\,, &(5.12)\\
m_\rho^2\rho_{03} &= \frac{1}{2}g_{\rho N} <\psi_N^\dagger\tau_{3N}\psi_N>\ . &(5.13)
\end{aligned}
$$

As there is no space-time dependence in these equations we look for the stationary solution for nucleons of the form

$$\psi_N = u(\vec{k})e^{i(\vec{k}\cdot\vec{x}-\varepsilon(k)t)}\,, \tag{5.14}$$

where $u(k)$ is an 8-component spinor. When this ψ_N is substituted in Eq. (5.10) we get the eigenvalue equation

$$(\vec{\alpha}\cdot\vec{k} + \beta m_N^*)u(\vec{k}) = (\varepsilon(k) - g_{\omega N}\omega_0 - \frac{1}{2}g_{\rho N}\tau_{3N}\rho_{03})u(\vec{k})\,, \tag{5.15}$$

with eigenvalue

$$\varepsilon(k) - g_{\omega N}\omega_0 - \frac{1}{2}g_{\rho N}\tau_{3N}\rho_{03} = \pm(\vec{k}^2 + m_N^{*2})^{1/2}\,,$$

which yields,

$$\varepsilon(k) = g_{\omega N}\omega_0 + \frac{1}{2}g_{\rho N}\tau_{3N}\rho_{03} \pm (\vec{k}^2 + m_N^{*2})^{1/2} = \varepsilon_\pm(k). \tag{5.16}$$

where m_N^* is the effective nucleon mass given as

$$m_N^* = m_N - g_{\sigma N}\sigma\,. \tag{5.17}$$

The general solution for the field operator ψ_N is written as

$$\psi_N = \frac{1}{\sqrt{V}}\sum_s \int d\vec{k}\left[a_s(\vec{k})u_s(\vec{k})e^{-i\varepsilon_+(\vec{k})t + i\vec{k}\cdot\vec{x}} + b_s^\dagger(\vec{k})v_s(\vec{k})e^{-i\varepsilon_-(\vec{k})t - i\vec{k}\cdot\vec{x}}\right]\,, \tag{5.18}$$

where $u_s(\vec{k})$ and $v_s(\vec{k})$ are positive and negative energy spinors, respectively; $a_s(\vec{k})$ denotes the annihilation operator for particles whereas $b_s^\dagger(\vec{k})$ stands for the creation operator for antiparticles. However, we do not consider antiparticles in our calculation as there is no antiparticle present in the ground state ($T = 0$) of uniform nuclear matter. Nucleons being fermions occupy all the energy levels upto their Fermi energies ($\varepsilon_f \equiv \varepsilon(k = k_f)$), which are also their chemical potentials (μ), in the ground state.

The expectations value appearing in the RHS of the field equation (5.12) gives the total baryon number density of the system

$$\begin{aligned} n \equiv <\psi_N^\dagger\psi_N> &= \frac{2}{(2\pi)^3}\int_0^{k_{f_p}} d\vec{k} + \frac{2}{(2\pi)^3}\int_0^{k_{f_n}} d\vec{k} \\ &= \frac{k_{f_p}^3}{3\pi^2} + \frac{k_{f_n}^3}{3\pi^2} \\ &= n_p + n_n\;. \end{aligned} \tag{5.19}$$

Similarly, for other expectation values we get scalar and vector baryon densities as

$$n_s \equiv < \bar{\psi}_N \psi_N >= \frac{2}{\pi^2} \int_0^{k_{fp}} k^2 dk \frac{m_N^*}{\sqrt{k^2 + m_N^{*2}}} + \frac{2}{\pi^2} \int_0^{k_{fn}} k^2 dk \frac{m_N^*}{\sqrt{k^2 + m_N^{*2}}} \,, \tag{5.20}$$

and

$$\begin{aligned} n_v \equiv < \psi_N^\dagger \tau_{3N} \psi_N > &= \frac{2}{(2\pi)^3} \int_0^{k_{fp}} d\vec{k} - \frac{2}{(2\pi)^3} \int_0^{k_{fn}} d\vec{k} \\ &= n_p - n_n \,. \end{aligned} \tag{5.21}$$

Expression for energy density and pressure for nucleons can be obtained from Energy-momentum tensor as

$$\epsilon_N = < T^{00} >= - < \mathcal{L}_N > + < \psi_N \gamma_0 \partial_0 \psi_N > \,, \tag{5.22}$$

$$P_N = \frac{1}{3} < T^{ii} >=< \mathcal{L}_N > + \frac{1}{3} < \bar{\psi}_N \gamma^i \partial_i \psi_N > \ . \tag{5.23}$$

After evaluating the expectation values we get

$$\begin{aligned} \epsilon_N &= \frac{1}{3} g_1 m_N (g_{\sigma N} \sigma)^3 + \frac{1}{4} g_2 (g_{\sigma N} \sigma)^4 + \frac{1}{2} m_\sigma^2 \sigma^2 + \frac{1}{2} m_\omega^2 \omega_0^2 + \frac{1}{2} m_\rho^2 \rho_{03}^2 \\ &+ \frac{1}{\pi^2} \left[\int_0^{k_{fp}} \sqrt{k^2 + m_N^{*2}}\, k^2 dk + \int_0^{k_{fn}} \sqrt{k^2 + m_N^{*2}}\, k^2 dk \right] \,, \end{aligned} \tag{5.24}$$

$$\begin{aligned} P_N &= -\frac{1}{3} g_1 m_N (g_{\sigma N} \sigma)^3 - \frac{1}{4} g_2 (g_{\sigma N} \sigma)^4 - \frac{1}{2} m_\sigma^2 \sigma^2 + \frac{1}{2} m_\omega^2 \omega_0^2 + \frac{1}{2} m_\rho^2 \rho_{03}^2 \\ &+ \frac{1}{3\pi^2} \left[\int_0^{k_{fp}} \frac{k^4 dk}{\sqrt{k^2 + m_N^{*2}}} + \int_0^{k_{fn}} \frac{k^4 dk}{\sqrt{k^2 + m_N^{*2}}} \right] \,. \end{aligned} \tag{5.25}$$

Leptons form uniform Fermi gases and their energy density and pressure can be easily calculated as

$$\epsilon_L = \sum_{l=e,\mu} \frac{1}{\pi^2} \int_0^{k_{F_l}} (k^2 + m_l^{*2})^{1/2} k^2 dk \,, \tag{5.26}$$

$$P_L = \frac{1}{3} \sum_{l=e,\mu} \frac{1}{\pi^2} \int_0^{k_{F_l}} \frac{k^4 dk}{(k^2 + m_l^{*2})^{1/2}} \,. \tag{5.27}$$

Now, we have the total energy density and pressure of the system :

$$\epsilon = \epsilon_N + \epsilon_L \,, \tag{5.28}$$

$$P = P_N + P_L \,. \tag{5.29}$$

So, knowing the masses and coupling constants the EOS of the nuclear matter can be calculated using Eqs. (5.11)-(5.13), (5.19)-(5.21) and (5.24)-(5.29).

5.2.2 Kaon condensed phase

By using a chiral $SU(3)_L \times SU(3)_R$ Lagrangian, Kaplan and Nelson [115] first demonstrated the possibility of the existence of an (anti)kaon (K^-) condensed phase in dense nuclear matter. (Anti)kaon begins to appear in the system when its effective in-medium energy or the chemical potential becomes equal to the chemical potential of electrons i.e.

$$\omega_{K^-} = \mu_{K^-} = \mu_e . \tag{5.30}$$

Generally μ_e increases as the baryon density increases. But the effective energy of K^- in the nuclear medium decreases with increasing density because of their attractive s-wave interaction with the nuclear medium. Therefore, at some density the above threshold condition may be fulfilled and K^- may appear through the following strangeness changing processes

$$n \to p + K^- \,, \qquad e^- \to K^- + \nu_e \,. \tag{5.31}$$

The appearance of K^- lowers the energy of the system in two ways :

i) Because of its bosonic character K^- mesons may form a condensate in the lowest momentum ($k = 0$) state and thereby save the kinetic energy of electrons they replace.

ii) With the appearance of K^- mesons the proton fraction of the matter also increases which in turn reduces the symmetry energy of nuclear matter.

A pure (anti)kaon condensed phase contains nucleons (we don't consider hyperons), leptons (electron, muon) as well as the (anti)kaon. For the interaction between nucleons we consider the same Lagrangian as before in Eq. 5.2. Interaction between kaons and nucleons can be treated in two ways - within the chiral perturbation theory [115–117] or within the kaon-meson coupling scheme. To treat the interactions of kaons on the same footing as nucleons we adopt the latter approach and use the Lagrangian density for the kaon in the minimal coupling scheme introduced by Glendenning and Schaffner-Bielich (1999) and is given by [118]

$$\mathcal{L}_K = D^*_\mu \bar{K} D^\mu K - m_K^{*2} \bar{K} K, \tag{5.32}$$

where $K \equiv (K^+, K^0)$ and $\bar{K} \equiv (K^-, \bar{K}^0)$ denote kaon and antikaon isospin doublets, respectively. D_μ is the covariant derivative

$$D_\mu = \partial_\mu + i g_{\omega K} \omega_\mu + i g_{\rho K} \boldsymbol{\tau}_K \cdot \boldsymbol{\rho}_\mu \,, \tag{5.33}$$

m_K^* is the effective mass of the kaon

$$m_K^* = m_K - g_{\sigma K} \sigma \,, \tag{5.34}$$

and $g_{\sigma K}, g_{\omega K}$ and $g_{\rho K}$ are the kaon-meson coupling constants. The equation of motion for the kaon is

$$(D_\mu D^\mu + m_K^{*2}) K = 0. \tag{5.35}$$

At this point we employ the *mean-field approximation* discussed in Sec. (5.2) and for static and uniform neutron star matter we get the expression for the in-medium energy of K^- mesons as

$$\omega_{K^-} = \sqrt{(k^2 + m_K^{*2})} - g_{\omega K}\omega_0 - \frac{1}{2} g_{\rho K}\rho_{03}. \tag{5.36}$$

For the s-wave condensation ($\vec{k} = 0$) we obtain

$$\omega_{K^-} = m_K^* - g_{\omega K}\omega_0 - \frac{1}{2} g_{\rho K}\rho_{03}. \tag{5.37}$$

So, we see that the interaction of K^- mesons with the nuclear medium causes a reduction in its energy which has also become density dependent through the meson fields σ, ω_0 and ρ_{03}. With increasing density meson fields generally increase which in turn decreases ω_{K^-} and when it becomes equal to the μ_e, K^- mesons appear in the system.

The meson field equations (5.11)-(5.13) get modified in the presence of the K^- condensate as

$$m_\sigma^2 \sigma = -\frac{\partial U}{\partial \sigma} + g_{\sigma N} n_s + g_{\sigma K} n_K \, , \tag{5.38}$$

$$m_\omega^2 \omega_0 = g_{\omega N} n - g_{\omega K} n_K \, , \tag{5.39}$$

$$m_\rho^2 \rho_{03} = \frac{1}{2} g_{\rho N}(\rho_p - \rho_n) - g_{\rho K} n_K \, . \tag{5.40}$$

where n_K is the vector density of the kaon and for the s-wave condensation considered here this is also the scalar density and is given by

$$n_K = 2(\omega_K + g_{\omega K}\omega_0 + g_{\omega K}\rho_{03})\bar{K}K = 2m_K^*\bar{K}K \tag{5.41}$$

The total charge density of the K^- condensate phase is calculated as

$$Q_K = n_p - n_e - n_\mu - n_k \tag{5.42}$$

As all the K^- mesons have zero momentum in the s-wave condensation, they don't have any direct contribution to the total pressure and can be calculated from Eq. (5.29) using modified meson field equations (5.38)-(5.40) in the presence of a K^- condensate . But they do contribute to the total energy density of the system through the term

$$\epsilon_K = m_K^* n_K \, , \tag{5.43}$$

so that the total energy density becomes

$$\epsilon = \epsilon_N + \epsilon_L + \epsilon_K \, . \tag{5.44}$$

5.2.3 Mixed phase

The transition from the hadronic phase to the K^- condensed phase in neutron stars is mainly of first order, but can also be of second order. The first order transition goes through a mixed phase where both the phases coexist in equilibrium. For a single component system having only one conserved quantity this equilibrium is governed by the Gibbs conditions:

$$\begin{aligned} \mu^I &= \mu^{II} = \mu \\ T^I &= T^{II} = T \\ P^I(\mu, T) &= P^{II}(\mu, T) = P \end{aligned} \tag{5.45}$$

For a fixed temperature the last equation of (5.45) gives an unique solution for μ which is generally determined by using the Maxwell construction. However, the ground state of neutron star matter is a two component system with two conserved quantities namely the total baryon density and the total electric charge. This gives two independent chemical potentials which we can choose as μ_n and μ_e so that the Gibbs conditions are now given by [105] (for $T = 0$)

$$
\begin{aligned}
\mu_e^H &= \mu_e^K \\
\mu_n^H &= \mu_n^K \\
P^H(\mu_e, \mu_n) &= P^K(\mu_e, \mu_n)\,.
\end{aligned}
\tag{5.46}
$$

Here, H and K stand for the hadronic and the K^- condensed phases, respectively. Unlike the Maxwell case here the equilibrium quantities (P, μ) don't remain constant throughout the mixed phase, instead they depend on the proportion of the two equilibrium phases. In the mixed phase the charge neutrality condition reads as

$$
(1-\chi)Q_H + \chi Q_K = 0\,, \tag{5.47}
$$

where χ is the volume fraction occupied by the condensed phase. Similarly for the total baryon number density and the energy density of the mixed phase are given by

$$
n_{MP} = (1-\chi)n_H + \chi n_K\,, \tag{5.48}
$$

$$
\epsilon_{MP} = (1-\chi)\epsilon_H + \chi \epsilon_K\,. \tag{5.49}
$$

where n_H and ϵ_H are the baryon number density and the energy density in the hadronic phase respectively and n_K and ϵ_K are the corresponding quantities in the K^- condensed phase.

5.3 Parameter sets

The EOS of the neutron star matter can be obtained within the framework of RMF theory if all the coupling constants appearing in the theory are known. To determine the coupling constants we rely on the empirical values of the bulk nuclear matter properties defined

Table 5.1: GM1 parameter set that reproduces saturation density $n_0 = 0.153$ fm^{-3}, binding energy $E/A = -16.3$ MeV, $m_N^*/m_N = 0.70$, incompressibility $K = 300$ MeV and symmetry energy coefficient $a_s = 32.5$ MeV. Masses are taken as $m_N = 938$ MeV, $m_\sigma = 550$ MeV, $m_\omega = 783$ MeV and $m_\rho = 770$ MeV.

$g_{\sigma N}$	$g_{\omega N}$	$g_{\rho N}$	g_1	g_2 (fm^{-1})
9.5708	10.5964	8.1957	12.2817	-8.9780

Table 5.2: Kaon-scalar meson coupling constants for the GM1 parameter set at different values of K^- optical potential depth U_K.

U_K (MeV)	-100	-120	-140	-160	-180
GM1	0.9542	1.6337	2.3142	2.9937	3.6742

earlier in the chapter, at the saturation density.

5.3.1 Nucleon-Meson coupling constants

There are five unknown coupling constants $g_{\sigma N}, g_{\omega N}, g_{\rho N}, g_1$ and g_2 in the nucleon-meson interaction Lagrangian given by Eq. (5.2). For our calculation we use the GM1 parameter set introduced by Glendenning and Moszkowski (1991) [119] as it predicts a maximum neutron star mass compatible with the most recent observed neutron star mass of $1.97 M_\odot$. The values of the parameters of this set are listed in table 5.1.

5.3.2 Kaon-Meson coupling constants

Coupling constants for the kaon-meson interaction (Eq. 5.32) are determined by using the quark model and isospin counting rule. For the vector coupling constants we have

$$g_{\omega K} = \frac{1}{3} g_{\omega N} \qquad and \qquad g_{\rho K} = g_{\rho N} \, . \tag{5.50}$$

The real part of the K^- optical potential depth at the saturation density provides the scalar coupling constant as

$$U_K(n_0) = -g_{\sigma K}\sigma - g_{\omega K}\omega_0\,. \tag{5.51}$$

We have seen in the Section (5.2.2) that the interaction of K^- mesons with the nuclear matter is attractive in nature. On the one hand, the analysis of K^- atomic data indicated that the real part of the optical potential could be as large as $U_K = -180 \pm 20$ MeV at normal nuclear matter density [120, 121]. On the other hand, chirally motivated coupled channel models with a self-consistency requirement predicted shallow potential depths of $-$40-60 MeV [122, 123]. Further, the highly attractive potential depth of several hundred MeV was obtained in the calculation of deeply bound K^--nuclear states [124, 125]. An alternative explanation to the deeply bound K^--nuclear states was given by others [126]. This shows that the value of K^- optical potential depth is still a debatable issue. The values of kaon-scalar meson coupling constants corresponding to the GM1 parameter set and for various values of K^- optical potential depths are listed in table 5.2.

Chapter 6

Shear viscosity in dense matter

6.1 Introduction

Shear viscosity plays important roles in neutron star physics. It might damp the r-mode instability below the temperature $\sim 10^8$ K [127]. The knowledge of shear viscosity is essential in understanding pulsar glitches and free precession of neutron stars [128]. The calculation of the neutron shear viscosity (η_n) for nonsuperfluid matter using free-space nucleon-nucleon scattering data was first done by Flowers and Itoh [129, 130]. Cutler and Lindblom [131] fitted the results of Flowers and Itoh [130] for the study of viscous damping of oscillations in neutron stars. Recently the neutron shear viscosity of pure neutron matter has been investigated in a self-consistent way [132].

It was noted that electrons, the lightest charged particles and neutrons, the most abundant particles in neutron star matter contribute significantly to the total shear viscosity. Flowers and Itoh found that the neutron viscosity was larger than the combined viscosity of electrons and muons ($\eta_{e\mu}$) in non-superfluid matter [130]. Further Cutler and Lindblom argued that the electron viscosity was larger than the neutron viscosity in a superfluid neutron star [131]. Later Andersson and his collaborators as well as Shtertin and his collaborator showed $\eta_{e\mu} > \eta_n$ in the presence of proton superfluidity [128,133]. In the latter calculation, the effects of the exchange of transverse plasmons in the collisions of charged particles were included and it lowered the $\eta_{e\mu}$ compared with the case when only longitudinal plasmons were considered [133].

So far, all of those calculations of shear viscosity were done in neutron star matter composed of neutrons, protons, electrons and muons. However, exotic forms of matter such as hyperon or antikaon condensed matter might appear in the interior of neutron stars as discussed in the previous chapters. Negatively charged hyperons or a K^- condensate could affect the electron shear viscosity appreciably.

Here we focus on the role of K^- meson condensates on the shear viscosity. No calculation of shear viscosity involving K^- condensation has been carried out so far. This motivates us to investigate the shear viscosity in the presence of a K^- condensate. The K^- condensate appears at 2-3 times the normal nuclear matter density. With the onset of the condensate, K^- mesons replace electrons and muons in the core. As a result, K^- mesons along with protons maintain the charge neutrality. It was noted that the proton fraction became comparable to the neutron fraction in a neutron star including the K^- condensate at higher densities [134–136]. The appearance of the K^- condensate would not only influence the electron and muon shear viscosities but it will also give rise to a new contribution called the proton shear viscosity [137].

This chapter is organized in the following way. In section 6.2 , we describe the calculation of shear viscosity in neutron stars involving the K^- condensate. Results are discussed in section 6.3. A summary is given in section 6.4.

6.2 Formalism

Here we are interested in calculating the shear viscosity of neutron star matter in the presence of an antikaon condensate. We consider neutron star matter undergoing a first order phase transition from charge neutral and beta-equilibrated nuclear matter to a K^-

condensed phase. The nuclear phase is composed of neutrons, protons, electrons and muons whereas the K^- condensed phase is made up of neutrons and protons embedded in the Bose-Einstein condensate of K^- mesons along with electrons and muons. Antikaons form a s-wave (with momentum $\mathbf{k} = \mathbf{0}$) condensation in this case. Therefore, K^- mesons in the condensate do not take part in momentum transfer during collisions with other particles. However, the condensate influences the proton fraction and equation of state (EOS) which, in turn, might have important consequences for the shear viscosity.

6.2.1 Solving the Boltzmann transport equation

The starting point for the calculation of the shear viscosity is a set of coupled Boltzmann transport equations [130, 133] for the i-th particle species ($i = n, p, e, \mu$) with velocity v_i and distribution function F_i,

$$\vec{v}_i \cdot \vec{\bigtriangledown} F_i = \sum\nolimits_{j=n,p,e,\mu} I_{ij}. \tag{6.1}$$

The transport equations are coupled through collision integrals given by,

$$I_{ij} = \frac{V^3}{(2\pi)^9(1+\delta_{ij})} \sum_{s_{i'},s_j,s_{j'}} \int d\mathbf{k}_j d\mathbf{k}_{i'} d\mathbf{k}_{j'} W_{ij} \mathcal{F} \ , \tag{6.2}$$

where

$$\mathcal{F} = [F_{i'}F_{j'}(1-F_i)(1-F_j) - F_iF_j(1-F_{i'})(1-F_{j'})] \ . \tag{6.3}$$

Here $\mathbf{k}_i$, $\mathbf{k}_j$ are momenta of incident particles and $\mathbf{k}_{i'}$, $\mathbf{k}_{j'}$ are those of final states. The Kronecker delta in Eq. (6.2) is inserted to avoid double counting for identical particles. Spins are denoted by s and W_{ij} is the differential transition rate. The non-equilibrium distribution function for the i-th species F_i is given by

$$F_i = f_i - \phi_i \frac{\partial f_i}{\partial \epsilon_i} \ , \tag{6.4}$$

where f_i denotes the equilibrium Fermi-Dirac distribution function for the i-th species

$$f(\epsilon_i) = \frac{1}{1 + \exp[(\epsilon_i - \mu_i)/k_B T]} \tag{6.5}$$

and ϕ_i gives the departure from the equilibrium. We adopt the following ansatz for ϕ_i [133, 138]

$$\phi_i = -\tau_i(v_i k_j - \frac{1}{3} v_i k_i \delta_{ij})(\bigtriangledown_i \mathcal{V}_j + \bigtriangledown_j \mathcal{V}_i - \frac{2}{3}\delta_{ij} \vec{\bigtriangledown} \cdot \vec{\mathcal{V}}) \ , \tag{6.6}$$

where τ_i is the effective relaxation time for the i-th species and $\mathcal{V}$ is the flow velocity.

To solve the transport equation (6.1) we linearize it by replacing F_i with f_i in the LHS and in the RHS we keep the lowest non-vanishing power of $(F_i - f_i)$ [139]. Multiplying both sides of Eq. (6.1) by $(2\pi)^{-3}(v_i p_j - \frac{1}{3} v_i p_i \delta_{ij}) d\mathbf{k}_i$ and summing over spin s_i and integrating over $d\mathbf{k}_i$ we obtain a set of relations between effective relaxation times and collision frequencies [133]

$$\sum_{j=n,p,e,\mu} (\nu_{ij}\tau_i + \nu'_{ij}\tau_j) = 1, \tag{6.7}$$

and the effective collision frequencies are

$$\nu_{ij} = \frac{3\pi^2}{2p_{f_i}^5 k_B T m_i^* (1+\delta_{ij})} \sum_{s_i, s_{i'}, s_j, s_{j'}} \int \frac{d\mathbf{k}_i d\mathbf{k}_j d\mathbf{k}_{i'} d\mathbf{k}_{j'}}{(2\pi)^{12}} W_{ij} [f_i f_j (1 - f_{i'})(1 - f_{j'})] \\ \times \left[\frac{2}{3} k_i^4 + \frac{1}{3} k_i^2 k_{i'}^2 - (\mathbf{k}_i \cdot \mathbf{k}_{i'})^2\right] , \tag{6.8}$$

$$\nu'_{ij} = \frac{3\pi^2}{2p_{f_i}^5 k_B T m_j^* (1+\delta_{ij})} \sum_{s_i, s_{i'}, s_j, s_{j'}} \int \frac{d\mathbf{k}_i d\mathbf{k}_j d\mathbf{k}_{i'} d\mathbf{k}_{j'}}{(2\pi)^{12}} W_{ij} [f_i f_j (1 - f_{i'})(1 - f_{j'})] \\ \times \left[\frac{1}{3} k_i^2 k_{j'}^2 - \frac{1}{3} k_i^2 k_j^2 + (\mathbf{k}_i \cdot \mathbf{k}_j)^2 - (\mathbf{k}_i \cdot \mathbf{k}_{j'})^2\right] . \tag{6.9}$$

The differential transition rate is given by

$$\sum_{s_i, s_{i'}, s_j, s_{j'}} W_{ij} = 4(2\pi)^4 \delta(\epsilon_i + \epsilon_j - \epsilon_{i'} - \epsilon_{j'}) \delta(\mathbf{k}_i + \mathbf{k}_j - \mathbf{k}_{i'} - \mathbf{k}_{j'}) \mathcal{Q}_{ij} \ , \tag{6.10}$$

where $\mathcal{Q}_{ij} =< |\mathcal{M}_{ij}|^2 >$ is the squared matrix element summed over final spins and averaged over initial spins.

We obtain effective relaxation times for different particle species solving a matrix equation that follows from Eq. (6.7). The matrix equation has the following form:

$$\begin{pmatrix} \nu_e & \nu'_{e\mu} & \nu'_{ep} & 0 \\ \nu'_{\mu e} & \nu_\mu & \nu'_{\mu p} & 0 \\ \nu'_{pe} & \nu'_{p\mu} & \nu_p & \nu'_{pn} \\ 0 & 0 & \nu'_{np} & \nu_n \end{pmatrix} \begin{pmatrix} \tau_e \\ \tau_\mu \\ \tau_p \\ \tau_n \end{pmatrix} = 1 \tag{6.11}$$

where,

$$\begin{aligned} \nu_e &= \nu_{ee} + \nu'_{ee} + \nu_{e\mu} + \nu_{ep} \ , \\ \nu_\mu &= \nu_{\mu\mu} + \nu'_{\mu\mu} + \nu_{\mu e} + \nu_{\mu p} \ , \\ \nu_p &= \nu_{pp} + \nu'_{pp} + \nu_{pn} + \nu_{pe} + \nu_{p\mu} \ , \\ \nu_n &= \nu_{nn} + \nu'_{nn} + \nu_{np} \ . \end{aligned} \tag{6.12}$$

It is to be noted here that the proton-proton interaction is made up of contributions from electromagnetic and strong interactions. As there is no interference of the electromagnetic and strong interaction terms, the differential transition rate for the proton-proton scattering is the sum of electromagnetic and strong contributions [130]. Therefore, we can write the strong and electromagnetic parts of the effective collision frequencies of proton-proton scattering as [137]

$$\begin{aligned} \nu_{pp} &= \nu^s_{pp} + \nu^{em}_{pp} \ , \\ \nu'_{pp} &= \nu'^{s}_{pp} + \nu'^{em}_{pp} \ . \end{aligned} \tag{6.13}$$

Here the superscripts 'em' and 's' denote the electromagnetic and strong interactions.

Solutions of Eq. (6.11) are given below

$$\begin{aligned}
\tau_e &= \Big[(\nu_p\nu_n - \nu'_{pn}\nu'_{np})(\nu_\mu - \nu'_{e\mu}) + (\nu'_{pn} - \nu_n)(\nu_\mu\nu'_{ep} - \nu'_{e\mu}\nu'_{\mu p}) + \nu_n\nu'_{p\mu}(\nu'_{ep} - \nu'_{\mu p})\Big]/\det A, \\
\tau_p &= \Big[(\nu_n - \nu'_{pn})(\nu_e\nu_\mu - \nu'_{e\mu}\nu'_{\mu e}) + \nu'_{p\mu}\nu_n(\nu'_{e\mu} - \nu_e) + \nu'_{pe}\nu_n(\nu'_{e\mu} - \nu_\mu)\Big]/\det A\,, \\
\tau_n &= \Big[(\nu_p - \nu'_{np})(\nu_e\nu_\mu - \nu'_{e\mu}\nu'_{\mu e}) + (\nu'_{np} - \nu'_{\mu p})(\nu'_{p\mu}\nu_e - \nu'_{e\mu}\nu'_{p\mu}) \\
&\quad + (\nu'_{ep} - \nu'_{np})(\nu'_{\mu e}\nu'_{p\mu} - \nu'_{pe}\nu_\mu)\Big]/\det A\,. \qquad (6.14)
\end{aligned}$$

where A is the 4×4 matrix of Eq. (6.11) and $\det A = [\nu_e\nu_\mu(\nu_p\nu_n - \nu'_{pn}\nu'_{np}) - \nu_e\nu'_{\mu p}\nu'_{p\mu}\nu_n - \nu'_{e\mu}\nu'_{\mu e}(\nu_p\nu_n - \nu'_{pn}\nu'_{np}) - \nu'_{e\mu}\nu'_{\mu p}\nu'_{pe}\nu_n + \nu'_{ep}\nu'_{\mu e}\nu'_{p\mu}\nu_n - \nu'_{ep}\nu_\mu\nu'_{pe}\nu_n]$. We obtain τ_μ from τ_e replacing e by μ. In the next paragraphs, we discuss the determination of matrix element squared for electromagnetic and strong interactions.

6.2.2 Electromagnetic interaction

First we focus on the electromagnetic scattering of charged particles. Here we adopt the plasma screening of the interaction due to the exchange of longitudinal and transverse plasmons as described in Refs. [133, 140, 141]. The matrix element for the collision of identical charged particles is given by $M_{12} = M_{12}^{(1)} + M_{12}^{(2)}$, where the first term implies the scattering channel $12 \to 1'2'$ and the second term corresponds to that of $12 \to 2'1'$. The scattering of charged particles in neutron star interiors involves small momentum and energy transfers. Consequently both channels contribute equally as the interference term is small in this case. The matrix element for nonidentical particles is given by [133,140,141]

$$M_{12\to 1'2'} = 4\pi e^2 \left(\frac{J^0_{1'1} J^0_{2'2}}{q^2 + \Pi_l^2} - \frac{\mathbf{J}_{t1'1} \cdot \mathbf{J}_{t2'2}}{q^2 - \omega^2 + \Pi_t^2} \right) , \qquad (6.15)$$

where $\mathbf{q}$ and ω are momentum and energy transfers, respectively in the neutron star interior; $J^\mu_{i'i}$ is the transition 4-current given as $J^\mu_{i'i} = (J^0_{i'i}, \boldsymbol{J}_{i'i}) = (\bar{u}_{i'}\gamma^\mu u_i)/2m_i^*$ where u_i and $\bar{u}_i$ are, respectively, the Dirac spinor and its conjugate satisfying the normalization

$\bar{u}_i u_i = 2m_i$; $\mathbf{J}_t$ is the transverse component of $\mathbf{J}$ with respect to $\mathbf{q}$ and the longitudinal component is written in terms of the time-like component J_0 by using the current conservation relation $q^\mu J_\mu = \omega J_0 - q J_l = 0$ [141]. Polarization functions Π_l and Π_t are associated with the plasma screening of charged particles' interactions through the exchange of longitudinal and transverse plasmons, respectively. They are evaluated within random phase approximation and for typical conditions of neutron star core they are given by [133]

$$\begin{aligned} \Pi_l &= q_l^2 = \frac{4e^2}{\pi} \sum_i m_i^* k_{f_i} \,, \\ \Pi_t &= i\frac{\pi}{4}\frac{\omega}{q} q_t^2 = i e^2 \frac{\omega}{q} \sum_i k_{f_i} \,, \end{aligned} \tag{6.16}$$

where q_l and q_t are longitudinal and transverse plasma wave numbers respectively. After evaluating the matrix element squared and doing the angular and energy integrations, the effective collision frequencies are calculated following the prescription of Refs. [133, 140]. The collision frequencies of Eqs. (6.8) and (6.9) for charged particles become

$$\begin{aligned} \nu_{ij} &= \nu_{ij}^{||} + \nu_{ij}^{\perp}, \\ \nu'_{ij} &= \nu'^{||\perp}_{ij} \,, \end{aligned} \tag{6.17}$$

where $\nu_{ij}^{||}$ and $\nu_{ij}^{\perp}$ correspond to the charged particle interaction due to the exchange of longitudinal and transverse plasmons and $\nu_{ij}^{||\perp}$ is the result of the interference of both interactions. For small momentum and energy transfers, different components of the collision frequency are given by [133, 140]

$$\begin{aligned} \nu_{ij}^{\perp} &= \frac{\alpha e^4 k_{f_j}^2}{m_i^* k_{f_i}} \frac{(k_B T)^{5/3}}{q_t^{2/3}} \,, \\ \nu_{ij}^{||} &= \frac{e^4 \pi^2 m_i^* m_j^{*2}}{k_{f_i}^3 q_l} (k_B T)^2 \,, \\ \nu'^{||\perp}_{ij} &= \frac{2e^4 \pi^2 m_i^* k_{f_j}^2}{k_{f_i}^3 q_l} (k_B T)^2 \,, \end{aligned} \tag{6.18}$$

where $i, j = e, \mu, p$. The value of $\alpha = 2(\frac{4}{\pi})^{1/3}\Gamma(8/3)\zeta(5/3) \sim 6.93$ where $\Gamma(x)$ and $\zeta(x)$ are gamma and Riemann zeta functions, respectively. The shear viscosities of electrons and muons are given by [133].

$$\eta_{i(=e,\mu)} = \frac{n_i k_{f_i}^2 \tau_i}{5m_i^*} \,. \tag{6.19}$$

Here effective masses (m_i^*) of electrons and muons are equal to their corresponding chemical potentials because of relativistic effects. It was noted that the shear viscosity was reduced due to the inclusion of plasma screening by the exchange of transverse plasmons [133, 140]. It is worth mentioning here that we extend the calculation of the collision frequencies for electrons and muons in Refs. [133, 140] to that of protons due to electromagnetic interaction. Before the appearance of the condensate in our calculation, protons may be treated as passive scatterers as was earlier done by Ref. [133]. However, after the onset of the antikaon condensation, electrons and muons are replaced by K^- mesons and proton fraction increases rapidly in the system [135, 136]. In this situation protons can not be treated as passive scatterers.

6.2.3 Strong interaction

Next we focus on the calculation of collision frequencies of neutron-neutron, proton-proton and neutron-proton scatterings due to the strong interaction. The knowledge of nucleon-nucleon scattering cross sections are exploited in this calculation. This was first done by Ref. [130]. Later recent developments in the calculation of nucleon-nucleon scattering cross sections in the Dirac-Brueckner approach were considered for this purpose [140,142]. Here we adopt the same prescription of Ref. [142] for the calculation of collision frequencies due to nucleon-nucleon scatterings. The collision frequency for the scattering of identical particles under strong interaction is given by

$$\nu_{ii} + \nu'_{ii} = \frac{16 m_i^{*3} (k_B T)^2}{3 m_n^2} S_{ii} \,, \tag{6.20}$$

$$S_{ii} = \frac{m_n^2}{16\pi^2} \int_0^1 dx' \int_0^{\sqrt{(1-x'^2)}} dx \frac{12x^2 x'^2}{\sqrt{1-x^2-x'^2}} \mathcal{Q}_{ii} \,, \tag{6.21}$$

where $i = n, p$ and m_n is the bare nucleon mass and $\mathcal{Q}_{ii}$ is the matrix element squared which appears in Eq. (6.10). Similarly we can write the collision frequency for nonidentical particles as [137]

$$\begin{aligned} \nu_{ij} &= \frac{32 m_i^* m_j^{*2} (k_B T)^2}{3 m_n^2} S_{ij} \,, \\ \nu'_{ij} &= \frac{32 m_i^{*2} m_j^* (k_B T)^2}{3 m_n^2} S'_{ij} \,, \end{aligned} \tag{6.22}$$

and

$$\begin{aligned} S_{ij} &= \frac{m_n^2}{16\pi^2} \int_{0.5-x_0}^{0.5+x_0} dx' \int_0^f dx \frac{6(x^2 - x^4)}{\sqrt{(f^2 - x^2)}} \mathcal{Q}_{ij} \,, \\ S'_{ij} &= \frac{m_n^2}{16\pi^2} \int_{0.5-x_0}^{0.5+x_0} dx' \int_0^f dx \frac{[6x^4 + 12x^2 x'^2 - (3 + 12x_0^2) x^2]}{\sqrt{(f^2 - x^2)}} \mathcal{Q}_{ij} \,. \end{aligned} \tag{6.23}$$

We define $x_0 = \frac{k_{f_j}}{2k_{f_i}}$, $x = \frac{\hbar q}{2k_{f_i}}$, $x' = \frac{q'}{2k_{f_i}}$, $f = \frac{\sqrt{x_0^2 - (0.25 + x_0^2 - x'^2)^2}}{x'}$, where momentum transfers $\mathbf{q} = \mathbf{k}_{j'} - \mathbf{k}_j$ and $\mathbf{q}' = \mathbf{k}_{j'} - \mathbf{k}_i$. We find that the calculation of S_{ij}, S_{ii} and S'_{ij} requires the knowledge of $\mathcal{Q}_{ii}$ and $\mathcal{Q}_{ij}$. The matrix elements squared are extracted from the in-vacuum nucleon-nucleon differential scattering cross sections computed using Dirac-Brueckner approach [143] from the following relations [133, 142].

$$\begin{aligned} \frac{d\sigma_{ij}}{d\Omega_{CM}}(\epsilon_{Lab}, \theta_{CM}) &= \frac{m_N^2}{16\pi^2} \mathcal{Q}_{ij} \,, \\ \cos\theta_{CM} &= \frac{q'^2 - q^2}{q'^2 + q^2} \,, \\ \epsilon_{Lab} &= \frac{q^2 + q'^2}{2m_N} \end{aligned} \tag{6.24}$$

where θ_{CM} is the scattering angle measured in the center of mass frame while ϵ_{Lab} is the total energy of the interacting particles in the laboratory frame. It is to be noted here that S_{pp}, S_{pn} and S'_{ij} are the new results of this calculation. As soon as we know the collision frequencies of nucleon-nucleon scatterings due to the strong interaction, we can immediately calculate effective relaxation times of neutrons and protons from Eq. (6.14). This leads to the calculation of the neutron and proton shear viscosities as

$$\eta_n = \frac{n_n k_{f_n}^2 \tau_n}{5m_n^*} \,,$$
$$\eta_p = \frac{n_p k_{f_p}^2 \tau_p}{5m_p^*} \,. \tag{6.25}$$

Finally the total shear viscosity is given by

$$\eta_{total} = \eta_n + \eta_p + \eta_e + \eta_\mu \,. \tag{6.26}$$

6.2.4 Calculation of the EOS

The EOS enters into the calculation of the shear viscosity as an input. We construct the EOS within the framework of the RMF model described in Chapter 5. Here we consider a first order phase transition from nuclear matter to K^- condensed matter. We adopt the Maxwell construction for the first order phase transition. The constituents of matter are neutrons, protons, electrons and muons in both phases and also (anti)kaons in the K^- condensed phase. Both phases maintain charge neutrality and β equilibrium conditions. The detail calculations of both these phases have already been presented in Chapter 5 and we use them here to get the effective nucleon mass and Fermi momenta of particles at different baryon densities. For the coupling constants we take GM1 [119] parameter set given in table 5.1. The K^- optical potential we choose is $U_K = -160$ MeV, which gives a kaon-sigma meson coupling constants $g_{\sigma K} = 2.9937$ (see table 5.2). This choice of U_K is motivated from the findings of the analysis of K^- atomic data.

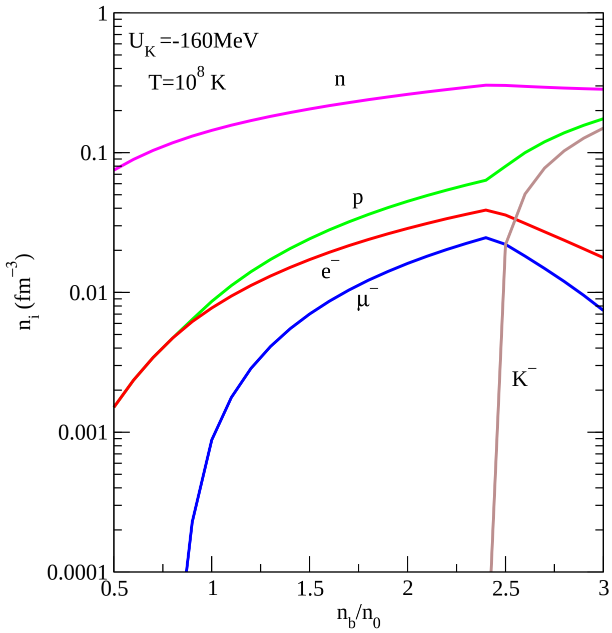

Figure 6.1: Number densities of different particle species as a function of normalized baryon density

6.3 Results and Discussions

The composition of neutron star matter including the K^- condensate as a function of normalized baryon density is shown in Fig. 6.1 The K^- condensation sets in at $2.43n_0$. Before the onset of the condensation, all particle fractions increase with baryon density. In this case, the charge neutrality is maintained by protons, electrons and muons. As soon as the K^- condensate is formed, the density of K^- mesons in the condensate rapidly increases and K^- mesons replace leptons in the system. The proton density eventually becomes equal to the K^- density. The proton density in the presence of the condensate increases significantly and may be higher than the neutron density at higher baryon densities [144]. This increase in the proton fraction in the presence of the K^- condensate might result in an enhancement in the proton shear viscosity and appreciable reduction in the electron and muon viscosities compared with the case without the condensate. We discuss this in detail in the following paragraphs.

Next we focus on the calculation of ν_{ii}, ν_{ij} and ν'_{ij}. For the scatterings via the electro-

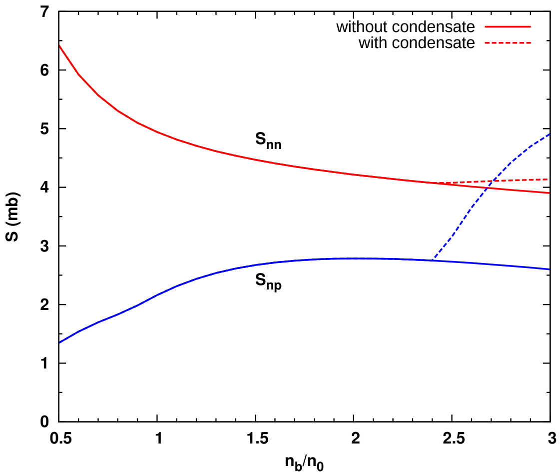

Figure 6.2: S_{nn} and S_{np} as a function of normalized baryon density

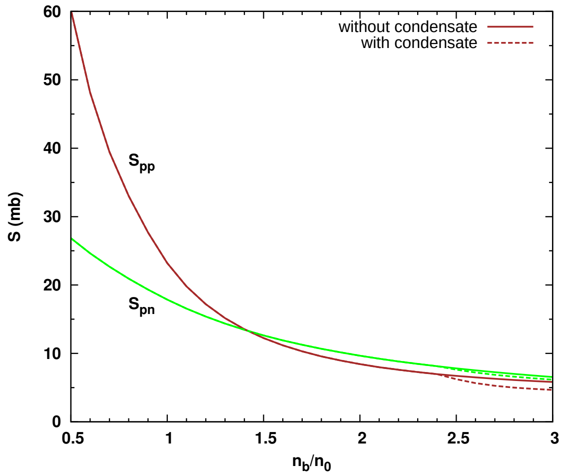

Figure 6.3: S_{pp} and S_{pn} as a function of normalized baryon density

magnetic interaction, we calculate those quantities using Eqs. (6.17) and (6.18). On the other hand, νs corresponding to collisions through the strong interaction are estimated using Eqs. (6.20)-(6.23). In an earlier calculation, the authors considered only S_{nn} and S_{np} [133] for the calculation of the neutron shear viscosity in nucleons-only neutron star matter because protons were treated as passive scatterers. It follows from the discussion in the preceding paragraph that protons can no longer be treated as passive scatterers because of the large proton fraction in the presence of the K^- condensate. Consequently the contributions of S_{pp} and S_{pn} have to be taken into account in the calculation of the proton and neutron shear viscosities. The expressions of S_{nn}, S_{pp}, S_{np} and S_{pn} given by Eqs. (6.21) and (6.23) involve matrix elements squared. We note that there is an one to one correspondence between the differential cross section and the matrix element squared [142]. We exploit the in-vacuum nucleon-nucleon cross sections of Li and Machleidt [143] calculated using Bonn interaction in the Dirac-Brueckner approach for the calculation of matrix elements squared. We fit the neutron-proton as well as proton-proton differential cross sections and use them in Eqs. (6.21) and (6.23) to calculate S_{nn}, S_{pp}, S_{np} and S_{pn} which are functions of neutron (k_{f_n}) and proton (k_{f_p}) Fermi momenta. The values of k_{f_n} ranges from 1.3 to 2.03 fm^{-1} whereas that of k_{f_p} spans the interval 0.35

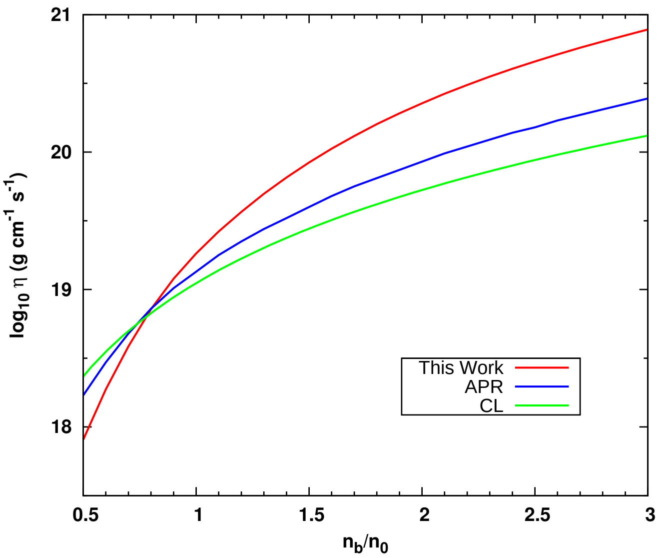

Figure 6.4: The shear viscosities in nuclear matter without the K^- condensate corresponding to this work, the parametrization of Cutler and Lindblom [131] and the EOS of APR [110] as a function of normalized baryon density at a temperature $T = 10^8$ K.

to 1.73 fm^{-1}. This corresponds to the density range ∼0.5 to $\sim 3.0n_0$. We fit the results of our calculation.

Figures 6.2 and 6.3 display the variation of S_{nn}, S_{pp}, S_{np} and S_{pn} with baryon density. The value of S_{nn} is greater than that of S_{np} in the absence of the condensate as evident from Fig. 6.2. Our results agree well with those of Ref. [133]. However, S_{np} rises rapidly with baryon density after the onset of the K^- condensation and becomes higher than S_{nn}. It is noted that the effect of the condensate on S_{nn} is not significant. Figure 6.3 shows that S_{pp} drops sharply with increasing baryon density and crosses the curve of S_{pn} in the absence of the condensate. However S_{pp} and S_{pn} are not influenced by the K^- condensate. A comparison of Fig. 6.2 and Fig. 6.3 reveals that S_{pp} is almost one order of magnitude larger than S_{nn} at lower baryon densities. This may be attributed to the smaller proton Fermi momentum. We also compute S'_{np} and S'_{pn} (not shown here) and these quantities have comparatively smaller values. Further we find that the magnitude of S'_{pn} is higher than that of S'_{np}.

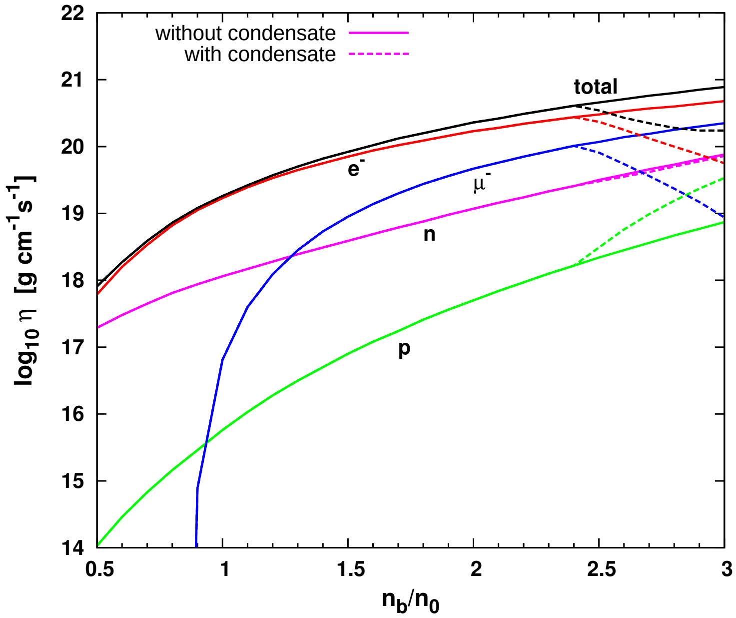

Figure 6.5: The total shear viscosity as well as shear viscosities corresponding to different particle species as a function of normalized baryon density at a temperature $T = 10^8$ K with (solid line) and without (dashed line) a K^- condensate.

As soon as we know νs, we can calculate effective relaxation times using Eq. (6.14) and shear viscosities using Eqs. (6.19), (6.25) and (6.26). First, we discuss the total shear viscosity in nuclear matter without a K^- condensate. This is shown as a function of baryon density at a temperature 10^8K in Fig. 6.4. Here our results indicated by the red line are compared with the calculation of the total shear viscosity using the EOS of Akmal, Pandharipande and Ravenhall (APR) [110] denoted by the blue line and also with the results of Flowers and Itoh [129, 130]. For the APR case, we exploit the parametrization of the EOS by Heiselberg and Hjorth-Jensen [145]. Further we take density independent nucleon effective masses $m_n^* = m_p^* = 0.8m_n$ for the calculation with the APR EOS which was earlier discussed by Shternin and Yakovlev [140]. On the other hand, the results of Flowers and Itoh were parametrized by Cutler and Lindblom (CL) [131] and it is shown by the green line in Fig. 6.4. It is evident from Fig. 6.4 that the total shear viscosity in our calculation is significantly higher than other cases. This may be attributed to the fact that our EOS is a fully relativistic one.

We exhibit shear viscosities in presence of the K^- condensate as a function of baryon density in Fig. 6.5. This calculation is performed at a temperature 10^8K. In the absence of the K^- condensate, the contribution of the electron shear viscosity to the total shear viscosity is the highest. The electron, muon and neutron shear viscosities exceed the proton shear viscosity by several orders of magnitude. Further we note that the lepton viscosities are greater than the neutron viscosity. On the other hand, we find interesting results in presence of the K^- condensate. The electron and muon shear viscosities decrease very fast after the onset of K^- condensation whereas the proton shear viscosity rises in this case. There is almost no change in the neutron shear viscosity. It is interesting to note that the proton shear viscosity in presence of the condensate approaches the value of the neutron shear viscosity as baryon density increases. The total shear viscosity decreases in the K^- condensed matter due to the sharp drop in the lepton shear viscosities. Here the variation of shear viscosities with baryon density is shown up to $3n_0$. The neutron and proton shear viscosities in neutron star matter with the K^- condensate might dominate over the electron and muon shear viscosities beyond baryon density $3n_0$. Consequently, the total shear viscosity would again increase.

The temperature dependence of the total shear viscosity is shown in Fig. 6.6. In an earlier calculation, electron and muon shear viscosities were determined by collisions only due to the exchange of transverse plasmons because this was the dominant contribution [140]. Under this approximation, the electron and muon shear viscosities had a temperature dependence of $T^{-5/3}$, whereas, the neutron shear viscosity was proportional to T^{-2}. The temperature dependence of the electron and muon shear viscosities deviated from the standard temperature dependence of the shear viscosity of neutron Fermi liquid. However, in this calculation we have not made any such approximation. We have considered all the components of effective collision frequency which have different temperature dependence as given by Eq. (6.18). This gives rise to a complicated temperature depen-

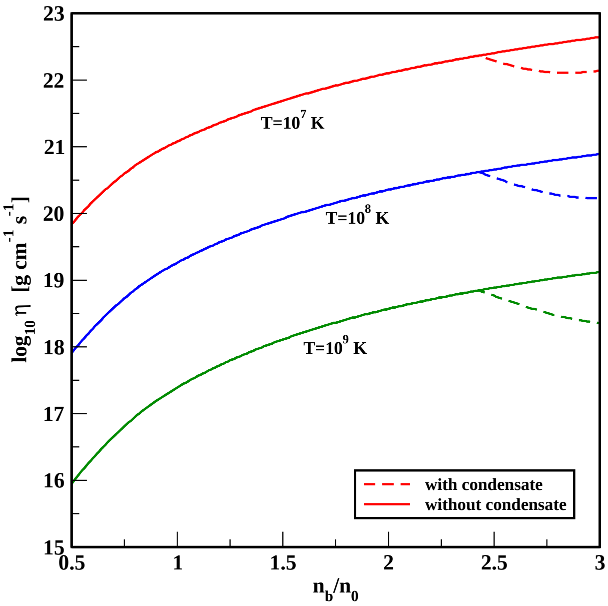

Figure 6.6: The total shear viscosity as a function of normalized baryon density at different temperature with (solid line) and without (dashed line) the K^- condensate.

dence in the calculation of shear viscosity. The total shear viscosity is plotted for $T = 10^7$, 10^8, and 10^9 K in Fig. 6.6. It is noted that the shear viscosity increases as temperature decreases.

The shear viscosity plays an important role in damping the r-mode instability in old and accreting neutron stars [146,147]. The suppression of the instability is achieved by the competition of various time scales associated with gravitational radiation (τ_{GR}), hyperon bulk viscosity (τ_B), modified Urca bulk viscosity (τ_U), and shear viscosity (τ_{SV}). At high temperatures the bulk viscosity damp the r-mode instability. As neutron stars cool down, the bulk viscosity might not be the dominant damping mechanism. The shear viscosity becomes significant in the temperature regime $\leq 10^8$ K and might suppress the r-mode instability effectively.

In this calculation, we consider only the K^- optical potential depth $U_K = -160$ MeV. However, this calculation could be performed for other values of U_Ks. As the magnitude of the K^- potential depth decreases, the threshold of the K^- condensation is shifted to higher densities [135]. On the other hand, hyperons may also appear in neutron star matter around 2-3n_0. Negatively charged hyperons might delay the onset of the K^- condensation [114, 148, 149]. However, it was noted in an earlier calculation that Σ^- hyperons were excluded from the system because of repulsive Σ-nuclear matter interaction and Ξ^- hyperons might appear at very high baryon density [136]. However, the appearance of Λ hyperons could compete with the threshold of K^- condensation. If Λ hyperons appear before K^- condensation, the threshold of K^- condensation is shifted to higher baryon density because of softening in the equation of state due to Λ hyperons. But the qualitative results of the shear viscosity discussed above remain the same.

6.4 Summary and Conclusions

We have investigated the shear viscosity in presence of a K^- condensate in this chapter. With the onset of K^- condensation, electrons and muons are replaced by K^- mesons rapidly. The proton fraction also increases and eventually becomes equal to the neutron fraction in the K^- condensed neutron star matter. This has important consequences for the electron, muon and proton shear viscosities. We have found that the electron and muon shear viscosities drop steeply after the formation of the K^- condensate in neutron stars. On the other hand, the proton shear viscosity whose contribution to the total shear viscosity was negligible in earlier calculations [130, 133], now becomes significant in presence of the K^- condensate. The proton shear viscosity would exceed the neutron as well as lepton shear viscosities beyond $3n_0$. The total viscosity would be dominated by the proton and neutron shear viscosities in this case. This calculation may be extended to neutron stars with strong magnetic fields.

It is worth mentioning here that we adopt the Maxwell construction for the first order phase transition in this calculation. Such a construction is justified if the surface tension between two phases is quite large [150]. Moreover the value of the surface tension between the nuclear and the K^- condensed phases or between the hadron and quark phases is not known correctly. Therefore, this problem could also be studied using the Gibbs construction [151].

Besides the role of shear viscosity in damping the r-mode instability as well as in pulsar glitches and free precession of neutron stars, it has an important contribution in the nucleation rate of bubbles in first order phase transitions. It was shown earlier that the shear viscosity might control the initial growth rate of a bubble [152, 153]. This will be studied in the next chapter in connection with the K^- condensation in neutron stars.

Chapter 7

Thermal nucleation in protoneutron stars

7.1 Introduction

A first order phase transition from nuclear matter to some exotic form of matter might be possible in protoneutron stars. It could be either a nuclear to quark matter transition or a first order pion/kaon condensation. Consequently, it might have tremendous implications for compact stars [105] and supernova explosions [154]. Here the focus is the first order phase transition proceeding through the thermal nucleation of a new phase in particular, the K^- condensed phase in hot and neutrino-trapped matter. After the pioneering work of Kaplan and Nelson on the kaon condensation in dense baryonic matter formed in heavy ion collisions as well as in neutron stars [115], several groups pursued the problem of the K^- condensation in (proto)neutron stars [114, 118, 135, 148, 149, 155–162]. In most cases, the phase transition was studied using either Maxwell construction or Gibbs rules for phase equilibrium coupled with global baryon number and charge conservation [151]. The first order phase transition driven by the nucleation of K^- condensed phase was considered in a few cases [163, 164]. In particular, the calculation of Ref. [164] dealt with the role of shear viscosity on the thermal nucleation of antikaon condensed phase in hot and neutrino-free compact stars. It is to be noted here that the first order phase transition through the thermal nucleation of quark matter droplets was also investigated in (proto)neutron stars [153, 163, 165–169] using the homogeneous nucleation theory of Langer [56, 163, 165]. The thermal nucleation is an efficient process than the quantum nucleation at high temperatures [153, 169].

We adopt the homogeneous nucleation theory of Langer [56, 170] for the thermal nucleation of the K^- condensed phase. Nuclear matter would be metastable near the phase transition point due to sudden change in state variables. In this respect thermal and quantum fluctuations are important. Droplets of K^- condensed matter are formed because of thermal fluctuations in the metastable nuclear matter. Droplets of the new and stable phase which are bigger than a critical radius, will survive and grow. The transportation of latent heat from the surface of the droplet into the metastable phase favours a critical size droplet to grow further. This heat transportation could be achieved through the thermal dissipation and viscous damping [152, 170, 173].

A parametrized form of the shear viscosity was used in earlier calculations of the nucleation of quark matter [153]. Recently, the influence of thermal conductivity and shear viscosity on the thermal nucleation time was studied in a first-order phase transition from the nuclear matter to the K^- condensed matter in hot neutron stars [164]. The shear viscosity due to neutrinos was not considered in that calculation. Here we study the effect of shear viscosity on the thermal nucleation rate of droplets of the K^- condensed matter in neutrino-trapped matter relevant to protoneutron stars [171,172]. Besides shear viscosities due to neutrons, protons and electrons, this involves the contribution of neutrinos to the total shear viscosity.

We organize the paper in the following way. We describe shear viscosities of different species including neutrinos, models for the EOS, and the calculation of thermal nucleation rate in Sec. 7.2. Results of this calculation are discussed in Sec. 7.3 . Section 7.4 gives the summary and conclusions.

7.2 Formalism

It was noted in the last chapter that the main contributions to the total shear viscosity in neutron star matter came from electrons, the lightest charged particles, and neutrons, the most abundant particles. Neutrinos are trapped in protoneutron stars and their contribution might be significant in transport coefficients such as shear viscosity. In principle, we may calculate shear viscosities for different particle species (n, p, e and ν_e) in neutrino-trapped matter using coupled Boltzmann transport equations of the form of Eq. (6.1) from which we can immediately write a set of relations between effective relaxation times (τ) and collision frequencies ($\nu_{ij}, \nu^{'}_{ij}$) as

$$\sum_{i,j=n,p,e,\nu_e} (\nu_{ij}\tau_i + \nu'_{ij}\tau_j) = 1\,, \tag{7.1}$$

which can be cast into a matrix equation similar to Eq. (6.11). However, solving the matrix equation becomes a problem because the relaxation time for neutrinos (calculated below) is much larger than those of other species as it is evident from Fig. 7.1. So we calculate the relaxation times of neutrons, protons and electrons in neutrino-trapped matter from the above matrix equation as was done in the previous chapter.

7.2.1 Neutrino shear viscosity

To calculate the neutrino shear viscosity we follow the prescription of Goodwin and Pethick [174] and get the following expression

$$\eta_\nu = \frac{1}{5} n_\nu k_{f_\nu} c\tau_\nu \left[\frac{\pi^2}{12} + \lambda_\eta \sum_{m=odd} \frac{2(2m+1)}{m^2(m+1)^2[m(m+1)-2\lambda_\eta]}\right]. \tag{7.2}$$

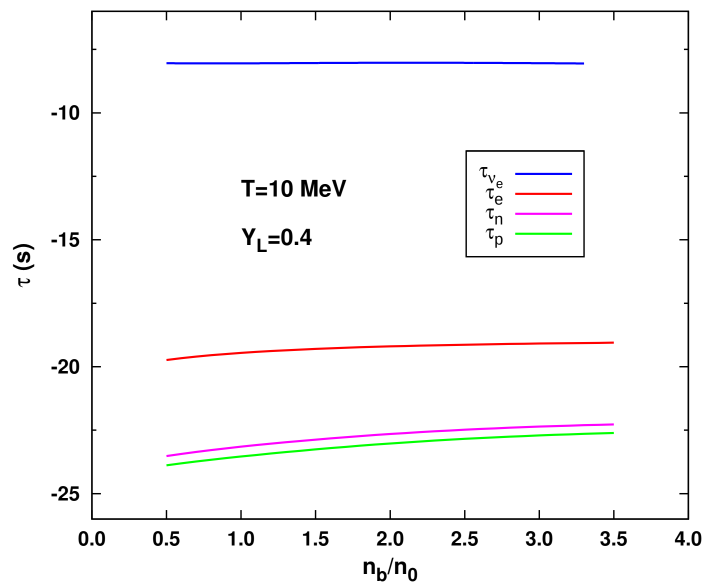

Figure 7.1: Relaxation times corresponding to different species in neutrino-trapped nuclear matter as a function of normalized baryon density at a temperature $T = 10$ MeV and $Y_L = 0.4$.

For neutrino shear viscosity, we only consider scattering processes involving neutrinos and other species. Various quantities in Eq.(7.2) are explained below. The neutrino relaxation time (τ_ν) is,

$$\tau_\nu^{-1} = \sum_{i=n,p,e} \tau_{\nu i}^{-1}, \quad , \tag{7.3}$$

$$\tau_{\nu i}^{-1} = \frac{E_{f_i}^2 (k_B T)^2}{64\pi^2} < I^i > \quad , \tag{7.4}$$

and λ_η is defined as

$$\lambda_\eta = \tau_\nu \sum_i \lambda_\eta^i \tau_{\nu i}^{-1} \tag{7.5}$$

$$\lambda_\eta^i = \frac{\int d\Omega_2 d\Omega_3 d\Omega_4 \, \frac{1}{2} \left[3(\hat{\mathbf{k}_1} \cdot \hat{\mathbf{k}_3})^2 - 1 \right] \langle |M|^2 \rangle_i \, \delta(\mathbf{k}_1 + \mathbf{k}_2 - \mathbf{k}_3 - \mathbf{k}_4)}{\int d\Omega_2 d\Omega_3 d\Omega_4 \, \langle |M|^2 \rangle_i \, \delta(\mathbf{k}_1 + \mathbf{k}_2 - \mathbf{k}_3 - \mathbf{k}_4)} \tag{7.6}$$

$$= 1 - \frac{3}{2k_{f_\nu}^2} \frac{I_1^i}{< I^i >} + \frac{3}{8k_{f_\nu}^4} \frac{I_2^i}{< I^i >} \, , \tag{7.7}$$

$$
\begin{aligned}
< I^i > &= \frac{8G_F^2\pi k_{f_\nu}}{3}\left[4C_{V_i}C_{A_i}\left(\frac{k_{f_\nu}}{E_{f_i}}\right)+(C_{V_i}^2+C_{A_i}^2)\left\{3+\left(\frac{k_{f_i}}{E_{f_i}}\right)^2+\frac{2}{5}\left(\frac{k_{f_\nu}}{E_{f_i}}\right)^2\right\}\right.\\
&\left.-\left(\frac{m_i}{E_{f_i}}\right)^2(C_{V_i}^2-C_{A_i}^2)\right] \qquad (7.8)\\
I_1^i &= \frac{32G_F^2\pi k_{f_\nu}^3}{15}\left[12C_{V_i}C_{A_i}\left(\frac{k_{f_\nu}}{E_{f_i}}\right)+(C_{V_i}^2+C_{A_i}^2)\left\{5+\left(\frac{k_{f_i}}{E_{f_i}}\right)^2+\frac{12}{7}\left(\frac{k_{f_\nu}}{E_{f_i}}\right)^2\right\}\right.\\
&\left.-3\left(\frac{m_i}{E_{f_i}}\right)^2(C_{V_i}^2-C_{A_i}^2)\right] \qquad (7.9)\\
I_2^i &= \frac{128G_F^2\pi k_{f_\nu}^5}{35}\left[20C_{V_i}C_{A_i}\left(\frac{k_{f_\nu}}{E_{f_i}}\right)+(C_{V_i}^2+C_{A_i}^2)\left\{7+\left(\frac{k_{f_i}}{E_{f_i}}\right)^2+\frac{10}{3}\left(\frac{k_{f_\nu}}{E_{f_i}}\right)^2\right\}\right.\\
&\left.-5\left(\frac{m_i}{E_{f_i}}\right)^2(C_{V_i}^2-C_{A_i}^2)\right]. \qquad (7.10)
\end{aligned}
$$

Here $< |M^2| >$ is the squared matrix element summed over final spins and averaged over initial spins for a scattering process and C_V and C_A are vector and axial-vector coupling constants.

For non-relativistic nucleons $(m_i/E_{f_i}) \simeq 1$, $(k_{f_i}/E_{f_i}) \ll 1$ and if also $(k_{f_\nu}/E_{f_i}) \ll 1$, λ_η^i reduces to [174]

$$\lambda_\eta^i = \frac{\frac{11}{35}C_{V_i}^2+\frac{2}{7}C_{A_i}^2}{C_{V_i}^2+2C_{A_i}^2} \qquad (7.11)$$

However, we do not assume non-relativistic approximation in this calculation. The total shear viscosity is given by

$$\eta_{total} = \eta_n + \eta_p + \eta_e + \eta_\nu \ , \qquad (7.12)$$

with

$$\eta_{i(=n,p,e)} = \frac{n_i k_{f_i}^2 \tau_i}{5m_i^*} \ . \qquad (7.13)$$

where m_i and k_{f_i} denote the effective mass and Fermi momentum respectively, of i-th species. The relaxation times (τ_i) are calculated using the method described in the previous chapter and are given by

$$
\begin{aligned}
\tau_n &= \left[\left(\nu_p\nu_e - \nu'_{pe}\nu'_{ep}\right) - \nu'_{np}\left(\nu'_{pe} - \nu_e\right)\right]/D\,, \\
\tau_p &= \left[\nu_n\left(\nu_e - \nu'_{pe}\right) - \nu'_{pn}\nu_e\right]/D\,, \\
\tau_e &= \left[\nu_n\left(\nu_p - \nu'_{ep}\right) - \nu'_{pn}\left(\nu'_{np} - \nu'_{ep}\right)\right]/D\,,
\end{aligned}
\tag{7.14}
$$

where $D = \nu_n(\nu_p\nu_e - \nu'_{pe}\nu'_{ep}) - \nu'_{pn}\nu_e$. Collision frequencies appearing in Eq. (7.14) are obtained from Eqs. (6.12), (6.13), (6.17)-(6.18) and (6.20)-(6.22).

7.2.2 The EOS

The knowledge of the EOS for the nuclear as well as the K^- condensed phases is essential for the computation of shear viscosity and thermal nucleation rate. As discussed in earlier chapters we consider here a first-order phase transition from the charge neutral and β-equilibrated ($\mu_e + \mu_p = \mu_n + \mu_{\nu_e}$) nuclear matter to the K^- condensed matter in a protoneutron star. Those two phases are composed of neutrons, protons, electrons, electron type neutrinos and of K^- mesons only in the K^- condensed phase. Both phases are governed by baryon number conservation and charge neutrality conditions. The critical droplet of the K^- condensed matter is in total phase equilibrium with the metastable nuclear matter. The mixed phase is governed by Gibbs phase rules along with global baryon number conservation and charge neutrality (Sec. 5.2.3). We adopt the bulk approximation [165] which does not consider the variation of the meson fields with position inside the droplet. Relativistic field theoretical models described in Chapter 5 are employed to calculate the EOS in nuclear and antikaon condensed phases. Expressions for the energy density and pressures in the nuclear matter and the K^- condensed matter are given in Secs.(5.2.1), (5.2.2). As we are interested in neutrino-trapped matter of protoneutron stars, we have to add the contributions of neutrinos in Eqs. (5.26) and (5.27) given by

$$
\epsilon_{\nu_e} = \frac{k_{f_{\nu_e}}}{8\pi^2}\,, \qquad P_{\nu_e} = \frac{k_{f_{\nu_e}}}{24\pi^2}\,. \tag{7.15}
$$

Here we use the zero temperature EOSs because it was noted earlier that the temperature of a few tens of MeV did not modify the EOS considerably [164].

7.2.3 Nucleation rate

We are interested in a first order phase transition driven by the nucleation of droplets of antikaon condensed phase in the neutrino-trapped nuclear matter. Droplets of antikaon condensed phase are born in the metastable nuclear matter due to thermal fluctuations. Droplets of antikaon condensed matter above a critical size (R_c) will grow and drive the phase transition. According to the homogeneous nucleation formalism of Langer and others, the thermal nucleation per unit time per unit volume is given by [56, 170]

$$\Gamma = \Gamma_0 exp \left(-\frac{\triangle F(R_c)}{T} \right) \ , \tag{7.16}$$

where $\triangle F$ is the free energy cost to produce a droplet with a critical size in the metastable nuclear matter. The free energy shift of the system as a result of the formation of a droplet is given by [167, 168]

$$\triangle F(R) = -\frac{4\pi}{3}(P^K - P^N)R^3 + 4\pi\sigma R^2 \ , \tag{7.17}$$

where R is the radius of the droplet, σ is surface tension of the interface separating two phases and P^N and P^K are the pressures in the neutrino-trapped nuclear and the K^- condensed phases, respectively as discussed above. We obtain the critical radius of the droplet from the maximum of $\triangle F(R)$ i.e. $\delta_R \triangle F = 0$,

$$R_C = \frac{2\sigma}{(P^K - P^N)} \ . \tag{7.18}$$

This relation also demonstrates the mechanical equilibrium between two phases.

We write the prefactor in Eq. (7.16) as the product of two parts - statistical and dynamical prefactors [152, 170, 173]

$$\Gamma_0 = \frac{\kappa}{2\pi}\Omega_0 \ . \tag{7.19}$$

The available phase space around the saddle point at R_C during the passage of the droplet through it is given by the statistical prefactor (Ω_0),

$$\Omega_0 = \frac{2}{3\sqrt{3}}\left(\frac{\sigma}{T}\right)^{3/2}\left(\frac{R_C}{\xi}\right)^4 \ , \tag{7.20}$$

Here ξ is the kaon correlation length which is considered to be the width of the interface between nuclear and antikaon condensed matter. The dynamical prefactor κ is responsible for the initial exponential growth rate of a critical droplet and given by [152, 173]

$$\kappa = \frac{2\sigma}{R_C^3(\triangle w)^2}\left[\lambda T + 2\left(\frac{4}{3}\eta + \zeta\right)\right] \ . \tag{7.21}$$

Here $\triangle w = w_K - w_N$ is the enthalpy difference between two phases, λ is the thermal conductivity and η and ζ are the shear and bulk viscosities of neutrino-trapped nuclear matter. We neglect the contribution of thermal conductivity because it is smaller compared with that of shear viscosity [164]. We also do not consider the contribution of bulk viscosity in the prefactor in this calculation.

We can now calculate the thermal nucleation time (τ_{nuc}) in the interior of neutron stars as

$$\tau_{nuc} = (V\Gamma)^{-1} \ , \tag{7.22}$$

where the volume $V = 4\pi/3R_{nuc}^3$. We assume that pressure and temperature are constant within this volume in the core.

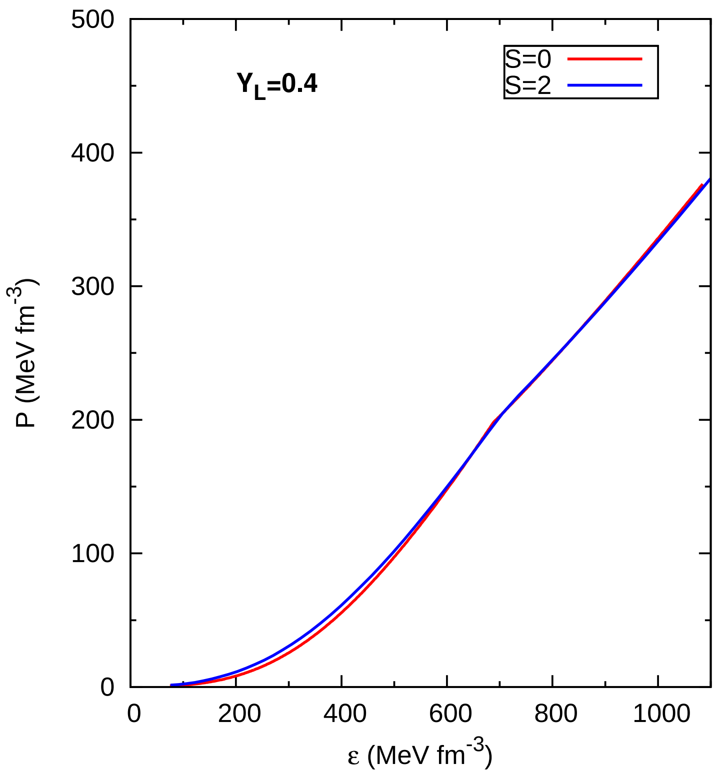

Figure 7.2: Comparison of EOSs corresponding to entropy density $S = 0$ and $S = 2$ for $Y_L = 0.4$.

7.3 Results and Discussion

Like the previous chapter here also we use the GM1 parameter set (table 5.1) for nucleon-meson coupling constants. Procedure to get the kaon-meson coupling constants is discussed in Sec. 5.3.2. Here we consider an optical potential depth of $U_K(n_0) = -120$ MeV at normal nuclear matter density and the corresponding kaon-scalar meson coupling constant is $g_{\sigma K} = 1.6337$ (table 5.2). The value of K^- optical potential adopted in this calculation resulted in a maximum neutron star mass of 2.08 $M_\odot$ in earlier calculations using the Maxwell construction [135]. This is consistent with the recently observed $2M_\odot$ neutron star [6].

Fig. 7.2 shows EOSs of neutrino-trapped matter ($Y_L = 0.4$) for entropy density $S = 0$ and $S = 2$. It is evident from the figure that thermal effects can't change the EOS

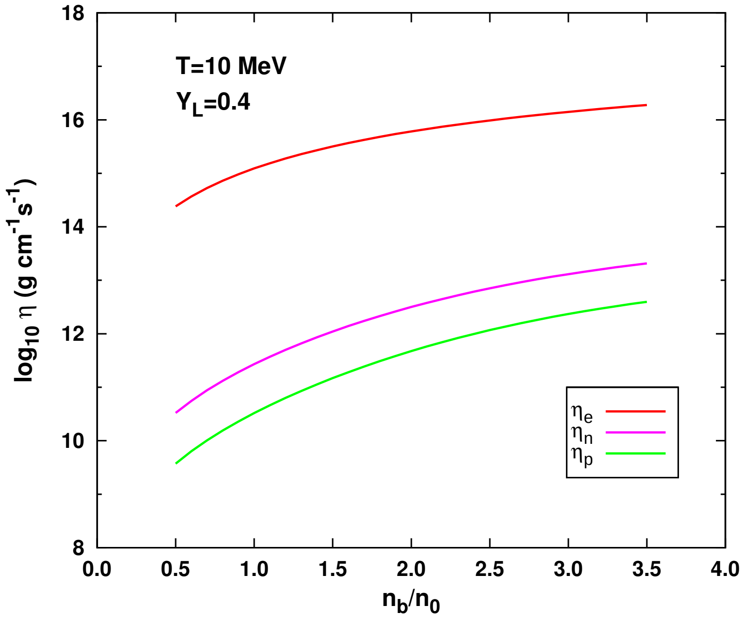

Figure 7.3: Shear viscosities corresponding to different particle species in neutrino-trapped nuclear matter as a function of the normalized baryon density at a temperature $T = 10$ MeV and $Y_L = 0.4$.

appreciably. Therefore, we use the EOS of neutrino-trapped nuclear and K^- condensed phases at zero temperature. In this calculation, the EOS enters in Eq. (7.17) as the difference between pressures in two phases and in Eq. (7.21) as the enthalpy difference between two phases. Here we exploit the zero temperature EOS for the the calculation of shear viscosity and thermal nucleation time. The thermal nucleation of exotic phases was earlier investigated using zero temperature EOS in Ref. [164, 168].

First we calculate shear viscosities of neutrons, protons and electrons in neutrino-trapped nuclear matter using Eq. (7.13) in the same fashion as it was done in the last chapter. We take lepton fraction $Y_L = 0.4$ in this calculation. Shear viscosities of different species are shown as a function of normalized baryon density at a temperature T=10 MeV in Fig. 7.3. Here the electron viscosity is higher than the neutron and proton shear viscosities. The total shear viscosity excluding the viscosity due to neutrinos in neutrino-trapped nuclear matter is shown as a function of normalized baryon density for

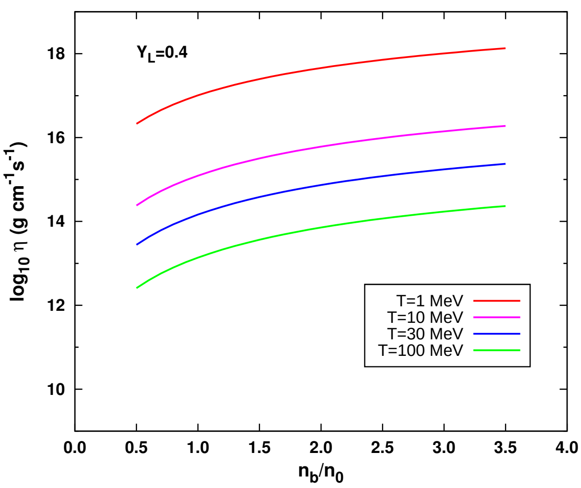

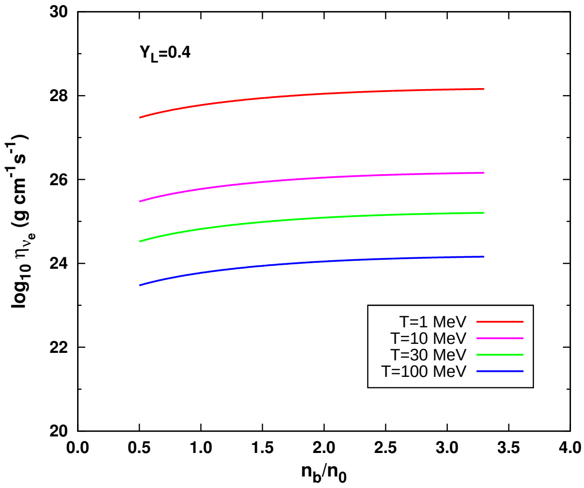

Figure 7.4: Total shear viscosity in neutrino-trapped nuclear matter except the neutrino contribution as a function of normalized baryon density for different temperatures

Figure 7.5: Shear viscosity owing to only neutrinos is shown as a function of normalized baryon density and at different values of the temperature.

temperatures $T = 1$, 10, 30 and 100 MeV in Fig. 7.4. The shear viscosity is found to increase with baryon density. Furthermore, the shear viscosity decreases with increasing temperature. It is observed that the shear viscosities of neutrons, protons and electrons in neutrino-trapped nuclear matter are of the same orders of magnitude as those of the neutrino-free case presented in the last chapter.

Next we calculate the shear viscosity due to neutrinos. As a prelude to it, we compare effective relaxation times corresponding to different species in neutrino-trapped nuclear matter in Fig. 7.1. Relaxation time is plotted with normalized baryon density at a temperature T=10 MeV in Fig. 7.1. Relaxation times of different particle species owing to scattering under strong and electromagnetic interactions are much much shorter than that of neutrinos undergoing scattering with other species through weak interactions. Consequently, particles excluding neutrinos come into thermal equilibrium quickly on the time scale of weak interactions. We calculate the shear viscosity due to neutrinos only treating others as background and it is shown as a function of normalized baryon density for temperatures $T = 1$, 10, 30 and 100 in Fig. 7.5. Like Fig. 7.4, the neutrino shear

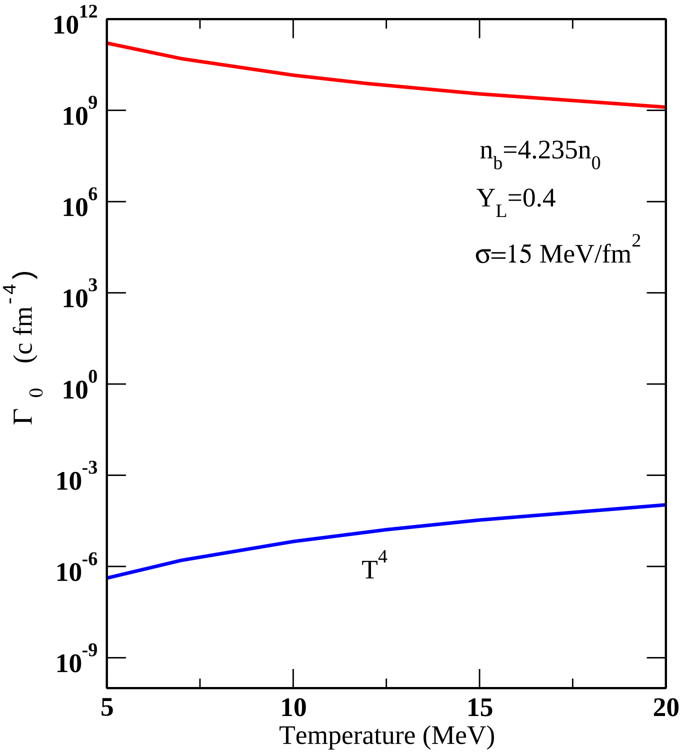

Figure 7.6: Prefactor including the contribution of shear viscosity as a function of temperature at a fixed baryon density and surface tension and compared with that of the T^4 approximation.

viscosity decreases with increasing temperature. However, the neutrino shear viscosity is several orders of magnitude larger than shear viscosities of neutrons, protons and electrons shown in Fig. 7.4. It is the neutrino shear viscosity which dominates the total viscosity of Eq. (7.12) in neutrino-trapped matter. We perform the rest of our calculation using the neutrino viscosity in the following paragraphs.

We calculate the prefactor (Γ_0) according to Eqs. (7.19)-(7.21). The dynamical prefactor not only depends on the shear viscosity but also on the thermal conductivity and bulk viscosity. However, it was already noted that the thermal conductivity and bulk viscosity in neutrino-trapped nuclear matter were negligible compared with the shear viscosity [174]. We only consider the effect of shear viscosity on the prefactor. Besides transport coefficients, the prefactor in particular, the statistical prefactor is sensitive to the correlation length of kaons and surface tension. The correlation length is the thickness of the interface between nuclear and kaon phases [152, 153] having a value ~ 5 fm [165]. The radius of a critical droplet is to be greater than the correlation length (ξ) for kaons [152, 165]. We perform our calculation with K^- droplets with radii greater than 5 fm. The other important parameter in the prefactor is the surface tension. The surface tension between nuclear and kaon phases was already estimated by Christiansen and collaborators [175] and found to be sensitive to the EOS. We perform this calculation for a set of values of surface tension $\sigma = 15$, 20, 25 and 30 MeV fm^{-2}. The prefactor (Γ_0) is shown as a function of temperature in 7.6. It is shown for a baryon density $n_b = 4.235n_0$ which is just above the critical density $3.9n_0$ for the K^- condensation at zero temperature [159], and surface tension $\sigma = 15$ MeV fm^{-2}. The prefactor was also approximated by T^4 according to the dimensional analysis in many calculations [152, 168]. The upper curve in Fig. 7.6 shows the prefactor of Eq. (7.19) including only the contribution of neutrino shear viscosity whereas the prefactor approximated by T^4 corresponds to the lower curve. It is evident from Fig. 7.6 that the approximated prefactor is very small compared with our result.

Now we discuss the nucleation time of a critical droplet of the K^- condensed phase in neutrino-trapped nuclear matter and the effect of neutrino shear viscosity on it. The thermal nucleation rate of the critical droplet is calculated within a volume with $R_{nuc} =$ 100 meters in the core of a neutron star where the density, pressure and temperature are constant. The thermal nucleation time is plotted with temperature for a baryon density $n_b = 4.235n_0$ in Fig. 7.7. Furthermore, this calculation is done with the kaon correlation length $\xi = 5$ fm and surface tension $\sigma = 15$, 20, 25 and 30 MeV fm^{-2}. The size of the critical droplet increases with increasing surface tension. Radii of the critical droplets are 7.1, 9.4, 11.7 and 14.1 fm corresponding to $\sigma = 15$, 20, 25 and 30 MeV fm^{-2}, respectively, at a baryon density $4.235n_0$. The nucleation time of the critical droplet diminishes as temperature increases for all cases studied here. However, the temperature corresponding to a particular nucleation time for example 10^{-3} s, increases as the surface

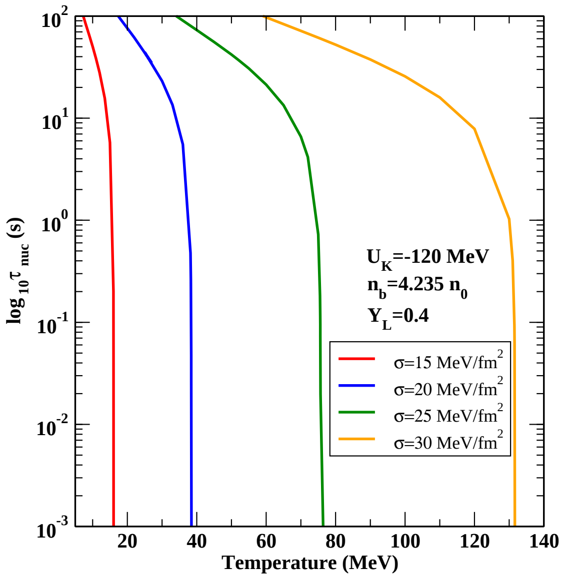

Figure 7.7: Thermal nucleation time is displayed with temperature for different values of surface tension

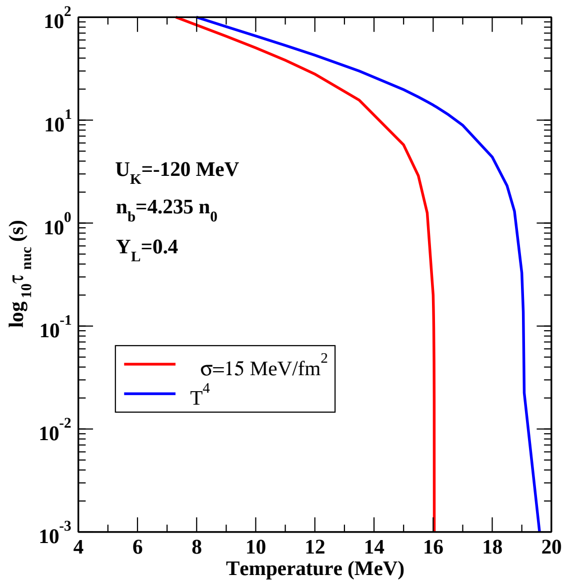

Figure 7.8: Comparison of our results for a fixed surface tension with the calculation of the T^4 approximation.

tension increases. There is a possibility that the condensate might melt down if the temperature is higher than the critical temperature. The critical temperature of the K^- condensation was investigated in neutrino-free matter in Ref. [162] and for neutrino matter in Ref. [176]. We compare thermal nucleation times corresponding to different values of the surface tension with the early post bounce time scale $t_d \sim 100$ ms in the core collapse supernova [154] when the central density might reach the threshold density of the K^- condensation. The time scale t_d is much less than the neutrino diffusion time ~ 1 s as obtained by Ref. [174]. Thermal nucleation of the K^- condensed phase may be possible when the thermal nucleation time is less than t_d. For $\sigma = 15$ MeV fm^{-2}, the thermal nucleation time of 10^{-3} s occurs at a temperature 16 MeV. It is evident from Fig. 7.7 that the thermal nucleation time is strongly dependent on the surface tension. Further thermal nucleation of a K^- droplet is possible so long as the condensate might survive the melt down at high temperatures [162,176]. Our results of thermal nucleation time are compared with the calculation taking into account the prefactor approximated by T^4 in Fig. 7.8 for surface tension $\sigma = 15$ MeV fm^{-2} and at a density $n_b = 4.235 n_0$. The upper curve denotes the calculation with T^4 approximation whereas the lower curve corresponds to the influence of neutrino shear viscosity on the thermal nucleation time. The results of the T^4 approximation overestimate our results hugely. For a nucleation time of 10^{-3} s at a temperature T=16 MeV, the corresponding time in the T^4 approximation is larger by several orders of magnitude.

7.4 Summary and Conclusions

We have studied shear viscosities of different particle species in neutrino-trapped β-equilibrated and charge neutral nuclear matter. We have used equations of state of the nuclear and the K^- condensed phases in the relativistic mean field model for the calculation of shear viscosity. It is noted that neutrons, protons and electrons come into thermal equilibrium in the weak interaction time scale. The shear viscosity due to neutrinos is calculated treating other particles as background and found to dominate the total shear viscosity.

Next we have investigated the first-order phase transition from the neutrino-trapped nuclear matter to the K^- condensed matter through the thermal nucleation of a critical droplet of the K^- condensed matter using the same relativistic EOS as discussed above. Our emphasis in this calculation is the role of the shear viscosity due to neutrinos in the prefactor and its consequences on the thermal nucleation rate. We have observed that the thermal nucleation of a critical K^- droplet might be possible well before the neutrino diffusion takes place. Furthermore, a comparison of our results with that of the calculation of thermal nucleation time in the T^4 approximation shows that the latter overestimates our results of thermal nucleation time computed with the prefactor including the neutrino shear viscosity. Though we have performed this calculation with the K^- optical potential depth of $U_{\bar{K}}(n_0) = -120$ MeV, we expect qualitatively same results for other values of the K^- optical potential depth (see table 5.2).

Bibliography

[1] A Hewish, S J Bell, J D H Pilkington , P F Scott and R A Collins *Nature* **217** 709 (1968). 1

[2] T Gold *Nature* **218** 731 (1968); T Gold *Nature* **221** 25 (1969). 1

[3] D G Ravenhall, C J Pethick and J R Wilson *Phys. Rev. Lett.* **50** 2066 (1983). 5, 30

[4] M Hashimoto, H Seki and M Yamada *Prog. Th. Phys.* **71** 320 (1984). 5, 30

[5] K Oyamatsu *Nucl. Phys. A* **561** 431 (1993). 5, 30

[6] P Demorest, T Pennucci, S M Ransom, M S E Roberts and J W T Hessels *Nature* **467** 1081 (2010). 6, 11, 97

[7] ATNF Pulsar Catalogue (http://www.atnf.csiro.au/research/pulsar/psrcat/); R N Manchester, G B Hobbs, A Teoh and M Hobbs *Astron. J.* **129** 1993 (2005). 6

[8] http://stellarcollapse.org/nsmasses; J M Lattimer *to appear in Annu. Rev. Nucl. Part. Sci.* **62** (2012). 7, 8

[9] J P Clark, S P Goodwin, P A Crowther, L Kaper, M Fairbairn, N Langer and C Brocksopp *Astron. Astrophys.* **392** 909 (2002). 9

[10] I H Stairs *J. Phys. G* **32** S259 (2006). 9

[11] G H Janssen, B W Stappers, M Kramer, D J Nice, A Jessner, I Cognard and M B Purver *Astron. Astrophys.* **490** 753 (2008). 10

[12] S E Thorsett and D Chakrabarty *Astrophys. J.* **512** 288 (1999). 10

[13] I N Reid *Astron. J.* **111** 2000 (1996). 10

[14] S Rappaport, P Podsiadlowski, P C Joss, R DiStefano and Z Han *Mon. Not. R. Astron. Soc.* **273** 731 (1995). 10

[15] P C C Freire, S M Ransom, S Begin, I H Stairs, J W T Hessels, L H Frey and F Camilo *Astrophys. J.* **675** 670 (2008). 11

[16] P A Caraveo, D F Bignami, R Mignani, L G Taff *Astrophys. J. Lett.* **461** L91 (1996). 12, 13

[17] A Golden and A Shearer *Astron. Astrophys.* **342** L5 (1999). 12

[18] P Haensel *Astron. Astrophys.* **380** 186 (2001). 12

[19] K Mori, C J Hailey, F Paerels and S Zane *Adv. Sp. Res.* **33** 503 (2004). 12

[20] W F Brisken, S E Thorsett, A Golden and W M Goss *Astrophys. J.* **593** L89 (2003). 13

[21] N Sartore, A Tiengo, S Mereghetti, A De Luca, R Turolla and F Haberl *Astron. Astrophys* **541** A66 (2012). 13

[22] F M Walter, T Eisenbeiß, J M Lattimer, et al. *Astrophys. J.* **724** 669 (2010). 13

[23] S Bhattacharyya *Adv. Sp. Res.* **45** 949 (2010). 13

[24] F Özel *Nature* **441** 1115 (2006). 13, 14

[25] J Madej, P C Joss and A Rozanska *Astrophys. J.* **602** 904 (2004). 14

[26] F Özel, T Güver and D Psaltis *Astrophys. J.* **693** 1775 (2009). 15

[27] T Güver, F Ožel, A Cabrera-Lavers and P Wroblewski *Astrophys. J.* **712** 964 (2010). 15

[28] T Güver, P Wroblewski, L Camarota and F Ožel *Astrophys. J.* **719** 1807 (2010). 15

[29] A W Steiner, J M Lattimer and E F Brown *Astrophys. J.* **722** 33 (2010). 15

[30] F Özel, G Baym and T Güver *Phys. Rev. D* **82** 101301(R) (2010). 15

[31] N A Webb and D Barret *Astrophys. J.* **671** 727 (2007). 15

[32] S Guillot, R E Rutledge and E F Brown *Astrophys. J.* **732** 88 (2011). 15

[33] C O Heinke, G B Rybicki, R Narayan and J E Grindlay *Astrophys. J.* **644** 1090 (2006). 15

[34] M Bejgar and P Haensel *Astron. Astrophys.* **405** 747 (2003). 16

[35] R A Fesen, J M Shull, and A P Hurford *Astron. J.* **113** 354 (1997). 16

[36] A G Lyne et al. *Scinece* **303** 1153 (2004). 16

[37] J M Lattimer and B F Schutz *Astrophys. J.* **629** 979 (2005). 16

[38] R C Duncan and C Thompson *Astrophys. J.* **392** L9 (1992). 17, 45

[39] C Kouveluotou et al *Nature* **393** 235 (1998); C Kouveluotou et al *Astrophys. J.* **510** L115 (1999). 17, 18

[40] http://www.physics.mcgill.ca/∼pulsar/magnetar/main.html. 17

[41] A L Watts and T E Strohmayer *Astrophys. J.* **637** L117 (2006); T E Strohmayer and A L Watts *Astrophys. J.* **653** 593 (2006). 18

[42] P M Woods and C Thompson *preprint* arXiv:astro-ph/0406133v3. 18

[43] C Thompson and R C Duncan *Mon. Not. R. Astron. Soc.* **275** 255 (1995) ; *Astrophys. J.* **473** 322 (1996). 18

[44] D Lai *Rev. Mod. Phys.* **73** 629 (2001). 20

[45] Thompson C and Duncan R C *Astrophys. J.* **408** 194 (1993); Thompson C and Duncan R C *Astrophys. J.* **473** 322 (1996). 18, 21

[46] D Lai and S L Shapiro *Astrophys. J.* **383** 745 (1991). 21, 22, 23, 27, 28

[47] S Chakraborty, D Bandyopadhyay and S Pal *Phys. Rev. Lett.* **78** 2898 (1997). 21

[48] G Baym, C Pethick and P Sutherland *Astrophys. J.* **170** 299 (1971). 21

[49] A Broderick, M Prakash, and J M Lattimer *Astrophys. J.* **537** 351 (2000). 21, 32

[50] G Audi, A H Wapstra and C Thibault *Nucl. Phys. A* **729** 337 (2003). 24

[51] P Moller, J R Nix, W D Myers and W J Swiatecki *At. Data Nucl. Data Tables* **59** 185 (1995). 24, 28

[52] G Baym , H A Bethe, and C J Pethick *Nucl. Phys.* A **175** 225 (1971). 24, 30, 31

[53] R Nandi and D Bandyopadhyay *J. Phys. Conf. Ser.* **312** 042016 (2011). 25, 40, 44

[54] M Bender et al *Phys. Rev. C* **60** 034304 (1999). 28

[55] S B Rüster, M Hempel and J B Schaffner-Bielich *Phys. Rev. C* **73** 035804 (2006). 28

[56] W D Langer, L C Rosen, J M Cohen and A G W Cameron *Astrophys. Space. Sc.* **5** 529 (1969). 30, 90, 95

[57] H A Bethe, G Bömer and K Sato *Astron. Astrophys.* **7** 270 (1970). 30

[58] J W Negele and D Vautherin *Nucl. Phys. A* **207** 298 (1973). 30, 40

[59] K S Cheng, C C Yao and Z C Dai *Phys. Rev. C* **55** 2092 (1997). 31

[60] D G Yakovlev and A D Kaminker *The Equation of State in Astrophysics* ed. G Chabrier and E Schatzman (Cambridge: Cambridge University) **214** (1994). 31

[61] L Hernquist *Astrophys. J. Suppl. Ser.* **56** 325 (1984). 31

[62] N Nag and S Chakrabarty *Eur. Phys. J. A* **45** 99 (2010). 31

[63] P Bonche, S Levit and D Vautherin *Nucl. Phys. A* **427** 278 (1984) ; P Bonche, S Levit and D Vautherin *Nucl. Phys. A* **436** 265 (1985). 31, 32, 33, 43

[64] E Suraud *Nucl. Phys. A* **462** 109 (1987). 31, 32, 42, 43

[65] J De, X Vinas, S K Patra and M Centelles *Phys. Rev. C* **64** 057306 (2001). 31, 35

[66] T Sil, J N De, S K Samaddar, X Vinas, M Centelles, B K Agrawal and S K Patra Phys. Rev. C **66** 045803 (2002). 31, 35

[67] T J Bürvenich, I N Mishustin and W Greiner *Phys. Rev. C* 76, 034310 (2007). 31

[68] R Nandi, D Bandyopadhyay, I N Mishustin and W Greiner *Astrophys. J.* **736** 156 (2011). 32, 33

[69] H Krivine, J Treiner and 0 Bohigas *Nucl. Phys. A* **336** 115 (1980). 33

[70] J R Stone, J C Miller, R Koncewicz, P D Stevenson and M R Strayer *Phys. Rev. C* **68** 034324 (2003). 33, 58

[71] M Brack, C Guet and H B Hâkansson *Phys. Rep.* **123** 275 (1985). 35

[72] E Chabanat, P Bonche, P Haensel, J Meyer and R Schaeffer *Nucl. Phys. A* **635** 231 (1998). 41

[73] J M Lattimer and D N Schramm *Astrophys. J.* **213** 225 (1977). 43, 44

[74] B S Meyer *Astrophys. J.* **343** 254 (1989). 43

[75] J D Gelfand et al *Astrophys. J.* **634** L89 (2005). 44

[76] M Arnould, S Goriely and K Takahashi *Phys. Rep.* **450** 97 (2007). 44

[77] C Barat et al *Astron. Astrophys.* **126** 400 (2003). 45

[78] G L Israel et al *Astrophys. J.* **628** L53 (2005). 45, 46

[79] A L Watts *preptint* arXiv:astro-ph/1111.0514. 45, 46, 51, 53

[80] A L Watts and T E Strohmayer *Adv. Space Res.* **40** 1446 (2007). 45, 46

[81] R C Duncan *Astrophys. J.* **498** L45 (1998). 45, 46, 47, 53

[82] A L Piro *Astrophys. J.* **634** L153 (2005). 46, 47

[83] L Samuelsson and N Andersson *Mon. Not. Astron. Soc.* **374** 256 (2007). 46

[84] H Sotani, K D Kokkotas and N Stergioulas *Mon. Not. Astron. Soc.* **375** 261 (2007). 46, 47, 48, 49, 50, 51

[85] A W Steiner and A L Watts *Phys. Rev. Lett.* **103** 181101 (2009). 46, 51, 53

[86] H Sotani, K D Kokkotas and N Stergioulas *Mon. Not. Astron. Soc.* **385** L5 (2008). 46, 47

[87] A Colaiuda, H Beyer and K D Kokkotas *Mon. Not. Astron. Soc.* **396** 1441 (2009). 46

[88] P Cerda-Dur*á*n, N Stergioulas and J A Font *Mon. Not. Astron. Soc.* **397** 1607 (2009). 46

[89] Y Levin *Mon. Not. Astron. Soc.* **368** L35 (2006). 46

[90] K Glampedakis and N Andersson *Mon. Not. Astron. Soc.* **371** 1311 (2006). 46

[91] Y Levin *Mon. Not. Astron. Soc.* **377** 159 (2007). 46

[92] U Lee *Mon. Not. Astron. Soc.* **374** 1015 (2007); *ibid* **385** 2069 (2008). 46

[93] H Sotani *Mon. Not. Astron. Soc.* **417** L70 (2011). 46, 47, 51

[94] R Nandi, D Chatterjee and D Bandyopadhyay *preprint* arXiv:astro-ph/1207.3247. 46, 54

[95] B W Carrol et al *Astrophys. J.* **305** 767 (1986). 47

[96] P N McDermott, H M van Horn and C J Hansen *Astrophys. J.* **325** 725 (1988). 47

[97] B L Schumaker and K S Thorne *Mon. Not. R. Astron. Soc.* **203** 457 (1983). 47, 49

[98] N Messios, D B Papadopolous and N Stergioulas *Mon. Not. R. Astron. Soc.* 328 1161 (2001). 47

[99] I Wasserman, S L Shapiro *Astrophys. J.* **265** 1036 (1983). 48

[100] K Konno, T Obata and Y Kojima *Astron. Astrophys.* **352** 211 (1999). 48

[101] S Ogata and S Ichimaru *Phys. Rev. A* **42** 4867 (1990). 51

[102] T Strohmayer, H M van Horn, S Ogata, H Iyetoni and S Ichimaru *Astrophys. J.* 375 679 (1991). 51, 52

[103] P Haensel in *Physics of Neutron Star Interiors* ed. D Blaschke, N K Glendenning and A Sedrakian *Lecture notes in physics* **578** (Springer, Heidelberg) 127 (2001). 52

[104] A Colaiuda and K D Kokkotas *Mon. Not. R. Astron. Soc.* **414** 3014 (2011). 55

[105] A K Glendenning *Compact Stars* (Springer, New York, 1997). 57, 58, 59, 60, 68, 89

[106] M Baldo in *Nuclear Methods and Nuclear Equation of State* ed. M Baldo (Singapore: World Scientific) 1 (1999). 58

[107] M Baldo and F Burgio in *Physics of Neutron Star Interiors*, ed. D Blaschke, N K Glendenning and A Sedrakian *Lecture Notes in Physics* **578** 1 (2001). 58

[108] F Weber *Pulsars as Astrophysical Laboratories for Nuclear and Particle Physics* (Bristol: IOP Publishing 1999). 58

[109] F Weber and M K Weigel *Phys. Rev. C* **32** 2141 (1985). 58

[110] A Akmal, V R Pandharipande and D G Ravenhall *Phys. Rev. C* **58** 1804 (1998). x, 58, 83, 84

[111] J D Walecka *Ann. of Phys.* **83** 491 (1974). 58

[112] B D Serot And J D Walecka in *Advances in Nuclear Physics* ed. J W Negele and E vogt (Plenum Press, New York, 1986). 58

[113] J Boguta and A R Bodmer *Nucl. Phys. A* **292** 413 (1977). 59, 60

[114] J Schaffner and I N Mishustin *Phys. Rev. C* **53** 1416 (1996). 59, 87, 89

[115] D B Kaplan and A E Nelson *Phys. Lett. B* **175** 57 (1986). 64, 65, 89

[116] A Mishra, S Schramm and W Greiner *Phys. Rev. C* **78** 024901 (2008). 65

[117] A Mishra, A Kumar, S Sanyal, V. Dexheimer and S Schramm *Eur. Phys. J. A* **45** 169 (2010). 65

[118] N K Glendenning and J Schaffner-Bielich *Phys. Rev. C* **60** 025803 (1999). 65, 89

[119] N K Glendenning and S A Moszkowski *Phys. Rev. Lett.* **67** 2414 (1991). 69, 80

[120] E Friedman, A Gal and C J Batty *Nucl. Phys. A* **579** 518 (1994). 70

[121] E Friedman, A Gal, J Mareš and A Cieplý *Phys. Rev. C* **60** 024314 (1999). 70

[122] A Ramos and E Oset *Nucl. Phys. A* **671** 481 (2000). 70

[123] J Schaffner-Bielich, V Koch and M Effenberger *Nucl. Phys. A* **669** 153 (2000). 70

[124] Y Akaishi and T Yamazaki *Phys. Rev. C* **65** 044005 (2002). 70

[125] Y Akaishi, A Dote and T. Yamazaki *Phys. Lett. B* **613** 140 (2005). 70

[126] A Ramos, V K Magas, E Oset and H Toki *Nucl. Phys A* **804** 219 (2008). 70

[127] N Andersson and K D Kokkotas *Mon. Not. R. Astron. Soc.* **299** 1059 (1998); *Int. J. Mod. Phys. D* **10** 381 (2001). 71

[128] N Andersson, G L Comer, and K Glampedakis *Nucl. Phys. A* **763** 212 (2005). 71

[129] E Flowers and N Itoh *Astrophys. J.* **206** 218 (1976). 71, 84

[130] E Flowers and N Itoh *Astrophys. J.* **230** 847 (1979). 71, 73, 75, 78, 84, 87

[131] C Cutler and L Lindblom *Astrophys. J.* **314** 234 (1987). x, 71, 83, 84

[132] O Benhar and M Valli *Phys. Rev. Lett.* **99** 232501 (2007). 71

[133] P S Shternin and D G Yakovlev *Phys. Rev. D* **78** 063006 (2008). 71, 72, 73, 74, 76, 77, 78, 79, 82, 83, 87

[134] H A Bethe and G E Brown *Astrophys. J.* **445** L129 (1995). 72

[135] S Pal, D Bandyopadhyay and W. Greiner *Nucl. Phys. A* **674** 553 (2000). 72, 78, 87, 89, 97

[136] S Banik and D Bandyopadhyay *Phys. Rev. C* **64** 055805 (2001). 72, 78, 87

[137] R Nandi, S Banik and D Bandyopadhyay *Phys. Rev. D* **80** 123015 (2009). 72, 75, 79

[138] G Rupak and T Schäfer *Phys. Rev. A* **76** 053607 (2007). 74

[139] J M Ziman *Electrons and Phonons* (Oxford University Press, 1960). 74

[140] P S Shternin and D G Yakovlev *Phys. Rev. D* **75** 103004 (2007). 76, 77, 78, 84, 85

[141] H Heiselberg and C J Pethick *Phys. Rev. D* **48** 2916 (1993). 76, 77

[142] D A Baiko, P Haensel and D G Yakovlev *Astron. Astrophys.* **374** 151 (2001). 78, 79, 82

[143] G Q Li and R Machleidt *Phys. Rev. C* **48** 1702 (1993); *Phys. Rev. C* **49** 566 (1994). 79, 82

[144] S Pal, C M Ko, Z Lin and B Zhang *Phys. Rev. C* **62** 061903(R) (2000). 81

[145] H Heiselberg and M Hjorth-Jensen *Astrophys. J. Lett.* **525** L45 (1999). 84

[146] M Nayyar and B J Owen *Phys. Rev. D* **73** 084001 (2006). 86

[147] D Chatterjee and D Bandyopadhyay *Phys. Rev. D* **74** 023003 (2006); *ibid* **75** 123006 (2007); *Astrophys. J.* **680** 686 (2008); *J. Phys. G* **35** 104078 (2008). 86

[148] P J Ellis, R Knorren and M Prakash *Phys. Lett. B* **349** 11 (1995). 87, 89

[149] R Knorren, M Prakash and P J Ellis *Phys. Rev. C* **52** 3470 (1995). 87, 89

[150] M G Alford, K Rajagopal, S Reddy and F Wilczek *Phys. Rev. D* **64** 074017 (2001). 87

[151] N K Glendenning *Phys. Rev. D* **46** 1274 (1992). 88, 89

[152] L P Csernai and J I Kapusta *Phys. Rev. D* **46** 1379 (1992). 88, 90, 96, 101

[153] I Bombaci, D Logoteta, P K Panda, C Providencia and I Vidana *Phys. Lett. B* **680** 448 (2009). 88, 90, 101

[154] I Sagert et al *Phys. Rev. Lett.* **102** 081101 (2009). 89, 102

[155] G E Brown, K Kubodera, M Rho and V Thorsson *Phys. Lett. B* **291** 355 (1992). 89

[156] V Thorsson, M Prakash, and J M Lattimer *Nucl. Phys. A* **572** 693 (1994). 89

[157] C H Lee, G E Brown, D P Min and M Rho *Nucl. Phys. A* **585** 401 (1995). 89

[158] M Prakash, I Bombaci, M Prakash, P J Ellis, J M Lattimer and R Knorren *Phys. Rep.* 280 1 (1997). 89

[159] S Banik and D Bandyopadhyay *Phys. Rev. C* **63** 035802 (2001). 89, 101

[160] S Banik and D Bandyopadhyay *Phys. Rev. C* **66** 065801 (2002); *Phys. Rev. D* **67** 123003 (2003). 89

[161] J A Pons, S Reddy, P J Ellis, M Prakash and J M Lattimer *Phys. Rev. C* **62** 035803 (2000). 89

[162] S Banik, W Greiner and D Bandyopadhyay *Phys. Rev. C* **78** 065804 (2008). 89, 102

[163] T Norsen *Phys. Rev. C* **65** 045805 (2002). 89, 90

[164] S Banik and D Bandyopadhyay *Phys. Rev. D* **82** 123010 (2010). 89, 90, 95, 96, 98

[165] T Norsen and S Reddy *Phys. Rev. C* **63** 065804 (2001). 90, 94, 101

[166] K Iida and K Sato, *Phys. Rev. C* **58** 2538 (1998). 90

[167] H Heiselberg in *International Symposium on Strangeness and Quark Matter* ed. G Vassiliadis, A D Panagiotou, S Kumar and J Madsen (World Scientific, Singapore) 338 (1999). 90, 95

[168] B W Mintz, E S Fraga, G Pagliara and J Schaffner-Bielich *Phys. Rev. D* **81** 123012 (2010). 90, 95, 98, 101

[169] I Bombaci, D Logoteta, P K Panda, C Providencia and I Vidana *Astron. Astrophys.* **528** A71 (2011). 90

[170] L A Turski and J S Langer *Phys. Rev. A* **22** 2189 (1980). 90, 95, 96

[171] S Banik and Rana Nandi *AIP Conf. Proc.* **1441** 396 (2011). 90

[172] S Banik, R Nandi and D Bandyopadhyay *Phys. Rev. C* **84** 065804 (2011). 90

[173] R Venugopalan and A P Vischer *Phys. Rev. E* **49** 5849 (1994). 90, 96

[174] B T Goodwin and C J Pethick *Astrophys. J.* **253** 816 (1982). 91, 93, 100, 102

[175] M B Christiansen, N K Glendenning and J Schaffner-Bielich *Phys. Rev. C* **62** 025804 (2000). 101

[176] S Banik, R Nandi and D Bandyopadhyay *preprint* arXiv:astro-ph/1206.1701. 102

List of publications

1. **Neutron Star Crust in Strong Magnetic Fields**

   R Nandi and D Bandyopadhyay *J. Phys. Conf. Ser.* **312** 042016 (2011).

2. **Inner crust of neutron stars in strongly quantizing magnetic fields**

   R Nandi, D Bandyopadhyay, I N Mishustin and W Greiner *Astrophys. J.* **736** 156 (2011).

3. **Shear viscosity in antikaon condensed matter**

   R Nandi, S Banik and D Bandyopadhyay *Phys. Rev. D* **80** 123015 (2009).

4. **Nucleation of antikaon condensed matter in protoneutron stars**

   S Banik and R Nandi *AIP Conf. Proc.* **1441** 396 (2011).

5. **Shear viscosity and the nucleation of antikaon condensed matter in protoneutron stars**

   S Banik, R Nandi and D Bandyopadhyay *Phys. Rev. C* **84** 065804 (2011).

6. **Melting of antikaon condensate in protoneutron stars**

   S Banik, R Nandi and D Bandyopadhyay, arXiv:astro-ph/1206.1701.

7. **Role of strongly magnetized crusts in torsional shear modes of magnetars**

   R Nandi, D Chatterjee and D Bandyopadhyay, arXiv:astro-ph/1207.3247.